



Agenzia nazionale per le nuove tecnologie, l'energia  
e lo sviluppo economico sostenibile



*Ministero dello Sviluppo Economico*

RICERCA DI SISTEMA ELETTRICO

# Reinterpretation of the late SCK-CEN/ENEA Experimental Neutronic Campaign on TAPIRO Fast Reactor with MCNPX Monte Carlo Transport Code

*N. Burgio, A. Santagata, M. Frullini, F. La Stella, F. Garofalo, C. Rusconi*



Report RdS/2012/042

REINTERPRETATION OF THE LATE SCK-CEN/ENEA EXPERIMENTAL NEUTRONIC CAMPAIGN ON TAPIRO FAST REACTOR WITH MCNPX MONTE CARLO TRANSPORT CODE

N. Burgio, A. Santagata – ENEA, M. Frullini, F. La Stella, F. Garofalo, C. Rusconi – CIRTEN Uniroma1

Settembre 2012

Report Ricerca di Sistema Elettrico

Accordo di Programma Ministero dello Sviluppo Economico - ENEA

Area: Governo, gestione e sviluppo del sistema elettrico nazionale

Progetto: Nuovo nucleare da fissione: collaborazioni internazionali e sviluppo competenze in materia nucleare

Responsabile del Progetto: Mariano Tarantino, ENEA

**Titolo**

## Reinterpretation of the Late SCK-CEN/ENEA Experimental Neutronic Campaign on TAPIRO Fast Reactor with MCNPX Monte Carlo Transport Code.

**Descrittori**

**Tipologia del documento:** Rapporto Tecnico  
**Collocazione contrattuale:** Accordo di programma ENEA-MSE: tema di ricerca "Nuovo nucleare da fissione"  
**Argomenti trattati:** Neutronica  
 Reattori Nucleari Veloci  
 Reattori sottocritici/ADS  
 Metodi Montecarlo

**Sommario**

Le attività di Ricerca e Sviluppo richiedono una verifica di scopo delle misure e degli esperimenti proposti affinché le attività siano rappresentative dei requisiti tecnologici, politici ed economici richiesti. Nell'ambito delle presenti attività relative al "Nuovo Nucleare da fissione" all'asse di Ricerca e Sviluppo si è spostato, anche ad opera dei recenti eventi di Fukushima, sul potenziamento degli studi relativi ai sistemi innovativi che sono stati definiti in Generation IV e nei successivi documenti comunitari. Una grossa porzione delle attività ENEA e CIRTEV sono indirizzate nel campo della definizione di modelli di Reattori Veloci al Piombo (LFR). Scopo di questo rapporto è fornire una reinterpretazione della campagna sperimentale effettuata negli anni '80 sul reattore veloce TAPIRO da ENEA e SK-CEN. A tal fine è stato costruito un modello di simulazione Monte Carlo (MCNPX) del reattore TAPIRO su cui sono state riprodotte una serie di misure (traverse di fissione e di reazioni di cattura) nei canali sperimentali Diametricale, Radiale 1 e Tangenziale. Sono stati sottoposti a confronto anche i dati di reattività delle barre di controllo e la riserva di reattività del sistema. L'accordo delle stime Monte Carlo con le misure sperimentali è generalmente buono e permette di considerare il modello di calcolo neutronico di TAPIRO come validato. Questo permetterà di progettare esperienze di supporto allo sviluppo di LFR, da tenere in TAPIRO, che siano rappresentative del sistema sotto studio, tagliando costi di progettazione e realizzazione.

**Note**
**Autori**

N. Burgio, A. Santagata (ENEA)

M. Frullini, F. La Stella, F. Garofalo, C. Rusconi (UNIRoma 1)



Copia n.

In carico a:

2			NOME			
			FIRMA			
1			NOME			
			FIRMA			
0	EMISSIONE	18/09/2012	NOME	N. Burgio	M. Tarantino	M. Tarantino
			FIRMA	<i>N. Burgio</i>	<i>M. Tarantino</i>	<i>M. Tarantino</i>
REV.	DESCRIZIONE	DATA		REDAZIONE	CONVALIDA	APPROVAZIONE

## Summary

Reinterpretation of the Late SCK-CEN/ENEA Experimental Neutronic Campaign on TAPIRO Fast Reactor with MCNPX Monte Carlo Transport Code.....	1
Introduction .....	4
Brief description of the MCNPX model of TAPIRO .....	5
Geometry overview .....	5
Control rods scheme and its implementation in the model .....	9
Materials Composition .....	10
Description of the estimators used in the simulations (Tallies) .....	12
Criticality Analysis of the Model .....	17
Clean and Cold Total reactivity.....	17
Shim rods insertion by step.....	19
Test of the worth equivalence of control rods.....	22
Comparison of criticality data of the late experimental campaign with the TAPIRO model outcomes	23
Estimation of the neutron flux spectrum in various position of the radial, tangential and diametrical channel by using F5 detectors tallies .....	25
Comparison of the neutron fluxes with experimental findings of late experimental campaign .....	31
Fission rate Traverses .....	33
MESH Tally fission traverses.....	35
<i>Diametrical channel</i> .....	37
<i>Radial channel</i> .....	39
<i>Tangential Channel</i> .....	41
The detector tally (F5) fission rate responses .....	44
<i>Diametrical channel</i> .....	45
<i>Radial channel</i> .....	50
<i>Tangential Channel</i> .....	55
Reaction Rate Traverses .....	60
MESH Tally reaction rate traverses .....	62
<i>Diametrical channel</i> .....	62
<i>Tangential Channel</i> .....	65
<i>Radial channel</i> .....	68
The detector tally (F5) reaction rate responses .....	71



<i>Diametrical channel</i> .....	71
<i>Tangential channel</i> .....	74
<i>Radial channel</i> .....	76
Comparison of the simulation outcomes with experimental results.....	78
Fission rates of <sup>235</sup> U, <sup>238</sup> U, <sup>237</sup> Np and <sup>239</sup> Pu fission chambers.....	79
<i>Radial Channel 1</i> .....	79
<i>Tangential Channel (B)</i> .....	87
<i>Diametrical Channel</i> .....	91
Activation rates for Au, Ni, Co and Sc activation foils. ....	92
<i>Diametrical channel (B)</i> .....	92
<i>Tangential Channel (B)</i> .....	96
<i>Radial 1 channel</i> .....	99
Conclusions.....	100
Reference .....	101

## Introduction

In the current Research and Development activities the needs of scoping studies where conceptual and experimental designs are tested to be representative of technological, political and economic project requirements, become stringent. After Fukushima accident, the government initiative for the exploitation of the Italian Nuclear industry ( 2<sup>nd</sup> and 3<sup>rd</sup> generation) have been drastically reduced in favor of the validation activities of the totally innovative Generation 4 nuclear systems. The new situation furnishes a motivation to focus all the ENEA and CIRTEN past activities on Lead Fast Reactor (LFR) and Accelerator Driven System (ADS) in a more harmonized design frame where the control of the main design and scope requirements allows the cutting of costs, the increase of safety and the preservation of experiments representativity [1]. Aim of this report is the reinterpretation of the late experimental campaign of 1980-1986 on TAPIRO reactor held by ENEA and SK-CEN [2] by using a new Monte Carlo model of the reactor. The authors are conscious that this argument is “one-step” back respect to the frame presented in the above statement. In our opinion, the adjustment of neutronic models of relatively simple experimental systems, such as TAPIRO [3], constitutes the basis to develop well-designed experience and calibration methodology in support of LFR and ADS activities. To fulfill this scope, a very detailed TAPIRO model has been implemented as MCNPX [4] input deck to reproduce the late experimental configurations on which the measurements have been performed. The model outcomes in terms of criticality analysis ( $K_{eff}$ , control rods worth), neutron flux intensity, neutron spectra, and reaction rates in the irradiation channels have been compared with the late measurements finding an overall good agreement. As conclusion, the model set-up appear to be sufficiently accurate to allow the detailed design of experiences in the irradiation facility of the TAPIRO reactor.

## Brief description of the MCNPX model of TAPIRO

### Geometry overview

MCNPX capability to describe the geometry features of complex system is fully used in the TAPIRO input deck. Practically the description of the model geometry allows a very detailed knowledge of the real system. As reported in Figure 1 and Figure 2 the reactor is constituted by an He cooled cylindrical core of high enriched ( $^{235}\text{U}$  95%) Uranium Molybdenum alloy.

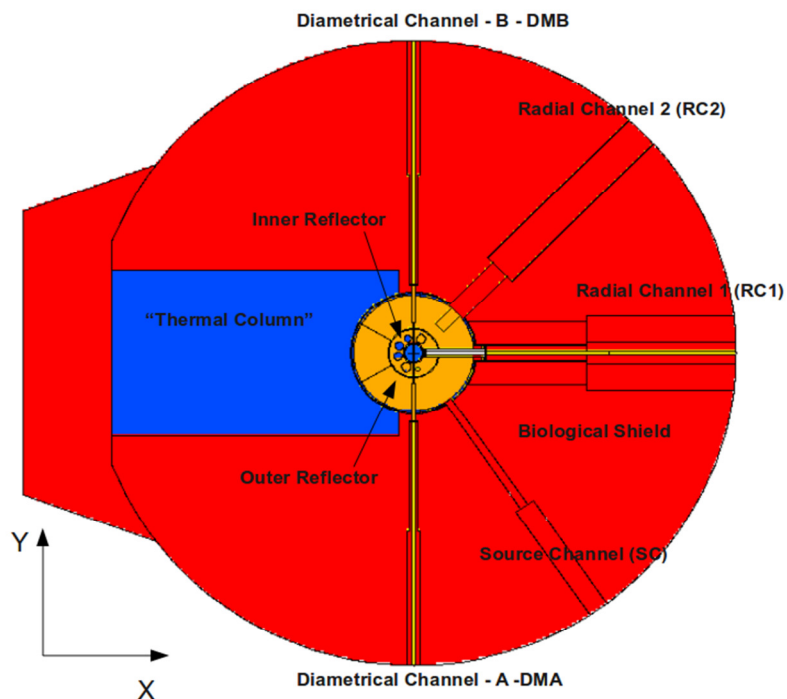


Figure 1 Cross section from MCNPX geometry plotter on YX plane of MCNPX reference system (Plant view).

Two cylindrical shells of copper reflector (inner and outer reflectors) surround the core. The control rod system, housed in the inner reflector, is constituted by five movable cylindrical sectors. It regulates the reactor power by increasing or reducing the neutron escape from the core (see Figure 2).

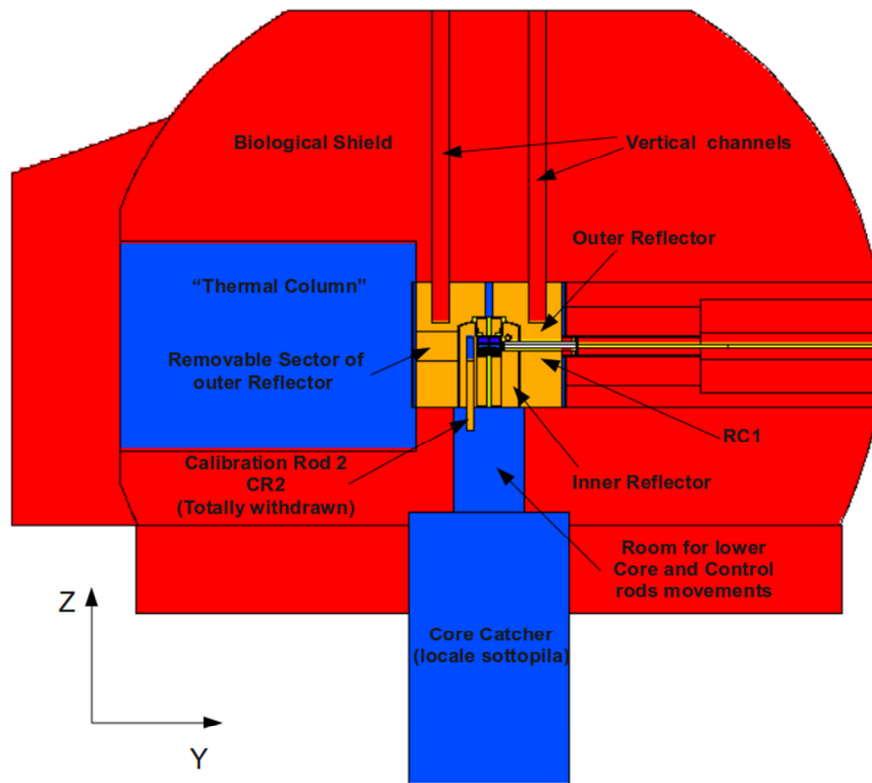


Figure 2 Section from the MCNPX plotter along the YZ plane of MCNPX reference system (side view).

In the outer reflector a removable copper sector (see Figure 2) allows the realization of irradiation experiments for relatively large size samples in a nearly fission neutron spectrum. A heavy concrete biological shield constitutes the last shell around the system. In Figure 2 is also reported the “Thermal Column” room that may host nuclear grade graphite block for irradiation experiments in thermal neutron spectrum. Several irradiation channels pass through the reflector and the core (see Figure 1 and Figure 3b). The diametrical channel (DM) passes through the entire core diameter, at mid-plane height, allowing samples irradiation in almost pure fission spectrum. There are also two radial channels, RC1 and RC2. Symmetrical to RC2 there is the source channel (Figure 1 and Figure 3a) that hosts the reactor start up neutron source. Two vertical channels (Figure 2 and Figure 3b) penetrate from the top of reactor down to the outer surface of the copper reflector.

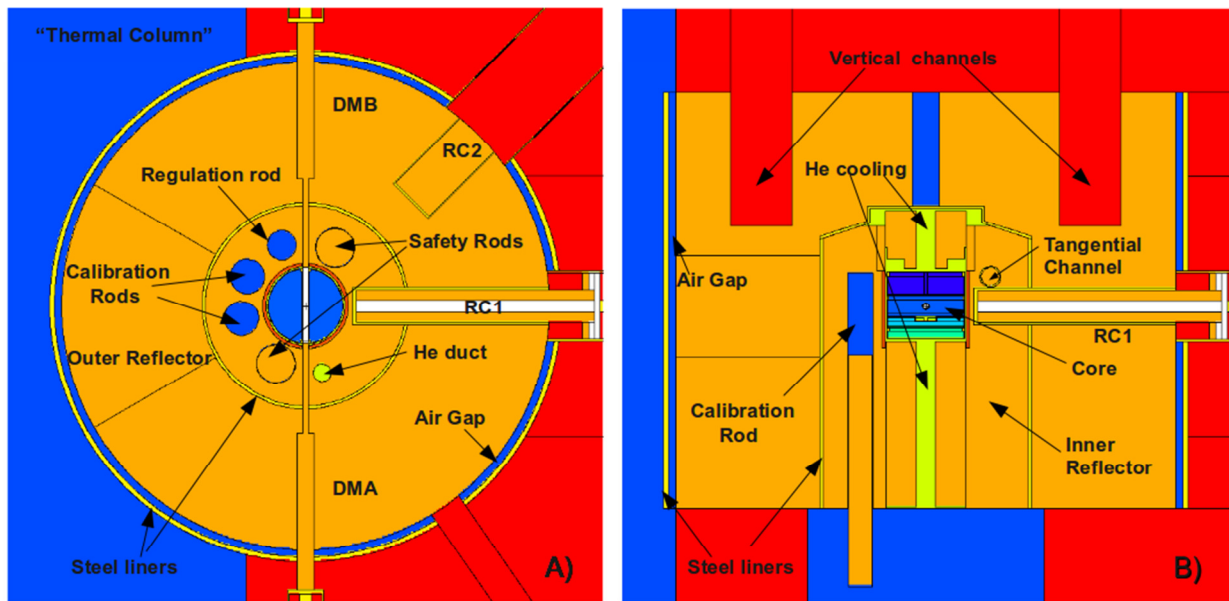


Figure 3

a) Magnification of the “in core” penetration of the diametrical irradiation channel and the final position of the Radial channel 1 and 2.

b) Magnification of the cross section plotting of Figure 2: He cooling system, tangential channel, the axial position of a shim rod, liner and reflector air gaps .

Figure 3a shows the details of the penetration of DM, RC1 and RC2 into the reflector. RC1 has a deeper penetration toward the core than RC2.). Figure 3b shows a side view of the reactor. All the symmetry breaks and heterogeneities, such as helium cooling system, core and inner reflector steel liners, outer reflector air gap, have been represented, at the best of our knowledge, in the MCNPX model.

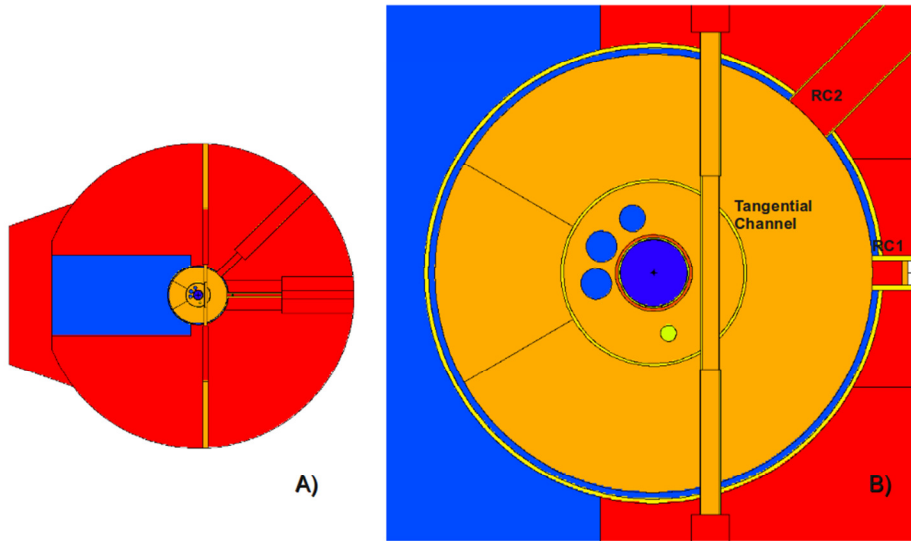


Figure 4 A) Cross section at the Tangential channel height, B) Magnification of the reflector and core cross section at the same height.

Figure 4b shows the tangential channel that lies above the plane of the other channels.

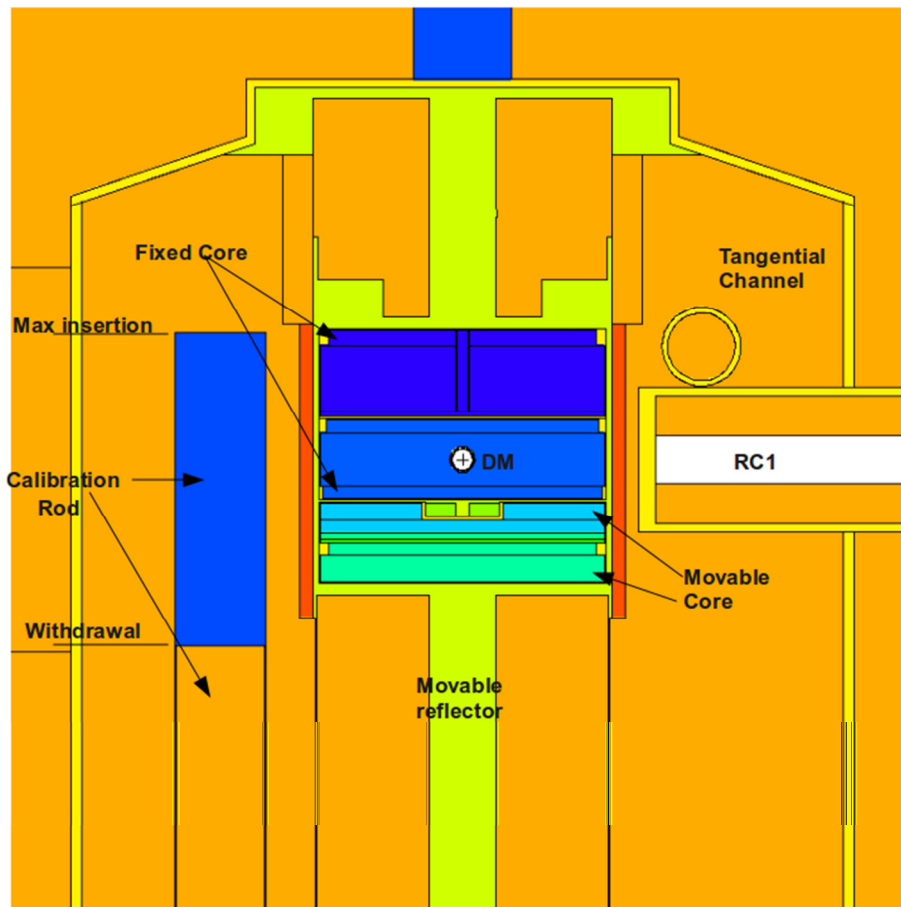


Figure 5 Magnification of the plotter cross section reported in Figure 3B


 <b>Ricerca Sistema Elettrico</b>	<b>Sigla di identificazione</b>	<b>Rev.</b>	<b>Distrib.</b>	<b>Pag.</b>	<b>di</b>
	NNFISS – LP3 - 047	0	L	9	101

Figure 5 reports a more close view of the core with the He cooling system and the inner reflector. The cylindrical core is assembled in several U-Mo alloy disks. Each disk is characterized by a slightly different  $^{235}\text{U}$  enrichment and density. Disk MA1 and MA2 constitute the upper core block and it is called *fixed core*. Disk MA2 has a passing hole that is connected with the diametrical channel and Disk MA1 has a central section that could host some instrumentation (such as thermocouples). Disks MB1, M2, M3, M4, and MB2, form the lower part of the core and it is known as the *movable core*. Disk1 MB1 has a central cavity where some pellets could be housed. The movable core and the lower part of inner reflector, due to a fast mechanic device, could be separated from the fixed core allowing a further reserve of negative reactivity for emergency shutdown (SCRAM) or for special reactor physics measurements.

### Control rods scheme and its implementation in the model

The TAPIRO control system is based on the regulation of the neutron escape from core. For this purpose, five copper cylindrical rods have been located in the inner reflector. Each of the rods can be withdrawn for a total axial length of 15 cm creating a void region of the same length in the reflector. In their withdrawal, the rods go down into apposite cavities in the lower part of the inner reflector (see Figure 3b). Two control rods of 7.5 cm of diameter are used as safety rods (SR1 and SR2) since they realize the greater negative reactivity insertion of the rods set. Safety rods are maintained completely inserted during normal operation and used for normal shutdown or for SCRAM. Two shim rods of 5.7 cm of diameter ensure the reactor rise to power (S1 and S2). The fine adjustment of the criticality is obtained by the regulation rods (RR - 4.8 cm of diameter).



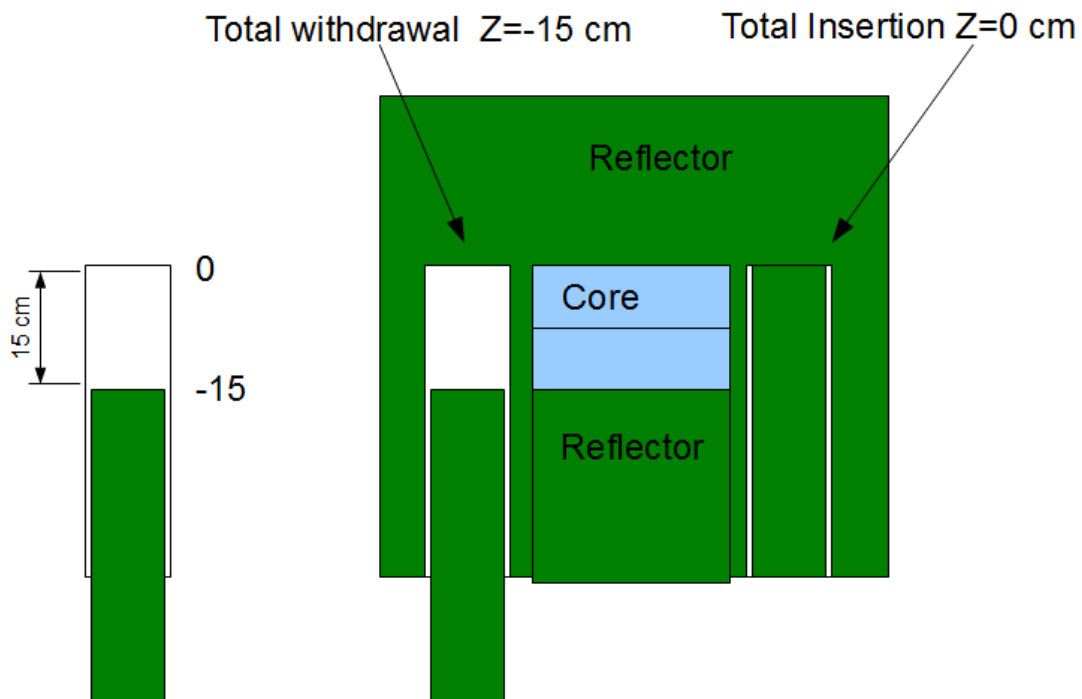


Figure 6. Schematic view of control rods movement systems.

The implementation of the rods movement in the MCNPX model of TAPIRO has been obtained describing each rod as a cylindrical cell (see Figure 6). A suitable MCNPX geometry transformation (see TRANS card in reference [4]) is then applied to the control rod cell. Setting  $Z=0$  means that the control rods remains totally inserted in the inner reflector whereas  $Z=-15$  cm correspond to the total withdrawn of the rod.

## Materials Composition

The materials compositions used in the TAPIRO model, except the fuel composition (see [5] for detailed description), have been reported in Table 1 and Table 2. Compositions, according to MCNPX input modality, are in atom fraction or in weight fraction (negative numbers).

Table 1 Material of neutronic interest

Material id	Nuclide	Composition Atom%	Material description
M1	<sup>4</sup> He	0.999999	Helium for core cooling density 1.0102E-03 g/cm <sup>3</sup>
	<sup>3</sup> He	1.37E-06	
M3	<sup>63</sup> Cu	0.692	COPPER for neutron reflector density 8.942 g/cm <sup>3</sup> .
	<sup>65</sup> Cu	0.308	


Table 2 Structural Materials

Material id	Nuclide	Composition Atom%	Material description
M2	Natural C	1.39E-03	AISI 316L composition from: ‘Coeur de TAPIRO-Protocoles de controle’ report 21.04.1969, pag. 12 (wt%: C 0.03, Mn 1.58, Si 0.55, Ni 12.32, Cr 16.15, Mo 2.01, Fe 67.36).  Material for cladding and lining density 7.9 g/cm <sup>3</sup> .
	<sup>28</sup> Si	1.00E-02	
	<sup>29</sup> Si	5.10E-04	
	<sup>30</sup> Si	3.36E-04	
	<sup>55</sup> Mn	1.60E-02	
	<sup>92</sup> Mo	1.73E-03	
	<sup>94</sup> Mo	1.08E-03	
	<sup>95</sup> Mo	1.85E-03	
	<sup>96</sup> Mo	1.94E-03	
	<sup>97</sup> Mo	1.11E-03	
	<sup>98</sup> Mo	2.81E-03	
	<sup>100</sup> Mo	1.12E-03	
	<sup>50</sup> Cr	7.51E-03	
	<sup>52</sup> Cr	1.45E-01	
	<sup>53</sup> Cr	1.64E-02	
	<sup>54</sup> Cr	4.08E-03	
	<sup>58</sup> Ni	7.97E-02	
	<sup>60</sup> Ni	3.05E-02	
	<sup>61</sup> Ni	1.32E-03	
	<sup>62</sup> Ni	4.19E-03	
<sup>64</sup> Ni	1.06E-03		
<sup>54</sup> Fe	3.89E-02		
<sup>56</sup> Fe	6.16E-01		
<sup>57</sup> Fe	1.44E-02		
<sup>58</sup> Fe	1.95E-03		
Material id	Nuclide	Composition Atom%	Material description
M5	<sup>1</sup> H	1.99E-01	HEAVY BORATED CONCRETE per schermo biologico (a base di cemento pozzolanico) (density 2.8 g/cc)
	<sup>10</sup> B	4.94E-03	
	<sup>11</sup> B	2.00E-02	
	<sup>16</sup> O	5.46E-01	
	<sup>24</sup> Mg	5.01E-03	
	<sup>25</sup> Mg	6.34E-04	
	<sup>26</sup> Mg	6.98E-04	
	<sup>27</sup> Al	1.20E-02	
	<sup>28</sup> Si	7.40E-03	
	<sup>29</sup> Si	3.76E-04	
	<sup>30</sup> Si	2.48E-04	
	<sup>40</sup> Ca	1.41E-02	
	<sup>42</sup> Ca	9.39E-05	
	<sup>43</sup> Ca	1.96E-05	
	<sup>44</sup> Ca	3.03E-04	
	<sup>46</sup> Ca	5.80E-07	
	<sup>48</sup> Ca	2.71E-05	
<sup>54</sup> Fe	3.49E-04		
<sup>56</sup> Fe	5.53E-03		

	<sup>57</sup> Fe	1.30E-04	
	<sup>58</sup> Fe	1.75E-05	
	<sup>138</sup> Ba	7.67E-02	
	<sup>32</sup> S	8.27E-02	
	<sup>23</sup> Na	1.21E-02	
	<sup>39</sup> K	1.12E-02	
	<sup>40</sup> K	1.40E-06	
	<sup>41</sup> K	8.05E-04	
Material id	Nuclide	Composition Atom%	Material description
M4	<sup>24</sup> Mg	7.43E-04	INCONEL density 8.42 g/cm <sup>3</sup> , DM channel adapter for core pass trough.
	<sup>25</sup> Mg	9.41E-05	
	<sup>26</sup> Mg	1.04E-04	
	55Mn	3.64E-03	
	<sup>28</sup> Si	3.75E-03	
	<sup>29</sup> Si	1.91E-04	
	<sup>30</sup> Si	1.26E-04	
	<sup>50</sup> Cr	7.41E-03	
	<sup>52</sup> Cr	1.43E-01	
	<sup>53</sup> Cr	1.62E-02	
	<sup>54</sup> Cr	4.02E-03	
	<sup>58</sup> Ni	5.05E-01	
	<sup>60</sup> Ni	1.93E-01	
	<sup>61</sup> Ni	8.36E-03	
	<sup>62</sup> Ni	2.66E-02	
	<sup>64</sup> Ni	6.73E-03	
	<sup>54</sup> Fe	4.69E-03	
<sup>56</sup> Fe	7.43E-02		
<sup>57</sup> Fe	1.74E-03		
<sup>58</sup> Fe	2.35E-04		

## Description of the estimators used in the simulations (Tallies)

It is important to underline that Monte Carlo results represent an average of the contributions from many events sampled during the simulation; therefore, a relevant parameter is the statistical error associated with the results. There is an important difference between precision and accuracy of a Monte Carlo calculation. **Precision** is the uncertainty of the estimated averages caused by the statistical fluctuations of the physical quantities sampled by the Monte Carlo process. Important portions of the physical phase space might not be sampled because of sampling cut-offs in time or energy, inappropriate use of variance reduction techniques, or an insufficient sampling of important low-probability events. **Accuracy** (systematic error) is a measure of how close is the calculated value to the true physical quantity being estimated. Error or estimations uncertainty associated to the results of Monte Carlo calculations refer only to the precision of the result and not to the accuracy. It is quite possible to calculate a highly precise result that is far from the physical truth because the

 <b>ENEA Ricerca Sistema Elettrico</b>	<b>Sigla di identificazione</b>	<b>Rev.</b>	<b>Distrib.</b>	<b>Pag.</b>	<b>di</b>
	NNFISS – LP3 - 047	0	L	13	101

phenomenon has not been modeled appropriately. Consequently, it is important to briefly describe the MCNPX estimator's mechanisms to better discuss their reliability during the comparison with homologous experimental measurements.

MCNPX has several types of estimator also called "tallies":

1) Current tally (F1 type)

It counts the number of particles that crosses a user-defined surface. Operatively, it counts the scalar product of the particle trajectory with the oriented surface normal times the particles statistical weight. Since surface of infinite area could be defined by the user, MCNPX tries to calculate the active surface of the tally (i.e. the part of surface defined in active cell volume of the simulations). If it fails a user-supplied surface, value must be furnished.

2) Track length Tally (F4)

It counts the density of the particles track length in one of the volume cells defined in the simulation. Numerically it sums the particles weight  $W_t$  times its track length  $T_l$  in the cell and divides the result by the cell volume  $V$ .

$$F4 = \sum_i W_t \frac{T_l}{V}$$

Again, MCNPX tries to calculate the cell volume. If it does not succeed in the volume calculation (asymmetric cell) then a user-supplied volume must be defined.

3) Detector tally (F5)

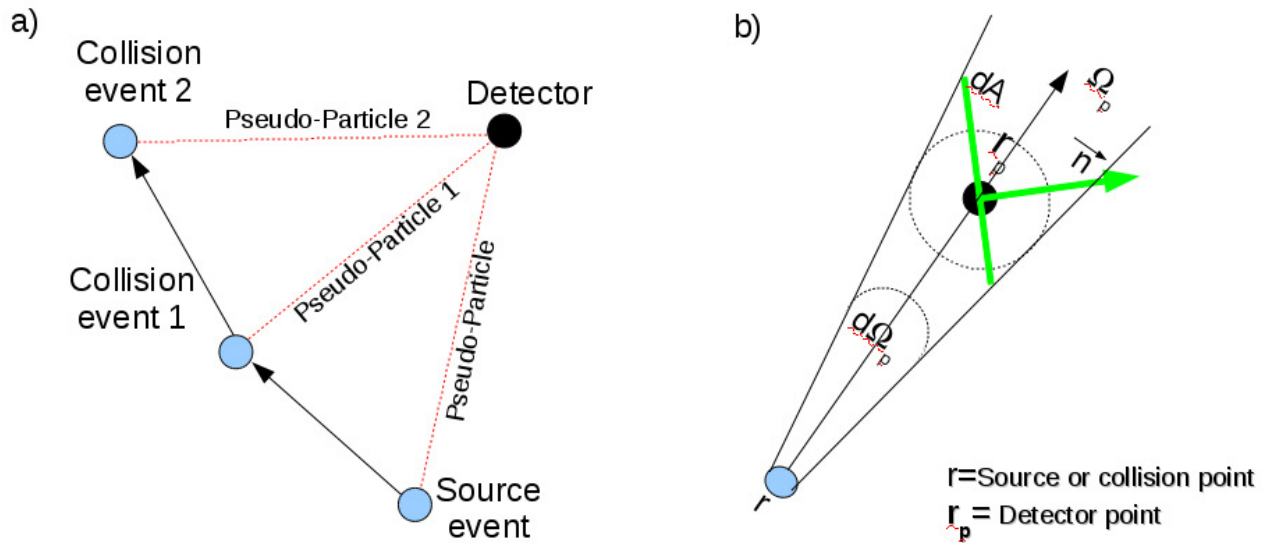


Figure 7 Description of the F5 (point detector) flux estimator of MCNPX

A point detector is a deterministic estimate of the neutron flux from an event points to the estimation point. Contributions to the point detector takes their origin from source and collision events (see Figure 7a). As reported in Figure 7b, the point detector is likely a sphere whose radius tends to zero.  $\Omega_p$  is the direction to the center of the detector sphere  $r_p$  from the event point  $r$ . Let  $d\Omega_p$  be the solid angle subtended by the sphere from  $r$ , and  $dA$  is an area defined as intersection between the cone and a plane passing to the detector point. To contribute to the flux tally a particle must scatter toward A into the solid angle  $d\Omega_p$ , the probability of this event is

$$p(\Omega_p)d\Omega_p$$

Additionally, the particle must have a free-flight (i.e. no collision) for the distance  $R=|r_p - r|$  along the direction  $\Omega_p$  to the sphere. The probability is

$$e^{-\int_0^R -\Sigma_t(s)ds}$$

Where  $\Sigma_t$  is the macroscopic cross section at distance  $s$  from the event point.

The probability of occurrence of both events is

$$p(\Omega_p)d\Omega_p e^{-\int_0^R -\Sigma_t(s)ds}$$

Thus (see MCNP manual for details) the score of the F5 detector tally is

$$F5 = w \frac{p(\mu)}{2\pi R^2} e^{-\int_0^R -\Sigma_t(s)ds}$$

The  $1/2\pi R^2$  term accounts for solid angles effects and  $p(\mu)$  accounts for the probability of scattering toward the detector instead of the direction selected in the random walk. Each contribution to the detector can be considered as the transport of a pseudo-particle to the detector. For contribution by events very close to the detector the  $R^2$  terms causes a singularity. To encompass this problem a spherical region of radius  $R_0$  is used to average the flux response in its volume.

#### 4) Mesh tally

Finally, it is useful to evaluate flux and reaction rates on a geometrical user defined mesh superimposed to the problem geometry. The MESH tally can define meshes in Cartesian, Cylindrical and spherical coordinates. The meshes can be rotated and translated by using transformation cards. This method is particularly interesting to define reaction rate traverses along preferential direction in the problem geometry.

The user can subdivide each of those tallies in several energy intervals to obtain a histogram representation of the response. It should be noted that in general the bins covers different energy intervals and consequently, a correct interpretation of the particles spectral features must be performed accordingly.

A MC code is able to estimates a reaction rate by using the following general relation:

$$S = C \int \Phi(E)R(E)dE$$

where  $C$  is a constant,  $\Phi$  is the neutron fluence (in  $n/cm^2/source\ particle$ ) normally estimated by an F4 tally and  $R(E)$  is a response function (the response function is often a microscopic cross section). An appropriate choice of the response function and of the constant  $C$  allows the estimation of any kind of reaction rate for which a collection of cross section has been compiled. For example, if  $C$  is expressed in  $atom/barn/cm$ , the calculated quantity  $S$  becomes the total number of formed atoms per unit volume per source particle ( $atom/cm^3/s.p.$ ). When  $S$  is estimated in a time independent simulation (e.g. a stationary condition where the decay rate of the formed nuclide is equal to its rate of formation), the quantity is numerically equal to the saturation yield per unit volume.



## Criticality Analysis of the Model

In the criticality analysis, the TAPIRO model has been tested in terms of internal coherence and the control rods worth have been compared with the experimental values reported in Table 3.

Table 3 Experimental data on control rods worth available from TAPIRO nuclear tests report [6]

Control rod	Worth (\$)	*Worth (PCM)
<b>Regulation rod</b>	0.4945	326
<b>Shim rods bunch</b>	1.5	990
<b>Shim rod 1</b>	0.7	462

\*Converted using a value of the delayed neutron fraction  $\beta_{\text{eff}} = 660$  PCM

## Clean and Cold Total reactivity

A first preliminary set of runs has been executed to estimate the  $K_{\text{eff}}$  values with the control rods in extreme positions (completely extracted or completely inserted) with the TAPIRO core maintained at room temperature and assuming the absence of fission products (clean and cold conditions). Table 4 and Table 5 report the  $K_{\text{eff}}$  results for different position of the TAPIRO rods when ENDF-BVII and JEFF3.1 cross sections are used.

Table 4 reactivity estimation worth of the control rods of TAPIRO (ENDF-BVII)


Simulation	Description	$K_{\text{eff}}$	** $K_{\text{eff}}$ Standard Deviation	*Rod worth [PCM]	**Rod worth Standard deviation
<b>Wallout</b>	All rods out	<b>0.9851</b>	0.00008	0	8.00
<b>Wallin</b>	All rods in	1.01121	0.00008	2611	11.31
<b>WCR1in</b>	S1 in	0.98901	0.00008	391	11.31
<b>WCR2in</b>	S2 in	0.98925	0.00008	415	11.31
<b>WSR1in</b>	SR1 in	0.99151	0.00008	641	11.31
<b>WSR2in</b>	SR2 in	0.9912	0.00008	610	11.31
<b>WRRin</b>	RR in	0.9879	0.00008	280	11.31

\*Rod worth is evaluated as the  $k_{\text{eff}}$  difference with respect to Wallin value (1st row, 3<sup>rd</sup> column, bold characters).

\*\* Rod worth standard deviation have been evaluated by simple consideration on error propagation.

Table 5 Reactivity estimation worth of the control rods of TAPIRO (JEFF 3.1)

Simulation	Description	$K_{\text{eff}}$	** $K_{\text{eff}}$ Standard Deviation	*Rod worth [PCM]	**Rod worth Standard deviation
<b>JWallout</b>	All rods out	<b>0.9809</b>	0.00008	0	8
<b>JWallin</b>	All rods in	1.00719	0.00008	2629	11.31
<b>JWCR1in</b>	S1 in	0.98522	0.00008	432	11.31
<b>JWCR2in</b>	S2 in	0.98512	0.00008	422	11.31
<b>JWSR1in</b>	SR1 in	0.98758	0.00008	668	11.31
<b>JWSR2in</b>	SR2 in	0.98711	0.00009	621	12.04
<b>JWRRin</b>	RR in	0.98393	0.00008	303	11.31

 <b>Ricerca Sistema Elettrico</b>	<b>Sigla di identificazione</b>	<b>Rev.</b>	<b>Distrib.</b>	<b>Pag.</b>	<b>di</b>
	NNFISS – LP3 - 047	0	L	18	101

The conclusions can be resumed as follow:

- 1) The sum of the individual rods worth (rows 3 to 7 in both Table 4 and Table 5) yields in a total worth of 2337 PCM for ENDFB-VII and 2446 PCM for JEFF-3.1. Conversely, the total insertion of all control rods (second row in both Table 4 and Table 5 ) yields a total rod worth 2611 PCM for ENDFB-VII and of 2629 PCM for JEFF-3.1. The two results differ of 170 PCM for ENDF and 86 PCM for JEFF. The discrepancy suggests, as expected, that multiple control rods insertion slightly enhance the total worth with a mechanism of mutual influence on neutron escape from core.
- 2) Both ENDF and JEFF simulation results are in relative good agreements with the experimental data of Table 3.
- 3) The  $K_{eff}$  values obtained using ENDF-BVII cross sections are bigger than the same values calculated using the JEFF3.1 cross sections, even if the differences are small. The rods worth obtained with ENDF-BVII and JEFF 3.1 cross sections are statistically consistent.

## Shim rods insertion by step

Another test has been carried out estimating the  $K_{\text{eff}}$  of the model for progressive insertion of both control rods, having safety rods totally extracted. The insertion step was, in all cases of 1 cm, and for each of the fifteen configurations a KCODE calculation has been performed. Table 6 and Table 7 report results for ENDF and Jeff cross sections. Figure 8 and Figure 9 report the tabulated data in graphical form.

**Table 6 Calibration rods worth for a progressive insertion of both CR1 and CR2 (Simulation carried out with ENDF-BVII cross sections at room temperature).**

Shim Rods length of insertion l [cm]	$K_{\text{eff}}$	Standard Deviation	$\Delta K_{\text{eff}}$ [PCM]	*Shim Rods Insertion range [cm]	$\Delta K_{\text{eff}}/\Delta l$ [PCM cm <sup>-1</sup> ]
0	0.99778	0.00008	0	--	--
1	0.99838	0.00008	60	0 - 1	60
2	0.99857	0.00008	79	1 - 2	19
3	0.9988	0.00008	102	2 - 3	23
4	0.99949	0.00008	171	3 - 4	69
5	0.99995	0.00008	217	4 - 5	46
6	1.00047	0.00008	269	5 - 6	52
7	1.00131	0.00008	353	6 - 7	84
8	1.00202	0.00008	424	7 - 8	71
9	1.00304	0.00008	526	8 - 9	102
10	1.00372	0.00008	594	9 - 10	68
11	1.00461	0.00008	683	10 - 11	89
12	1.00538	0.00008	760	11 - 12	77
13	1.00625	0.00008	847	12 - 13	87
14	1.00704	0.00008	926	13 - 14	79
15	1.00747	0.00009	969	14 - 15	9

\*Length Range of insertion for which the linear worth coefficient (last column) has been calculated.

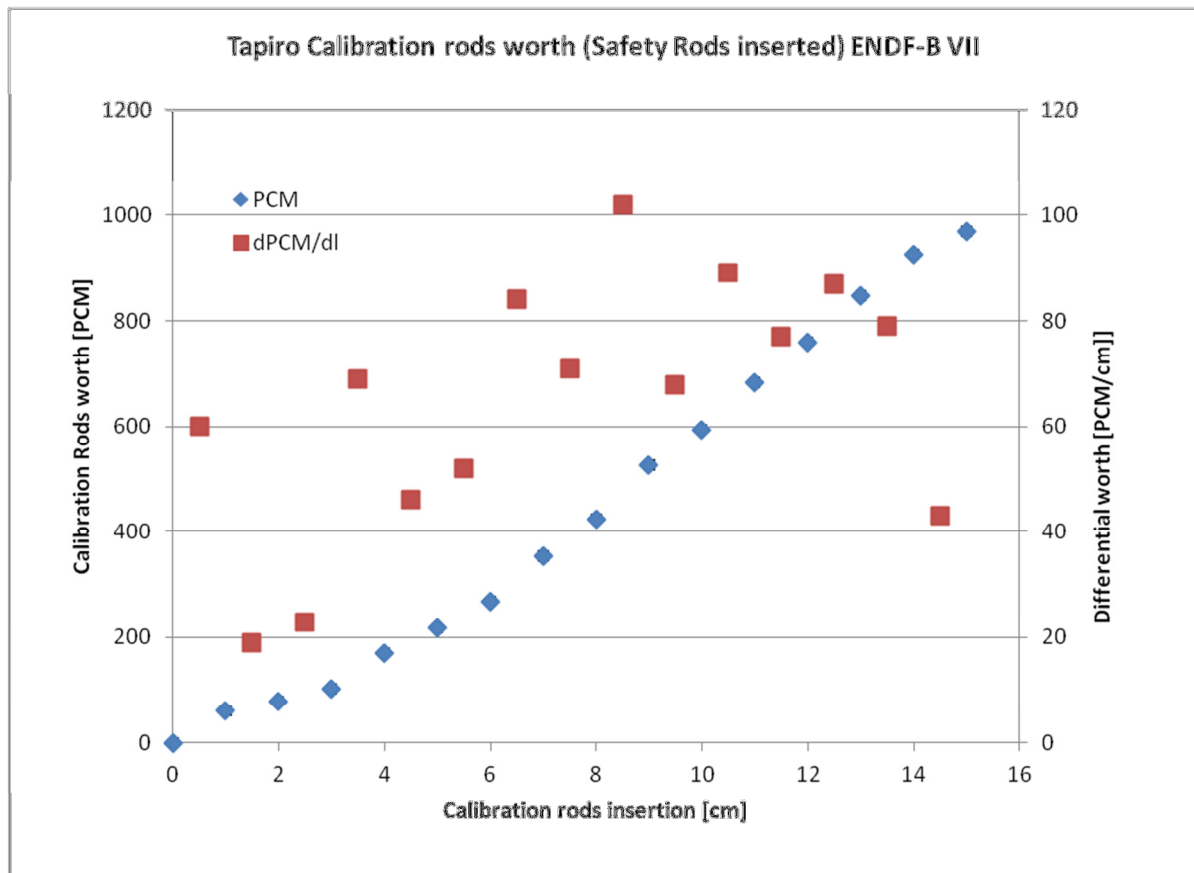


Figure 8 Reactivity worth for the progressive insertion of both shim Rods and its incremental ratio (ENDF-B VII nuclear data) when both Safety Rods are inserted

Table 7 rods worth for a progressive insertion of both CR1 and CR2 (Simulation carried out JEFF3.1 cross sections at room temperature)

Shim Rods length of insertion l [cm]	$K_{eff}$	Standard Deviation	$\Delta K_{eff}$ [PCM]	*Shim Rods Insertion range [cm]	$\frac{\Delta K_{eff}}{\Delta l}$ [PCM cm <sup>-1</sup> ]
0	0.99368	0.00008	0	--	0
1	0.99416	0.00008	48	0 - 1	48
2	0.9946	0.00008	92	1 - 2	44
3	0.99491	0.00008	123	2 - 3	31
4	0.99531	0.00008	163	3 - 4	40
5	0.99603	0.00008	235	4 - 5	72
6	0.99663	0.00008	295	5 - 6	60
7	0.99728	0.00008	360	6 - 7	65
8	0.99812	0.00008	444	7 - 8	84
9	0.99908	0.00008	540	8 - 9	96
10	0.99983	0.00008	615	9 - 10	75
11	1.00059	0.00009	691	10 - 11	76
12	1.00161	0.00009	793	11 - 12	102
13	1.0023	0.00008	862	12 - 13	69
14	1.00298	0.00008	930	13 - 14	68
15	1.00348	0.00008	980	14 - 15	50

\*Length Range of insertion for which the linear worth coefficient (last column) has been calculated.

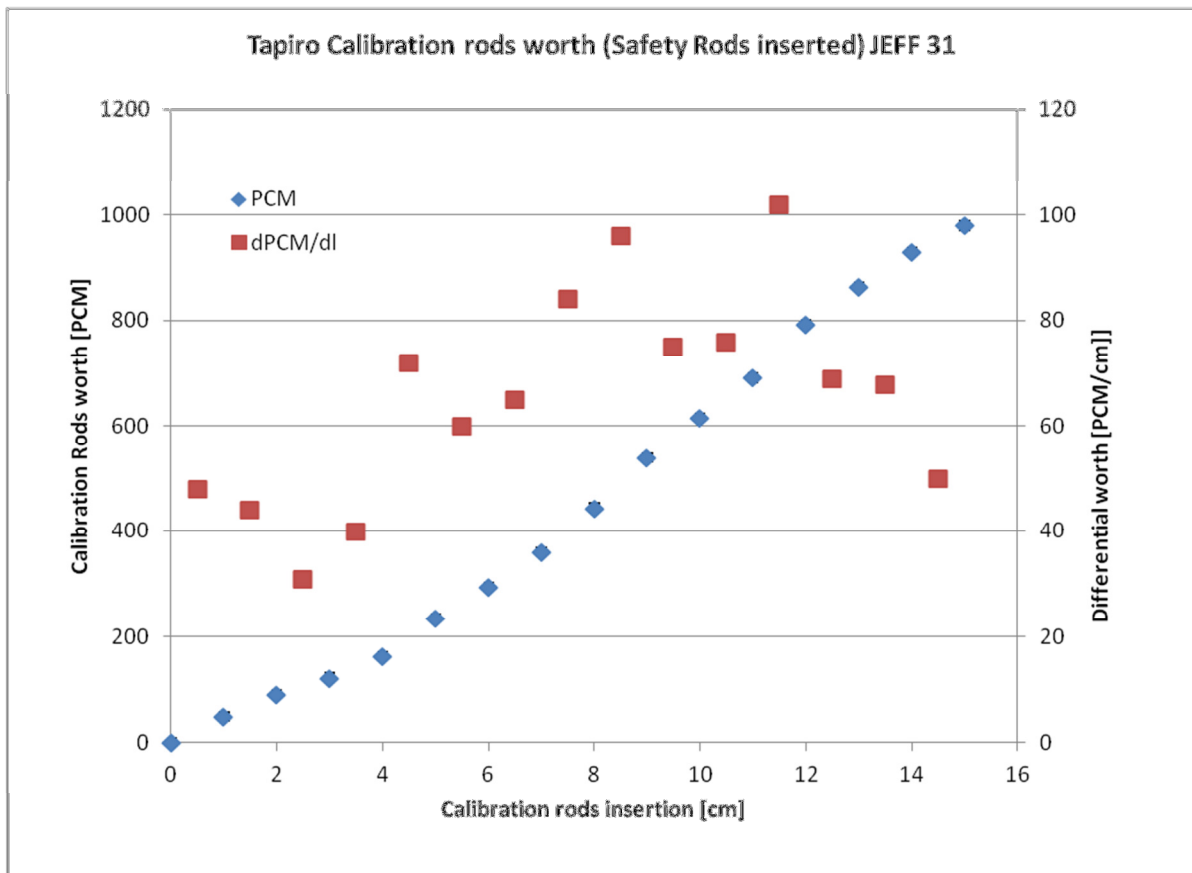


Figure 9 Reactivity worth for the progressive insertion of both shim Rods and its incremental ratio (JEFF3.1 nuclear data) when both Safety Rods are inserted

Both ENDFB-VII and JEFF3.1 estimated almost the same reactivity worth interval of 930-980 PCM. In the case of ENDFB-VII, 5 cm of rods insertion set the system to criticality. Conversely, with JEFF3.1, the system approaches the criticality with a rods insertion of 10-11 cm. As reported in Table 6 and Table 7, the maximum of reactivity worth obtained during the simulations is between 8-9 cm for ENDF and 10-11 cm for JEFF.

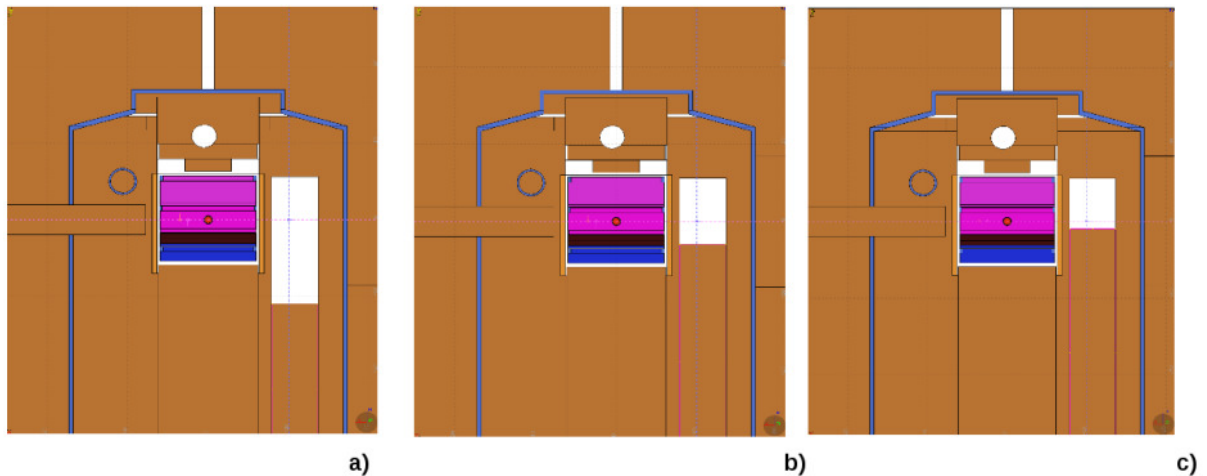


Figure 10 Control rod axial positions relative to core height: a) totally extracted rod, b) level of insertion compatible with the maximum worth ( $\Delta K_{eff}/\Delta l$  – see Table 6) in simulations with ENDF-BVII nuclear data , c) level of insertion compatible with the maximum worth change with length ( $\Delta K_{eff}/\Delta l$  – see Table 7) in simulations with JEFF3.1 nuclear data

Accordingly with Figure 10, the maximum insertion effect take place in ENDF simulations when the moveable core axial height is reached by the rod, conversely, for JEFF the same effects is obtained when the rods is inserted at the beginning of the axial height of the fixed core. A complete explanation of the differences between the two cross section dataset goes beyond the scope of the present report and future work will be addressed in this direction to explain the discrepancy.

### Test of the worth equivalence of control rods

In the late experimental campaign, fission chambers neutronic measurements has been performed in the irradiation channels reaching the criticality state with the rods positioned in different configurations. The leading idea for these measurements was the investigation of possible local flux perturbation induced by the different arrangements of the control rods. In the present reports similar configurations have been simulated at the sole purpose to tests the worth equivalence of the control rods. The following simulation scheme has adopted:

- 1) Assume as basis the criticality cases of Table 6 and Table 7.

- 2) For ENDF data set criticality will be re-obtained moving S1 around 4 cm and S2 around 6 cm of insertion. For JEFF 3.1 data set criticality will be re-obtained moving S1 around 9 cm and S2 around 11 cm of insertion. Safety rods remain completely inserted.
- 3) For ENDF data set criticality will be re-obtained moving S1 around 6 cm and S2 around 4 cm of insertion. For JEFF 3.1 data set criticality will be re-obtained moving S1 around 11 cm and S2 around 9 cm of insertion. Safety rods remain completely inserted.

Results are summarized in Table 8

**Table 8 ENDF-B VII and JEFF-3.1 simulations of the criticality with asymmetric insertion of the SHIM rods**

Simulations	Description	$K_{eff}$	$K_{eff}$ Standard Deviation	Cross Section
<b>LP3T2.5</b> (see Table 6)	Symmetric insertion of 5 cm for both S1 and S2	0.99995	0.00008	ENDF-BVII
<b>LP3T2.4.6</b>	Asymmetric insertion of Shims: S1 4 cm, S2 6 cm	1.00005	0.00008	ENDF-BVII
<b>LP3T2.6.4</b>	Asymmetric insertion of Shims: S1 6 cm, S2 4 cm	1.00004	0.00008	ENDF-BVII
<b>JLP3T2.10</b> (see Table Table 7)	Symmetric insertion of 10cm for both S1 and S2	0.99983	0.00008	JEFF-3.1
<b>JLP3T2.9.11</b>	Asymmetric insertion of Shims: S1 9 cm, S2 11 cm	0.99978	0.00008	JEFF-3.1
<b>JLP3T2.11.9</b>	Asymmetric insertion of Shims: S1 11 cm, S2 9 cm	0.99977	0.00008	JEFF-3.1

Both ENDF and JEFF simulations symmetrically compensated the worth variation re-gaining criticality. Since the results from Table 4 and Table 5 indicated that control rods effects are almost linear (excess of reactivity worth from rods mutual interaction is of the order of 170-86 PCM), the worth equivalence of the control rods is verified and prove, at least for little rod insertion, the model consistency.

## **Comparison of criticality data of the late experimental campaign with the TAPIRO model outcomes**

In Volume 2, Figure 8.2.4, of the reference [2] two criticality states have been experimentally obtained with different levels of insertion of S1,S2 and RR rods with and without a fuel pellets at the



center of diametrical channel (in core position). The criticality has been obtained with an insertion 10 cm of both Shims (RR inserted for 0.55 cm). Conversely, when no fuel pellets was present, the Shims were inserted for 10 cm (RR insertion 7 cm). The rods configuration compatibles with the experimental criticality states have been reproduced in the following simulations:

**Table 9  $K_{eff}$  estimations with SHIM and Calibration rods positions suggested by the report on the late TAPIRO experimental campaign (FIG: 8.2.4 of the report)**

Simulation	Description	$K_{eff}$ estimation					
		ENDF			JEFF31		
		$K_{eff}$	Std. Dev	$\Delta K_{eff}$ [PCM]	$K_{eff}$	Std. Dev	$\Delta K_{eff}$ [PCM]
<b>WithFuel</b>	Shim rods at 10 cm of insertion, RR at 0.55. Fuel Pellet in Diametrical channel.	1.00476	0.00008	476	1.00098	0.00008	98
<b>Nofuel</b>	Shim rods at 10 cm of insertion, RR at 7 cm. No Fuel Pellet.	1.00504	0.00008	504	1.00108	0.00008	108

Table 9 reports the results of the criticality simulations for the two experimental configurations carried out with both ENDF-B-VII and JEFF31 neutron cross section data sets. It is evident that both data sets tend to estimates as supercritical the experimental configuration. ENDF-BVII shows a greater level of discrepancy (500 PCM) whereas the JEFF3.1 is significantly less (100 PCM). As consequence of these results, the next simulations were carried out with JEFF3.1 without fuel pellets in the diametrical channel.

## Estimation of the neutron flux spectrum in various position of the radial, tangential and diametrical channel by using F5 detectors tallies

A preliminary estimation on the neutron flux intensity and spectrum in Tangential, Diametrical, and Radial 1 channels has been carried out in the simulation describe in Table 10 by using F5 detector tallies (see page 12).

**Table 10 Main characteristics of the simulation run for the estimation of the neutron energy spectrum**

Simulations	Description
<b>NofuelFlux</b>	SHIM rods at 10 cm of insertion, regulation at 7 cm. No Fuel Pellet. Jeff31 cross sections. F5 tallies for the estimation of neutron flux with a 5 energy bins representation. 1000 Kcode cycles.

Table 11 to Table 13 report the energy distribution of the neutron flux in a five energy bins representation for Diametrical, Tangential and Radial 1 channels. Figure 11, Figure 13 and Figure 15 report the neutron spectrum, normalized at its own total, for each examined channel. Figure 12, Figure 14 and Figure 16 report the previous normalized spectrum in logarithmic scale.

**Table 11 Five bins representation of the energy distribution of the neutron flux in various positions of the diametrical channel**

*Distance [cm]	-55	-45	-35	-25	-15	0	+15	+25	+35	+45	+55
<b>E bins [MeV]</b>	<b>Neutron Fluence [n/cm2/s.p.]</b>										
<b>1.00E-07</b>	1.27E-08	2.95E-08	1.03E-08	5.26E-13	2.77E-19	3.04E-26	2.30E-12	6.59E-13	9.16E-11	2.45E-08	9.85E-09
<b>5.00E-03</b>	5.73E-06	2.05E-05	2.31E-05	3.45E-05	4.32E-05	3.10E-06	4.16E-05	3.27E-05	2.29E-05	1.96E-05	5.09E-06
<b>1.00E+00</b>	2.45E-06	2.55E-05	1.46E-04	4.46E-04	1.19E-03	4.06E-03	1.21E-03	4.48E-04	1.41E-04	2.53E-05	2.48E-06
<b>2.00E+01</b>	7.55E-08	2.26E-07	1.74E-06	1.34E-05	1.13E-04	3.07E-03	1.19E-04	1.39E-05	1.79E-06	2.71E-07	5.28E-08
<b>Total</b>	8.27E-06	4.62E-05	1.71E-04	4.93E-04	1.34E-03	7.14E-03	1.37E-03	4.95E-04	1.66E-04	4.53E-05	7.63E-06

\* For radial and diametrical channel distance on channel axis taking origin in the intersection of core axis with channel axis. For tangential channel the origin is the intersection of the translation of the core axis (- 10.6 cm along y-axis of MCNP reference system) with the channel axis.

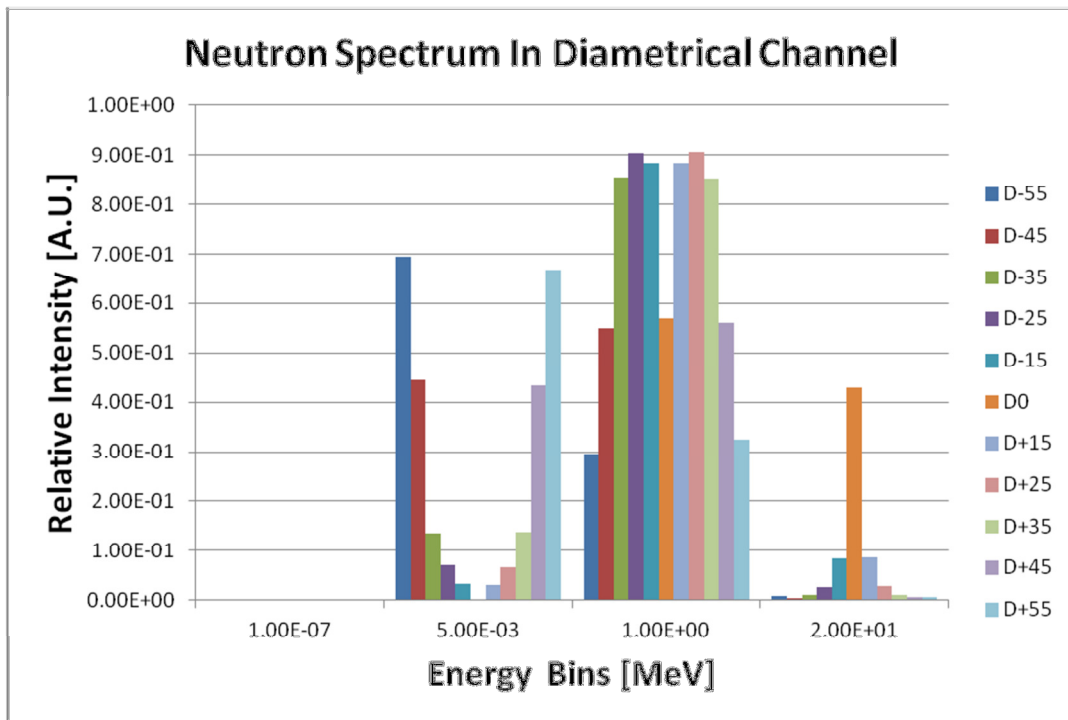


Figure 11 Five energy bins representation of the normalized neutron spectrum at various distances from the core axis along the diametrical channel

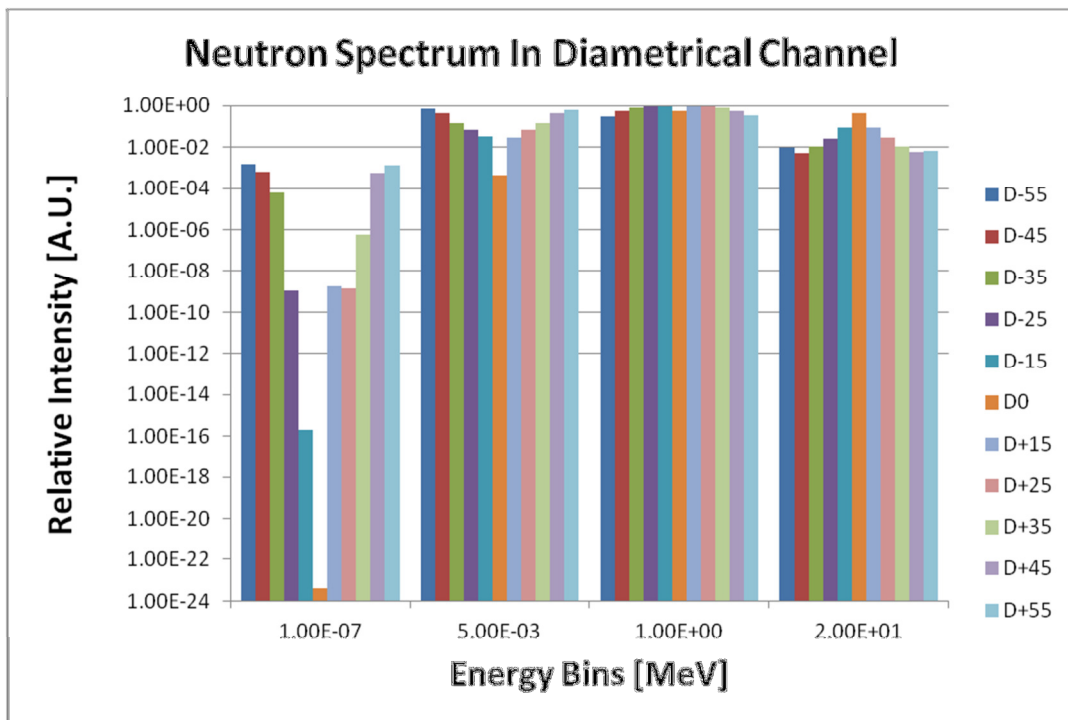


Figure 12 Five energy bins representation of the normalized neutron spectrum at various distances from the core axis along the diametrical channel (Intensity is in logarithmic scale)

The neutron spectrum in the selected points of the diametrical channel is characterized by a progressive transition from a nearly fission spectrum in the in core position of the channel to a progressive softening in its peripheral position. The thermal neutron population that is negligible at core center progressively growth with the detector distance from the core axis. This last finding clearly indicates, at least for the simulation conditions, a elevated symmetry of the two halves of the channel.

Table 12 Five bins representation of the energy distribution of the neutron flux in various positions of the Tangential channel.

*Distance [cm]	-50	-40	-30	-20	-10	0	+10	+20	+30	+40	+50
E bins [MeV]	Neutron Fluence [n/cm2/s.p.]										
1.00E-07	3.67E-08	7.11E-09	4.20E-10	6.65E-15	8.40E-20	8.77E-13	2.21E-12	1.53E-11	1.94E-11	8.91E-09	2.67E-08
5.00E-03	9.30E-06	2.08E-05	2.69E-05	3.77E-05	4.73E-05	4.54E-05	4.65E-05	3.87E-05	2.61E-05	2.01E-05	7.90E-06
1.00E+00	5.54E-06	5.27E-05	2.09E-04	5.39E-04	1.13E-03	1.66E-03	1.15E-03	5.33E-04	2.06E-04	5.11E-05	6.54E-06
2.00E+01	8.10E-08	4.65E-07	3.32E-06	2.04E-05	1.02E-04	2.68E-04	1.05E-04	1.88E-05	3.05E-06	3.93E-07	7.10E-08
Total	1.50E-05	7.40E-05	2.39E-04	5.97E-04	1.28E-03	1.97E-03	1.30E-03	5.91E-04	2.35E-04	7.17E-05	1.20E-05

\* For radial and diametrical channel distance on channel axis taking origin in the intersection of core axis with channel axis . For tangential channel the origin is the intersection of the translation of the core axis (- 10.6 cm along y axis of MCNP reference system) with the channel axis.

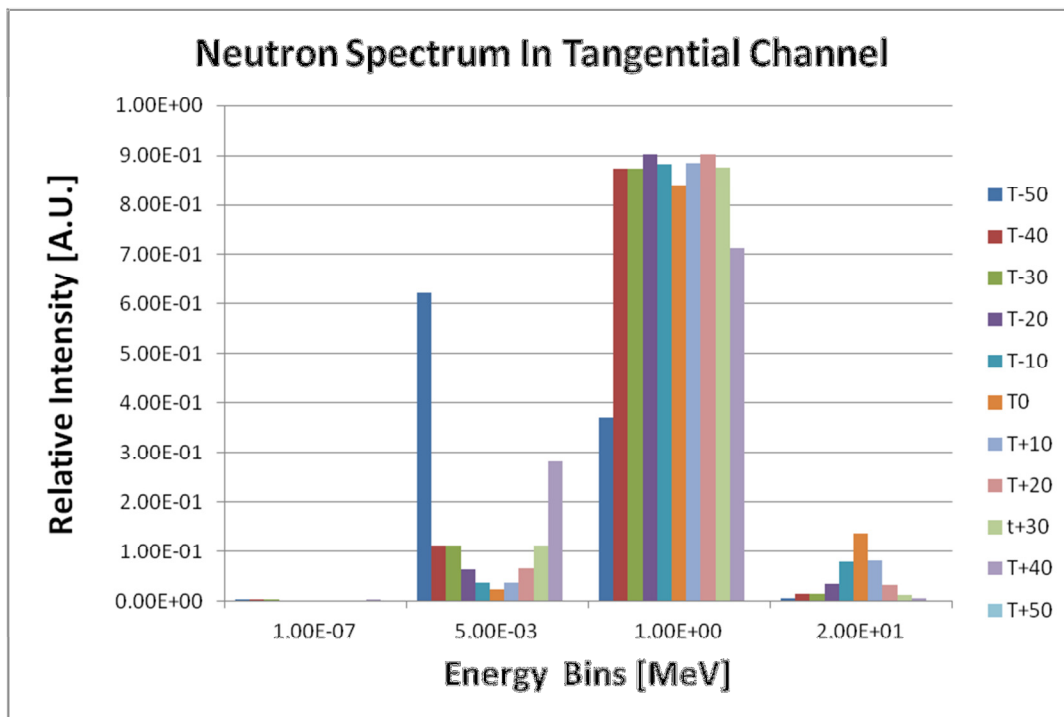


Figure 13 Five energy bins representation of the normalized neutron spectrum at various distances from the core axis along the tangential channel.

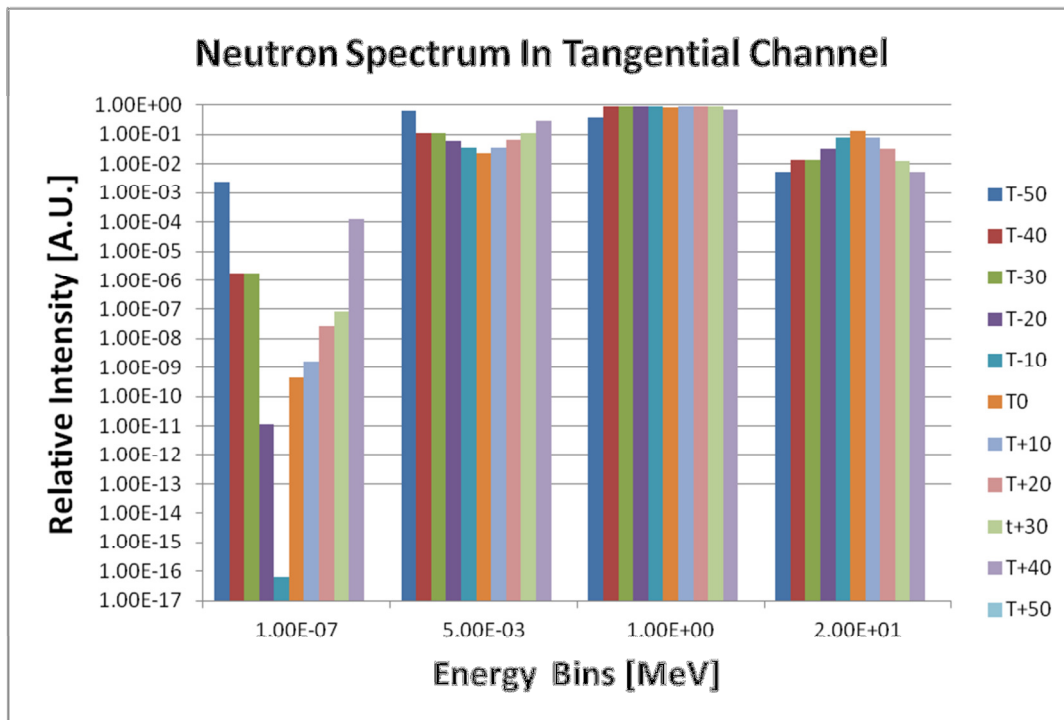


Figure 14 Five energy bins representation of the normalized neutron spectrum at various distances from the core axis along the tangential channel axis (Intensity is in logarithmic scale)

As expected, the intensity of the neutron flux in the central position (T0) of the tangential channel shows a intensity decrease of a factor 3.5 compared to the homologues position of the diametrical channel. The neutron spectrum retains the feature of a progressive softening from the “central” to the peripheral positions. Again, the thermal neutron population is negligible at the center of the core and become progressively increase with the distance from the core axis.

Table 13 Five bins representation of the energy distribution of the neutron flux in various positions of the Radial 1 channel.

*Distance [cm]	8.55	15	25	35	45	55
E bins [MeV]	Neutron Fluence [n/cm2/s.p.]					
1.00E-07	3.53E-20	2.19E-12	4.31E-11	1.44E-09	2.64E-08	1.34E-08
5.00E-03	4.18E-05	4.79E-05	3.89E-05	2.67E-05	1.94E-05	5.48E-06
1.00E+00	2.17E-03	1.20E-03	4.51E-04	1.48E-04	2.85E-05	3.12E-06
2.00E+01	6.22E-04	1.56E-04	2.36E-05	4.75E-06	1.36E-06	2.42E-07
Total	2.83E-03	1.41E-03	5.14E-04	1.79E-04	4.93E-05	8.85E-06

\* For radial and diametrical channel distance on channel axis taking origin in the intersection of core axis with channel axis . For tangential channel the origin is the intersection of the translation of the core axis (- 10.6 cm along y axis of MCNP reference system) with the channel axis.

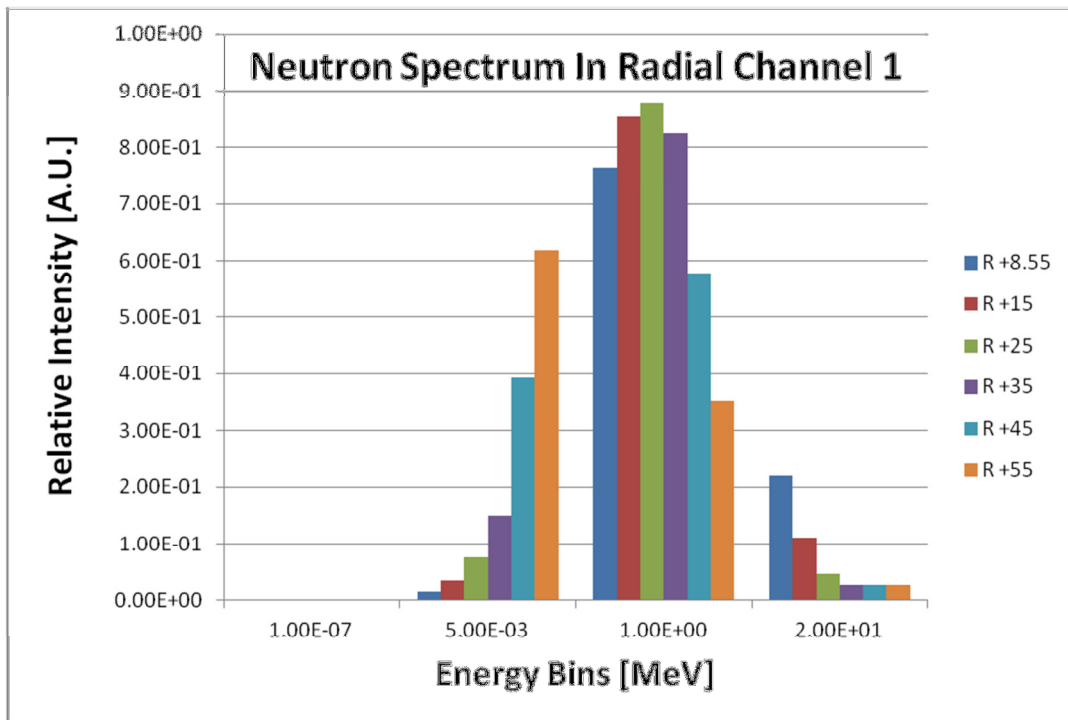


Figure 15 Five energy bins representation of the normalized neutron spectrum at various distances from the core axis along the Radial channel 1 axis.

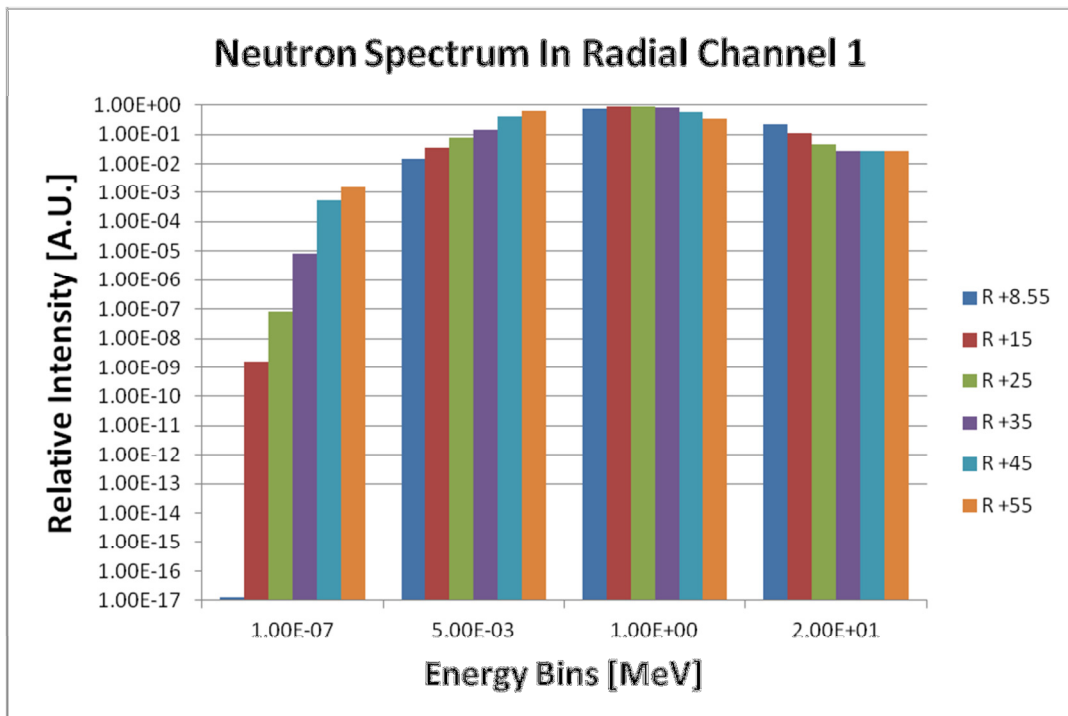



Figure 16 Five energy bins representation of the normalized neutron spectrum at various distances from the core axis along the radial channel 1 axis (Intensity is in logarithmic scale)

	<b>Sigla di identificazione</b> NNFISS – LP3 - 047	<b>Rev.</b> 0	<b>Distrib.</b> L	<b>Pag.</b> 30	<b>di</b> 101
---	---	------------------	----------------------	-------------------	------------------

The intensity of the neutron flux in the position 8.55 of the radial channel 1 is, roughly, 2 order of magnitude lower than the one estimated in position 0 of the diametrical channel. The neutron spectrum shows a progressive softening as the distance from the core axis increases. Also in this channel, the thermal neutron population is negligible in the near core position and increases with distance from core axis.



## Comparison of the neutron fluxes with experimental findings of late experimental campaign

Reference [2] reports an estimation of some neutron flux spectral properties derived from the experimental findings. Originally, such estimations have been normalized to 5 kW of reactor power and refer to a high symmetric (spherical) model of the reactor. A good basis for comparison of this data is with the neutron fluxes responses obtained in the diametrical channel in the present simulation. Table 14 reports the comparison of the spectral properties for the flux intensity greater than 100 keV and 1 MeV. Data have been normalized at their own maximum.

Table 14 Comparison of experimental-derived (Table 2.1 Vol 1 reference [2]) and estimated data

Late Report			MCNPX		
Dist	Norm Flux > 1 MeV	Norm Flux > 100 KeV	Dist	Norm Flux > 1 MeV	Norm Flux > 100 KeV
0	0.4364	0.9545	0.000	0.6467	0.9793
10.4	0.1833	0.8350	15.000	0.2477	0.8034
20.6	0.0632	0.6842	25.000	0.0441	0.6568
30.4	0.0200	0.5143	35.000	0.0644	0.5275

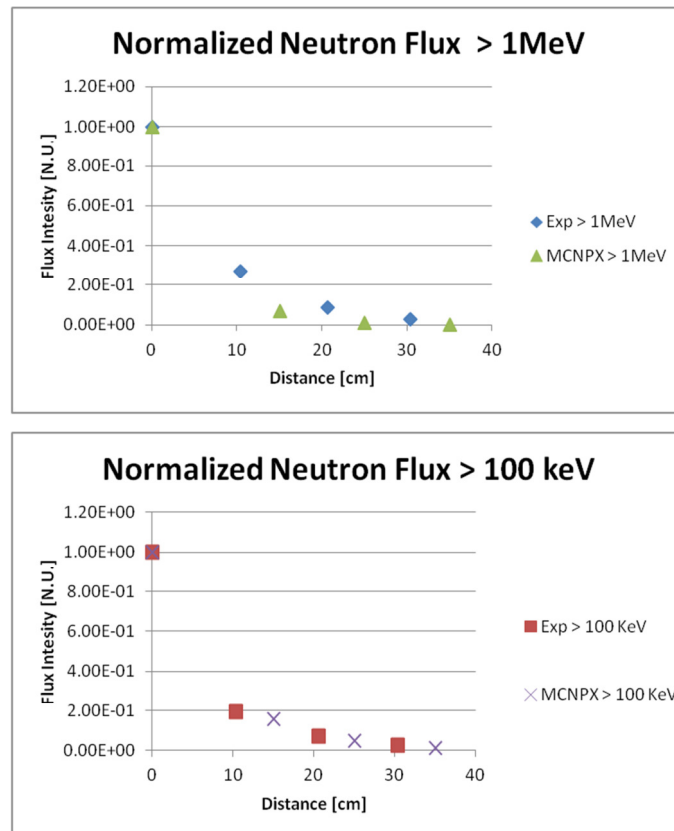


Figure 17 Comparison of experimental and estimated normalized partial neutron fluxes for neutrons.

Taking into account that, except for the 0 position, actual MC-simulated data and late campaign data refers to slightly different position the agreement is satisfactory.

Table 15 Comparison of total neutron flux intensities

Late Report Ref. [2] Table 2.1 Vol. 1		MCNPX	
Dist	Total Norm Flux	Dist	Total Norm flux
0	1.00E+00	0.000	1.00E+00
10.4	2.73E-01	15.000	1.92E-01
20.6	8.64E-02	25.000	6.93E-02
30.4	3.18E-02	35.000	2.33E-02

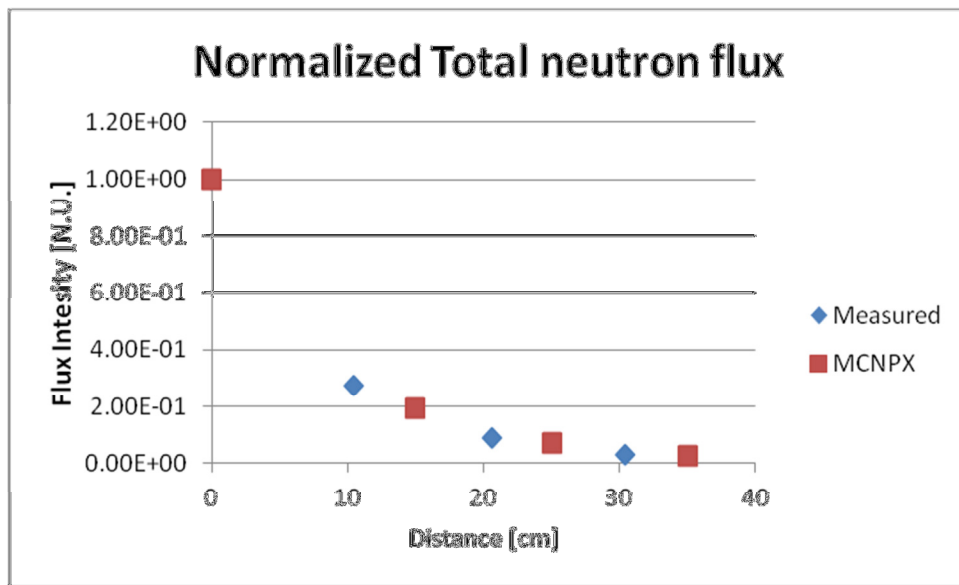


Figure 18 Comparison of total neutron flux intensities

Concerning the comparison of the total intensity of the neutron flux vs. distance from core axis (see Table 15 and Figure 18) the data are in good agreement.

## Fission rate Traverses

Fission traverses have been estimated by using both mesh tallies (type 1 estimators) and detectors (F5 MCNPX Tally type) along the axes of diametrical, radial, and tangential channel. The fissionable nuclides used in the estimations are  $^{235}\text{U}$ ,  $^{238}\text{U}$ ,  $^{239}\text{Pu}$  and  $^{237}\text{Np}$ . It would be useful to recall the fission modality of the selected isotopes to gains some insight in their fission rate answers.

Table 16 reports the comparison of the total fission probability for  $^{239}\text{Pu}$ ,  $^{235}\text{U}$ ,  $^{237}\text{Np}$  and  $^{238}\text{U}$  from the JEFF3.1.1 data files (see Figure 19 and

Figure 20) condensed in a four bin representations. Since all the isotope have been used in very thin foils in fission chambers, it is useful to compare the sole total fission cross sections neglecting scattering and capture transport phenomena (an almost ideal detector approach).

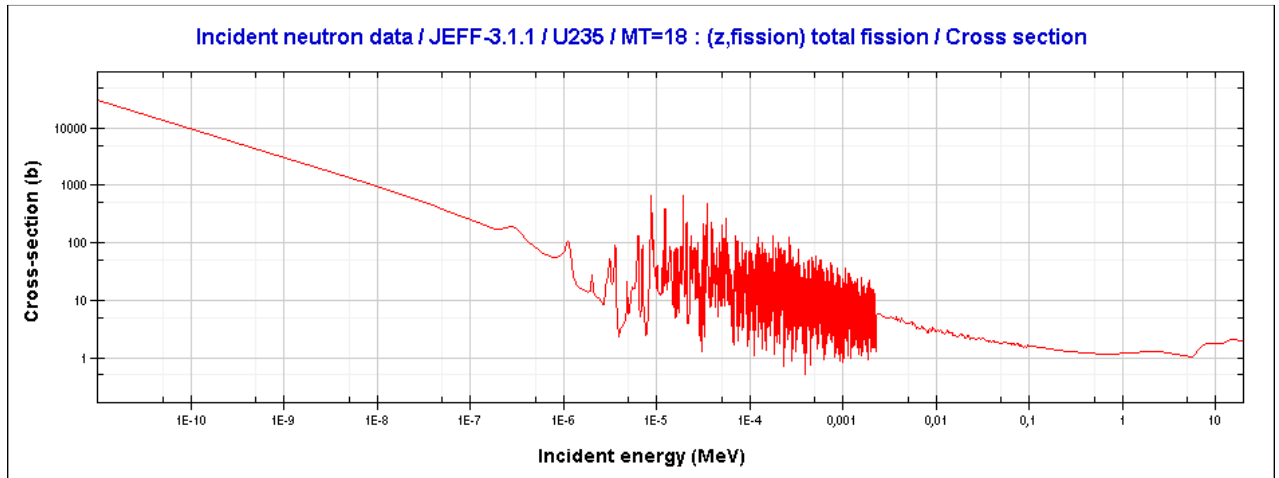
**Table 16 Four energy bins representation of the total fission cross section for the Fissile materials used in the fission rate traverses.**

Isotope	Integral Cross section	Energy Bins			
		0 - 0.1eV	0.1 eV - 5KeV	5 KeV - 1 MeV	1 - 20 MeV
<b>U235</b>	[Barn]	9.06E+05	5.56E+05	5.09E+02	1.53E+02
	*Norm.	61.94%	38.02%	0.03%	0.01%
<b>U238</b>	[Barn]	3.76E-02	1.41E+01	9.69E+00	1.56E+02
	Norm.	0.02%	7.84%	5.39%	86.75%
<b>Pu239</b>	[Barn]	9.58E+05	6.79E+05	3.05E+02	3.37E+02
	Norm.	58.51%	41.45%	0.02%	0.02%
<b>Np237</b>	[Barn]	2.74E+01	2.91E+02	4.78E+01	4.25E+02
	Norm.	3.46%	36.77%	6.04%	53.72%

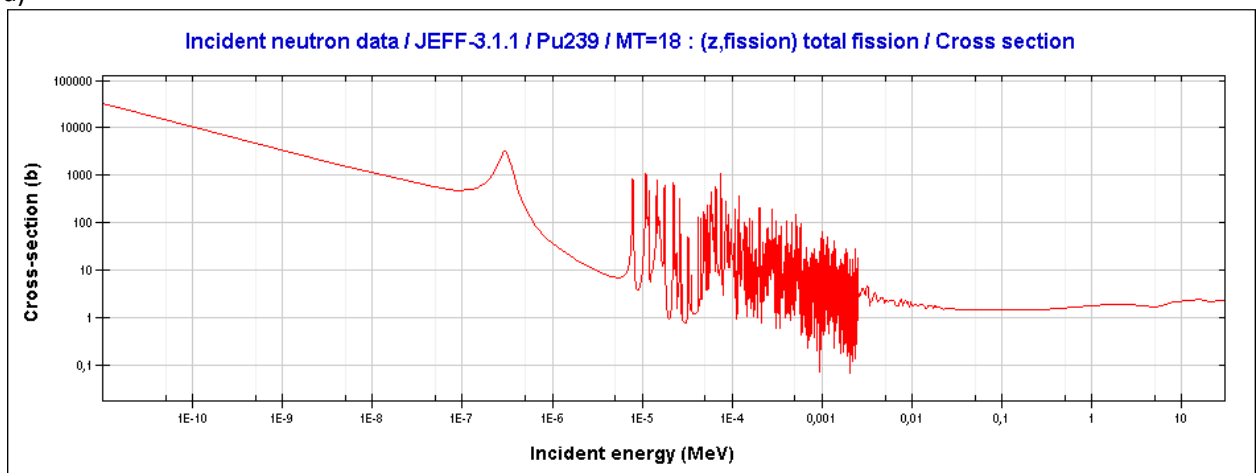
\*Percentage relative to the integrated response on the whole energy interval (up to 20 MeV)

Basically,  $^{239}\text{Pu}$  and  $^{235}\text{U}$  detect thermal and epithermal neutrons with very high efficiency but are also able to detect fast and high energy neutrons practically in the entire considered energy range.

$^{237}\text{Np}$  shows a detection efficiency that progressively increases with the energy of the neutrons.  $^{238}\text{U}$  has his best detection efficiency for the high-energy neutrons.

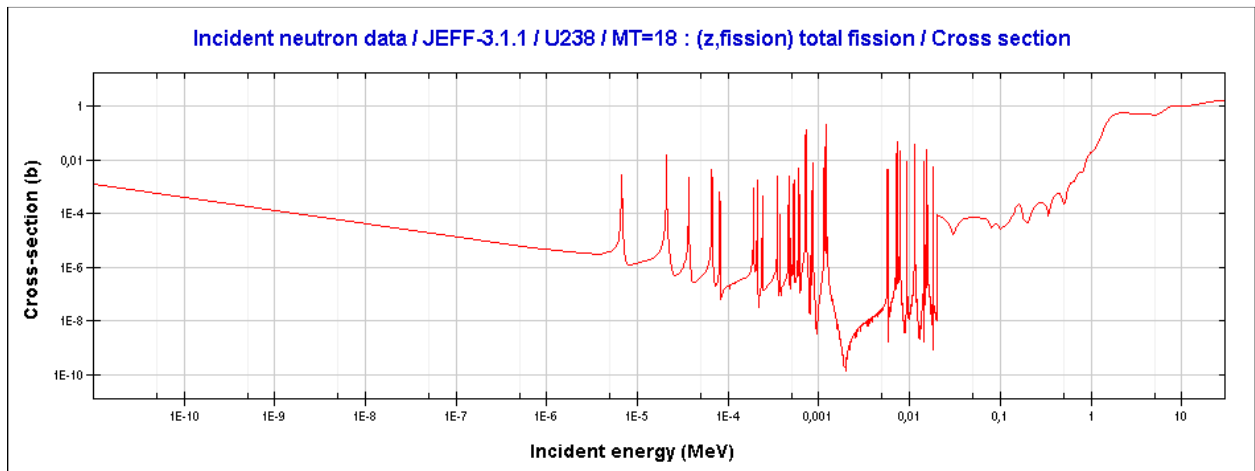


a)

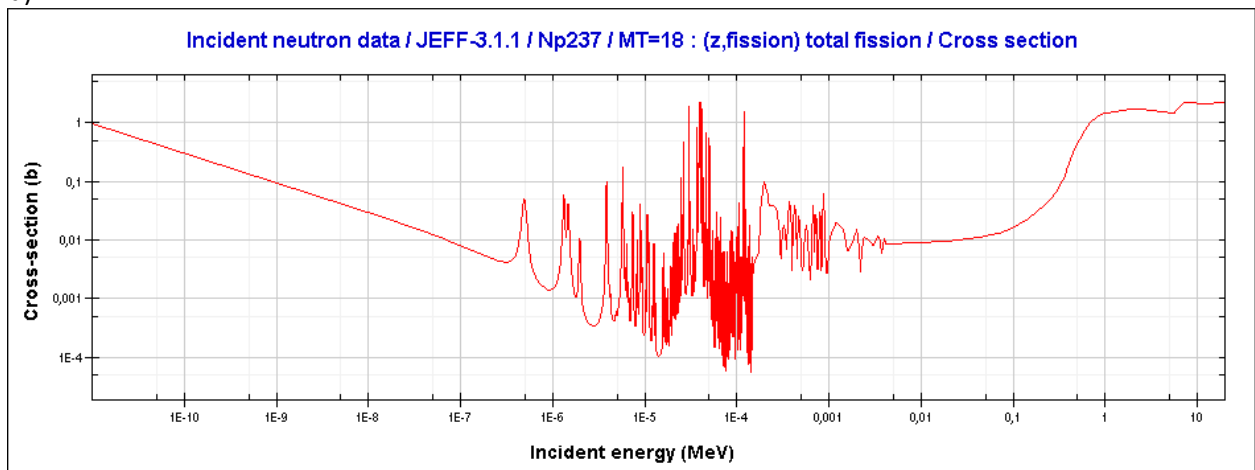


b)

Figure 19: Total fission cross sections for <sup>235</sup>U (a) and <sup>239</sup>Pu (b) from the Janis Database [7].



a)




b)

Figure 20 Total fission cross sections for <sup>238</sup>U (a) and <sup>237</sup>Np (b) from the Janis Database [7].

## MESH Tally fission traverses

Fission rate has been estimated along traverses on the axis of the diametrical, tangential, and radial1 channels by using the mesh tally estimators. In order to avoid great uncertainties in the response of the mesh tally estimator a tradeoff study between mesh volumes and tally relative error has been carried out and the optimal mesh volume (Cartesian mesh) of 1X1X1 cm<sup>3</sup> has been adopted. The simulation features are reported in Table 17.

 <b>ENEA</b> Ricerca Sistema Elettrico	<b>Sigla di identificazione</b>	<b>Rev.</b>	<b>Distrib.</b>	<b>Pag.</b>	<b>di</b>
	NNFISS – LP3 - 047	0	L	36	101

**Table 17 Simulations plan for the fission rate traverses in Tangential, Diametrical and Radial 1 channels of TAPIRO (voxel volume 1X1X1 cm<sup>3</sup>)**

Simulations	Description
<b>ALLTgRdDiBig</b>	Mesh Tally for <sup>239</sup> Pu, <sup>237</sup> Np, <sup>238</sup> U and <sup>235</sup> U in tangential, radial and diametrical channels. Voxel dimensions are 1X1X1 cm <sup>3</sup> . Traverses range: from -55 to +55 cm in Diametrical channel, from -50 to +50 cm in Tangential channel, from 8.55 to 60 cm in Radial 1 channel. No pellets in Diametrical channel. JEFF31 cross section dataset. 4000 iterations for KCODE.

Figure 21 to Figure 26 report the fission traverses for the diametrical, tangential and radial channels.

Each figure also reports a schematic representation of the irradiation channel under consideration

with a scale in centimeter that allows the proper localization of the traverses.

*Diametrical channel*

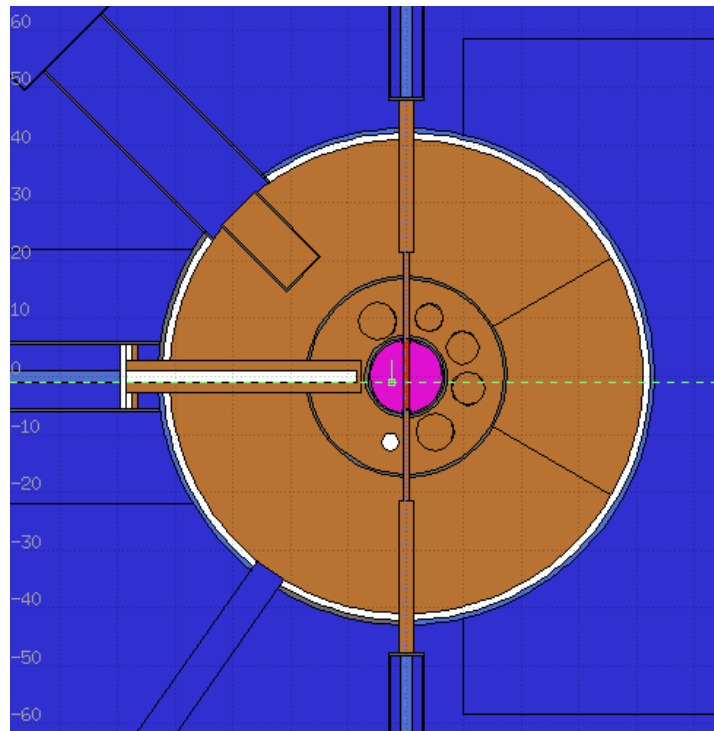
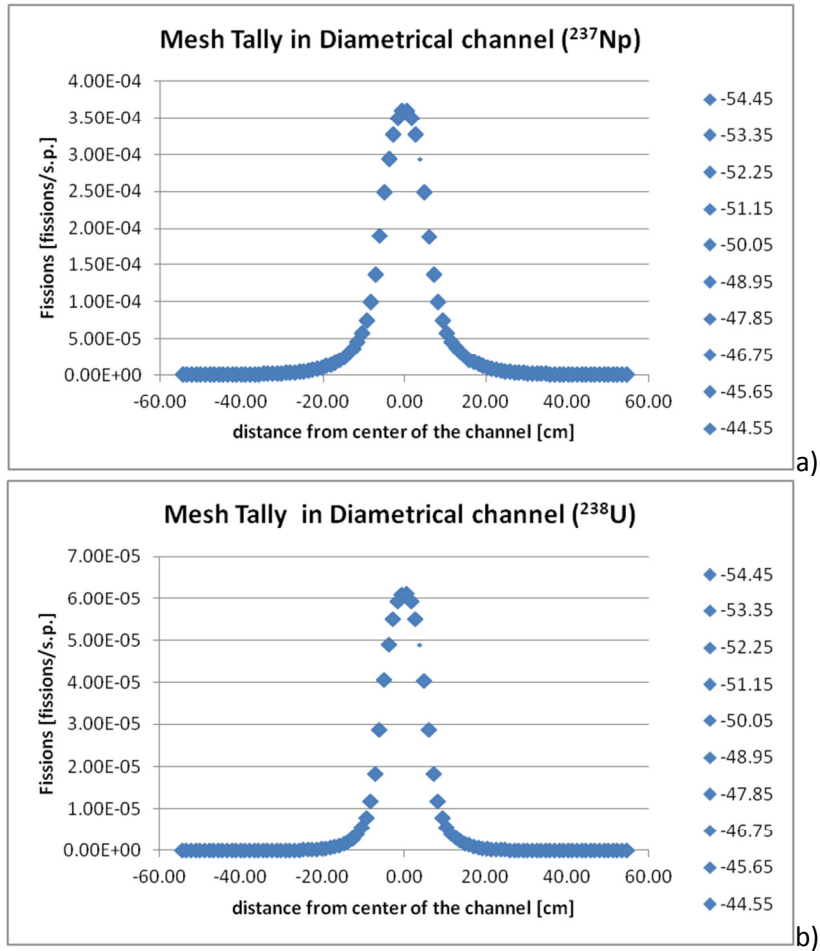


Figure 21: Fission rate on mesh tally for <sup>237</sup>Np (a), <sup>238</sup>U (b) in the diametrical channel of TAPIRO (JEFF31 data set, no pellet, Mesh voxel 1x1x1 cm<sup>3</sup>).

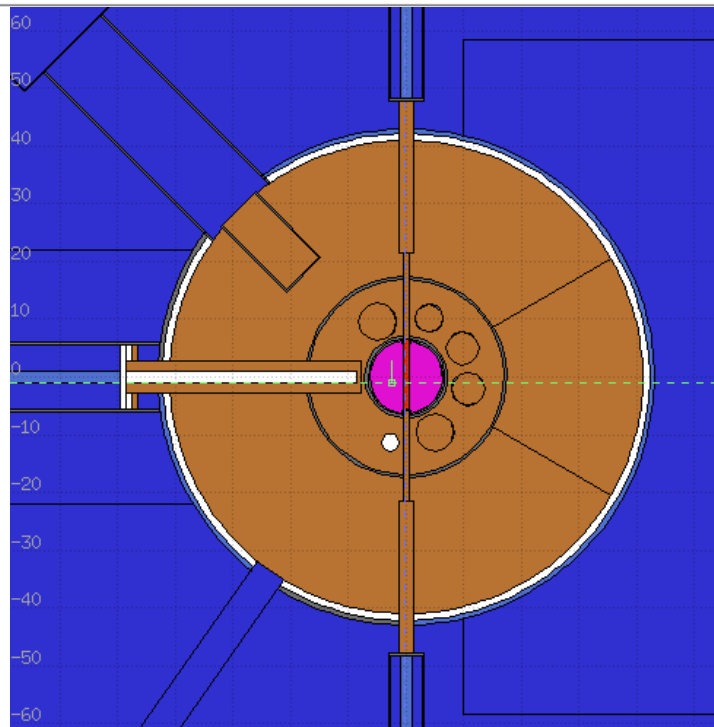
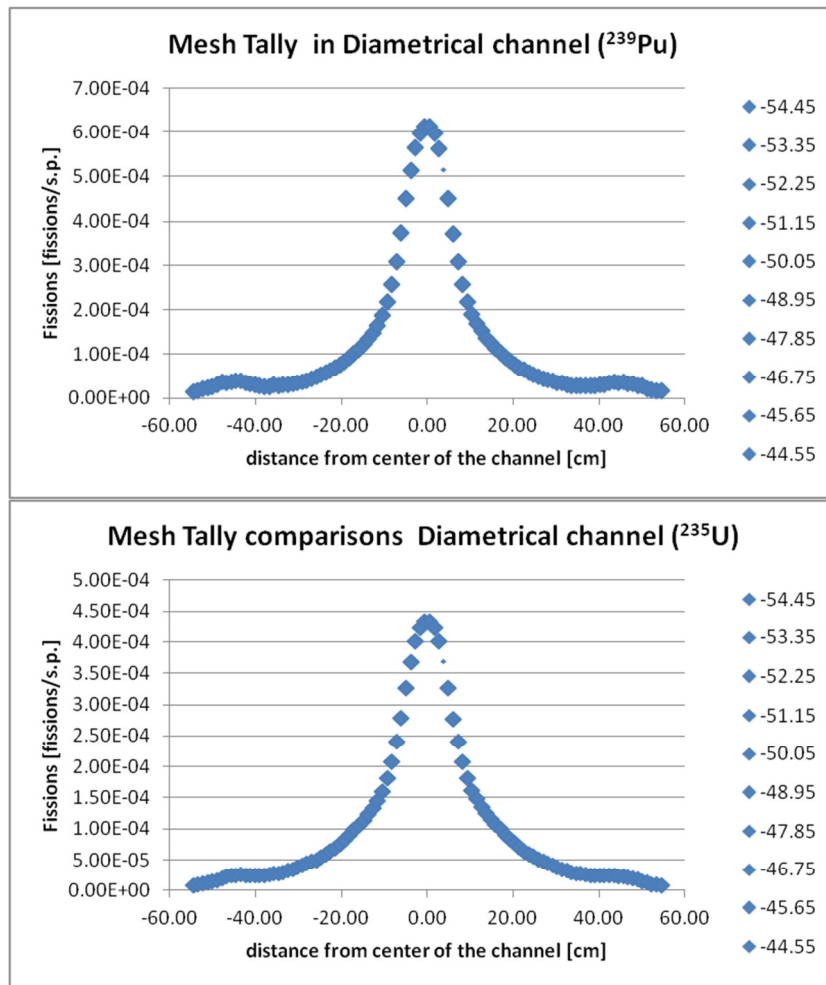


Figure 22 Fission rate on mesh tally for <sup>239</sup>Pu (a), <sup>235</sup>U (b) in the diametrical channel of TAPIRO (JEFF31 data set, no pellet, Mesh voxel 1x1x1 cm<sup>3</sup>).



Radial channel

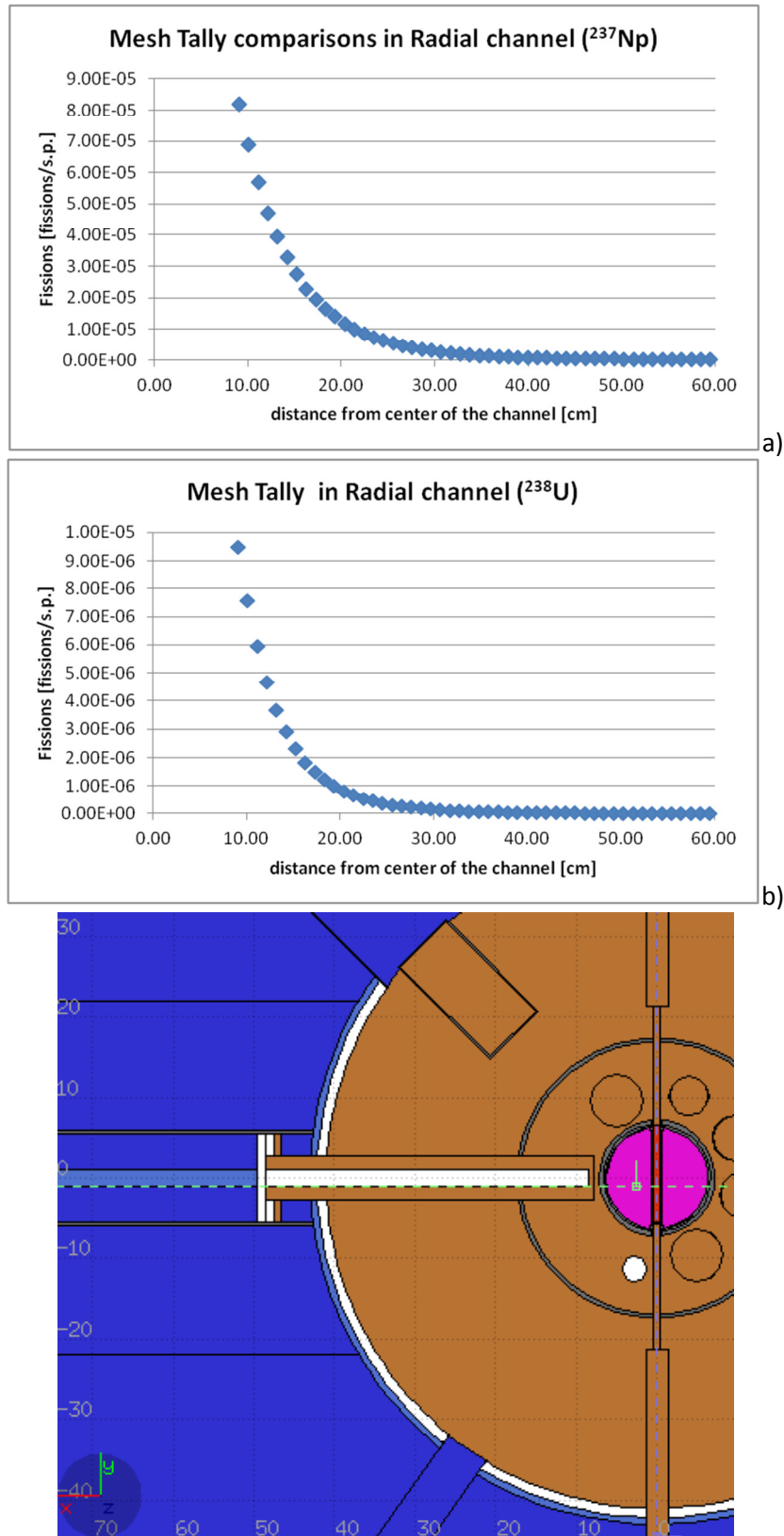
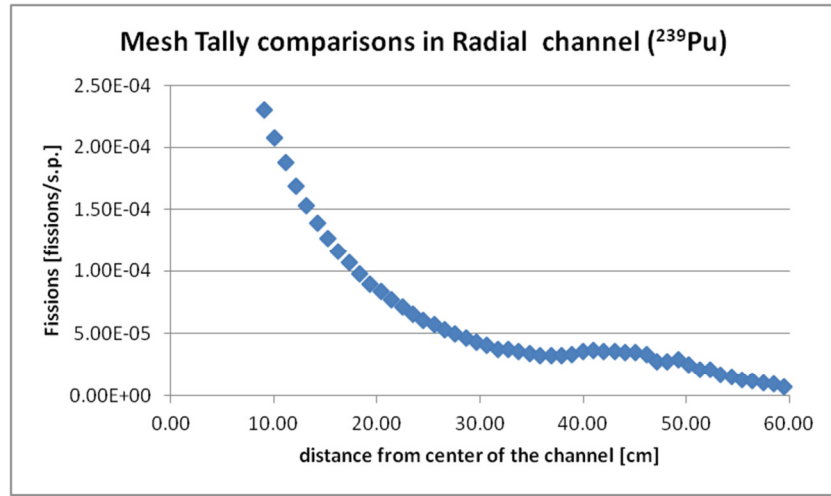
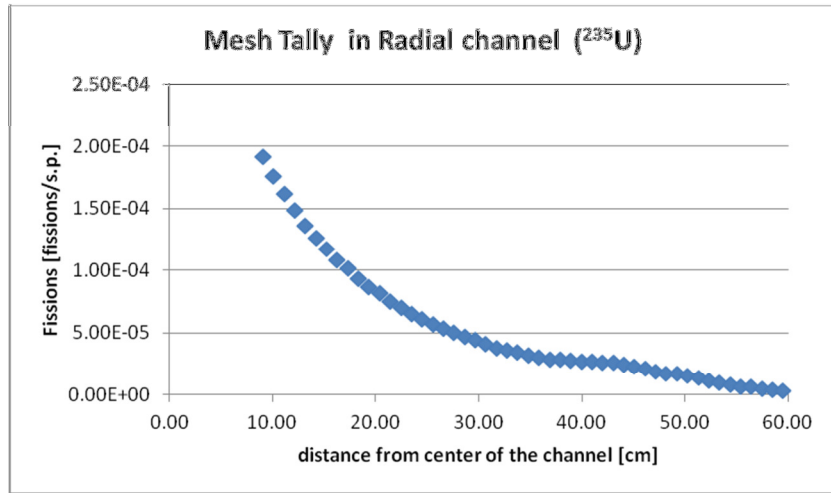


Figure 23 Fission rate on mesh tally for  $^{237}\text{Np}$  (a),  $^{238}\text{U}$  (b) in the radial channel of TAPIRO (JEFF31 data set, no pellet, Mesh voxel  $1\text{x}1\text{x}1\text{ cm}^3$ )



a)



b)

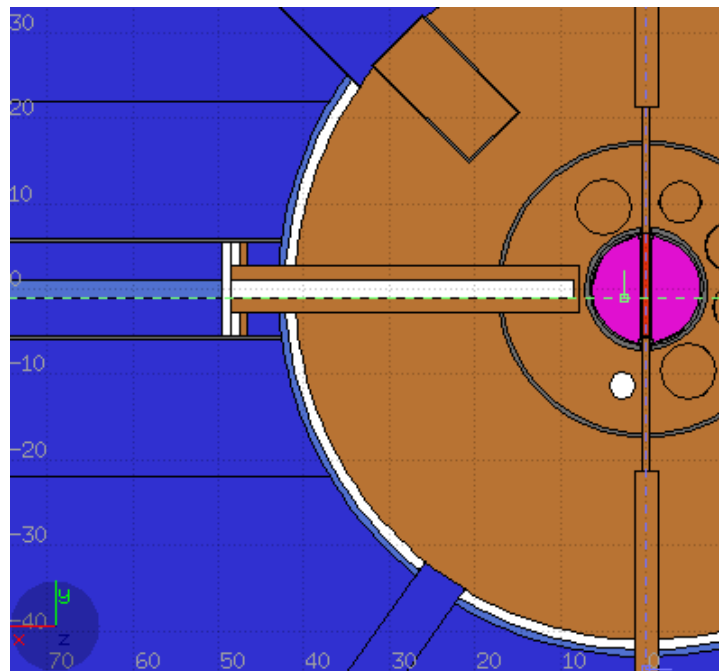


Figure 24 Fission rate on mesh tally for <sup>239</sup>Pu (a) and <sup>235</sup>U (b) in the radial channel of TAPIRO (JEFF31 data set, no pellet, Mesh voxel 1x1x1 cm<sup>3</sup>)

*Tangential Channel*

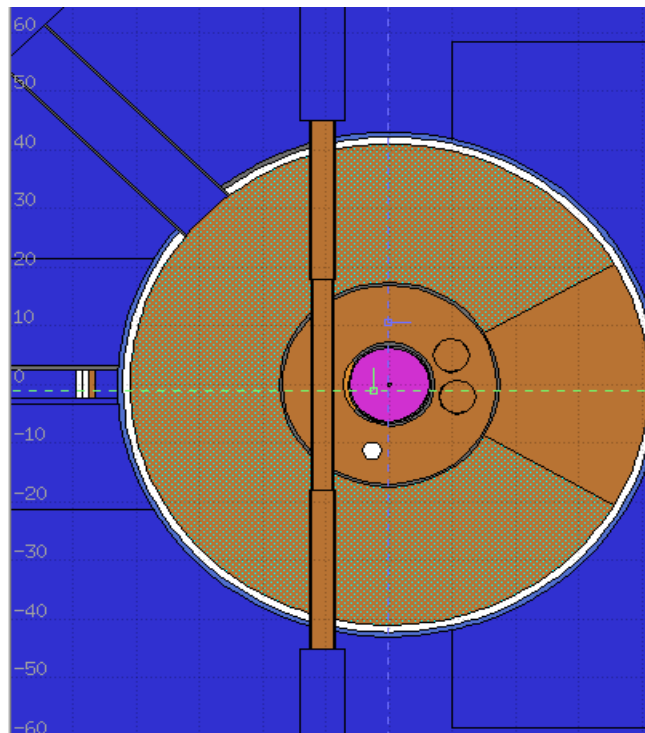
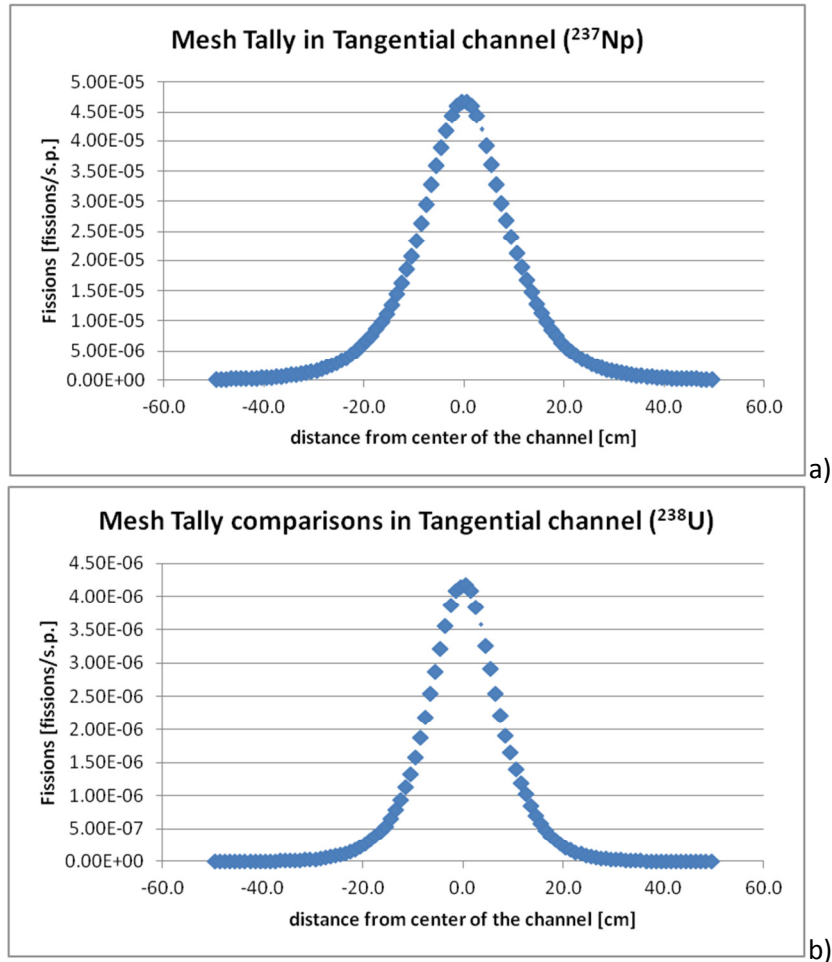
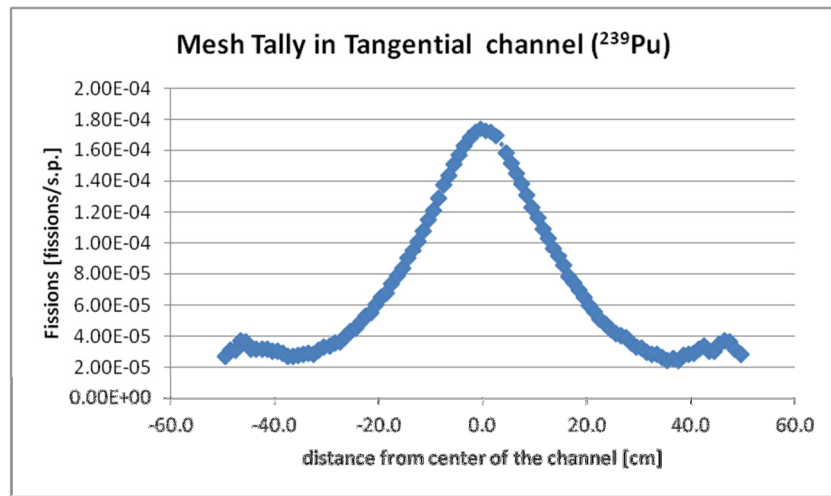
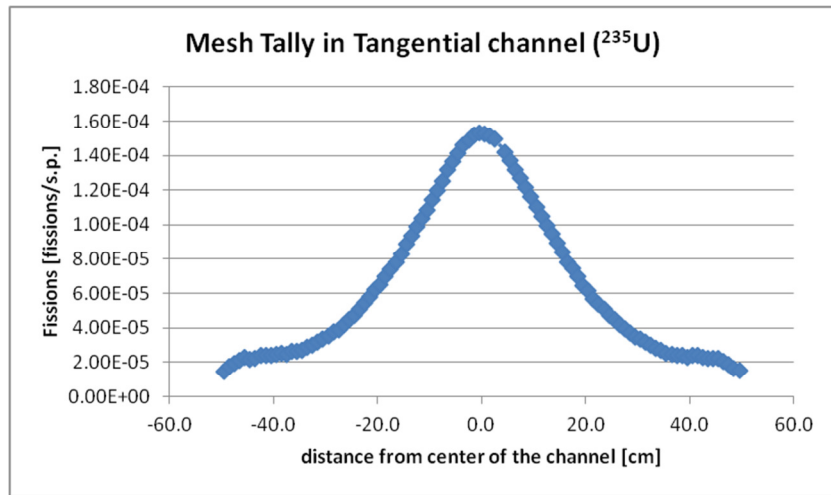


Figure 25 Fission rate on mesh tally for  $^{237}\text{Np}$  (a),  $^{238}\text{U}$  (b),  $^{239}\text{Pu}$  (c) and  $^{235}\text{U}$  (d) in the tangential channel of TAPIRO (JEFF31 data set, no pellet, Mesh voxel  $1 \times 1 \times 1 \text{ cm}^3$ ).



a)



b)

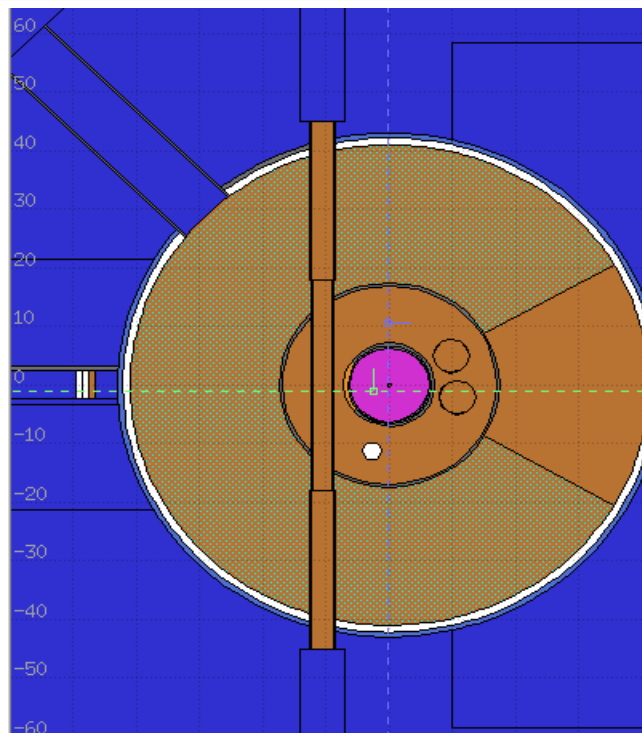


Figure 26 Fission rate on mesh tally for <sup>239</sup>Pu (a) and <sup>235</sup>U (b) in the tangential channel of TAPIRO (JEFF31 data set, no pellet, Mesh voxel 1x1x1 cm<sup>3</sup>).

In all channels  $^{237}\text{Np}$ ,  $^{235}\text{U}$  and  $^{239}\text{Pu}$  fissions rate have standard deviation contained in the range of 0.1% -8% of the estimated mean. Conversely,  $^{238}\text{U}$  fission rate shows a standard deviation range of 1%-30% of the estimated mean. Obviously, the highest dispersion for  $^{238}\text{U}$  fissions rate are located in the last few points at the extremities of the traverses. Due to their great affinity for fast fissions the  $^{237}\text{Np}$  and  $^{238}\text{U}$  show fission rate decrease with the increase of the distance from the core axis. Obviously,  $^{238}\text{U}$  that is practically insensitive to non-fast neutrons, shows a narrow curve than  $^{237}\text{Np}$ . In the case of  $^{235}\text{U}$  and  $^{239}\text{Pu}$ , the decrease of fission rate with distance is compensated by thermal and epithermal neutrons fissions (originated from the slowing down in the reflector) yielding in a broader decreasing curve. In distance range of 40-50 cm (end of the reflector, begin of the concrete biological shield) there are also relative maximum originated by the fission induced by the collided flux. All the results are compatible with previously estimated neutron fluxes (see page 25).

## The detector tally (F5) fission rate responses

In order to verify the internal coherency of the simulations the estimations of the fission rates for  $^{239}\text{Pu}$ ,  $^{235}\text{U}$ ,  $^{237}\text{Np}$  and  $^{238}\text{U}$  along the axis of the Diametrical, Radial 1 and Tangential channels have been re-estimated by using the F5 tally type placed in selected points . Table 18 resumes the performed simulation.

**Table 18 Simulation plan for the F5 detector tally estimations of fission rate in Radial, Diametrical and Tangential channels**

Simulations	Description
<b>DetectorTang</b>	Detector Tallies for $^{239}\text{Pu}$ , $^{237}\text{Np}$ , $^{238}\text{U}$ and $^{235}\text{U}$ in tangential channel. 11 estimations points from -50 to +50 cm along axis channel. Channel axis is parallel to the X axis of the reference system. No pellets in Diametrical channel. JEFF31 cross section dataset. 4000 iterations for KCODE.
<b>DetectorDiam</b>	Detector Tallies for $^{239}\text{Pu}$ , $^{237}\text{Np}$ , $^{238}\text{U}$ and $^{235}\text{U}$ in Diametrical channel. 11 estimation points from -55 to +55 cm along axis channel. Channel axis is coincident with the Y axis of the reference system. No pellets in Diametrical channel. JEFF31 cross section dataset. 4000 iterations for KCODE.
<b>DetectorRad</b>	Detector Tallies for $^{239}\text{Pu}$ , $^{237}\text{Np}$ , $^{238}\text{U}$ and $^{235}\text{U}$ in Diametrical channel. 6 estimation points from 9 cm to +55 cm along axis channel. Channel axis is coincident with the X axis of the reference system. No pellets in Diametrical channel. JEFF31 cross section dataset. 4000 iterations for KCODE.

Table 19 to Table 21 report the energy subdivision of the fission rates responses obtained in the simulation set: the “spectral” responses of the reaction rate are compatible with the cross section data (see Figure 19 and Figure 20) and the previously reported neutron spectra (Figure 11 to Figure 16).

Figure 27 to Figure 38 report the comparison of the mesh tally and detectors estimations that practically show coincident numerical response. In the light of these results, the internal coherency of the model appears to be adequate also for the fission rate estimations.

*Diametrical channel*

Table 19 Five energy bins representation of fission rates for <sup>239</sup>Pu, <sup>235</sup>U, <sup>238</sup>U and <sup>237</sup>Np detector tallies in Diametrical channel (Total flux estimations).

Distance [cm]	Upper Energy Bins [MeV]	U235		U238		Pu239		Np237	
		Fissions/s.p.	E%	Fissions/s.p.	E%	Fissions/s.p.	E%	Fissions/s.p.	E%
-55	[MeV]	5.83E-07	40.51%	Fissions/s.p.	E%	Fissions/s.p.	E%	Fissions/s.p.	E%
	1.00E-07	6.42E-06	5.16%	2.84E-14	40.36%	9.14E-07	40.33%	2.18E-11	40.52%
	5.00E-03	2.56E-07	8.11%	1.78E-11	12.89%	1.83E-05	30.84%	2.15E-08	13.83%
	1.00E+00	2.17E-09	7.37%	3.24E-11	8.49%	2.09E-07	6.28%	1.31E-08	8.28%
	2.00E+01	7.26E-06	5.78%	4.01E-10	7.39%	3.43E-09	7.37%	3.05E-09	7.32%
	Total	Fissions/s.p.	E%	4.51E-10	6.62%	1.94E-05	29.13%	3.77E-08	8.43%
-45	[MeV]	4.87E-07	15.77%	Fissions/s.p.	E%	Fissions/s.p.	E%	Fissions/s.p.	E%
	1.00E-07	2.05E-05	2.82%	2.39E-14	16.21%	7.73E-07	17.15%	1.82E-11	15.77%
	5.00E-03	2.46E-06	2.42%	1.52E-10	14.24%	3.28E-05	5.46%	7.24E-08	5.84%
	1.00E+00	1.57E-08	9.07%	3.28E-10	3.62%	2.10E-06	2.24%	1.05E-07	3.69%
	2.00E+01	2.35E-05	2.50%	2.50E-09	12.10%	2.47E-08	9.04%	2.19E-08	9.01%
	Total	Fissions/s.p.	E%	2.98E-09	10.19%	3.57E-05	5.04%	1.99E-07	3.05%
-35	[MeV]	6.64E-09	40.02%	Fissions/s.p.	E%	Fissions/s.p.	E%	Fissions/s.p.	E%
	1.00E-07	1.53E-05	2.56%	3.45E-16	40.21%	1.20E-08	40.48%	2.48E-13	40.02%
	5.00E-03	1.32E-05	1.12%	3.14E-10	28.63%	1.92E-05	7.81%	6.74E-08	3.75%
	1.00E+00	1.00E-07	3.55%	2.22E-09	2.67%	1.19E-05	1.07%	7.45E-07	3.47%
	2.00E+01	2.85E-05	1.47%	1.56E-08	5.53%	1.58E-07	3.57%	1.41E-07	3.60%
	Total	Fissions/s.p.	E%	1.82E-08	4.80%	3.13E-05	4.81%	9.53E-07	2.78%
-25	[MeV]	1.07E-11	80.21%	Fissions/s.p.	E%	Fissions/s.p.	E%	Fissions/s.p.	E%
	1.00E-07	1.76E-05	5.59%	5.62E-19	81.11%	1.99E-11	82.72%	4.01E-16	80.19%
	5.00E-03	3.64E-05	0.62%	2.97E-10	9.19%	1.56E-05	4.43%	8.52E-08	3.35%
	1.00E+00	7.81E-07	1.76%	1.01E-08	1.58%	3.55E-05	0.61%	3.29E-06	1.46%
	2.00E+01	5.48E-05	1.85%	1.46E-07	1.84%	1.23E-06	1.75%	1.10E-06	1.72%
	Total	Fissions/s.p.	E%	1.57E-07	1.72%	5.23E-05	1.39%	4.48E-06	1.16%
-15	[MeV]	5.04E-18	83.11%	Fissions/s.p.	E%	Fissions/s.p.	E%	Fissions/s.p.	E%
	1.00E-07	1.89E-05	2.57%	2.66E-25	83.60%	9.57E-18	84.55%	1.88E-22	83.10%
	5.00E-03	8.74E-05	0.39%	3.99E-10	14.21%	1.59E-05	2.88%	9.91E-08	2.78%
	1.00E+00	6.64E-06	0.86%	4.84E-08	1.06%	9.37E-05	0.36%	1.43E-05	0.61%
	2.00E+01	1.13E-04	0.53%	1.55E-06	0.90%	1.05E-05	0.86%	9.41E-06	0.85%
	Total	Fissions/s.p.	E%	1.60E-06	0.87%	1.20E-04	0.48%	2.38E-05	0.51%
0	[MeV]	3.64E-27	47.51%	Fissions/s.p.	E%	Fissions/s.p.	E%	Fissions/s.p.	E%
	1.00E-07	7.19E-07	1.65%	1.80E-34	47.13%	5.78E-27	46.36%	1.36E-31	47.50%
	5.00E-03	2.51E-04	0.04%	1.08E-11	15.28%	5.67E-07	2.01%	5.63E-09	4.07%
	1.00E+00	1.80E-04	0.07%	3.91E-07	0.10%	3.22E-04	0.04%	9.69E-05	0.06%
	2.00E+01	4.32E-04	0.04%	6.02E-05	0.09%	2.86E-04	0.07%	2.60E-04	0.07%
	Total	Fissions/s.p.	E%	6.05E-05	0.09%	6.08E-04	0.04%	3.57E-04	0.05%
15	[MeV]	2.57E-17	99.75%	Fissions/s.p.	E%	Fissions/s.p.	E%	Fissions/s.p.	E%
	1.00E-07	1.99E-05	6.63%	1.35E-24	99.76%	4.84E-17	99.78%	9.58E-22	99.75%
	5.00E-03	8.95E-05	0.39%	3.77E-10	8.42%	1.56E-05	2.43%	1.05E-07	3.41%
	1.00E+00	6.78E-06	0.77%	4.92E-08	1.02%	9.59E-05	0.38%	1.46E-05	0.63%
	2.00E+01	1.16E-04	1.18%	1.60E-06	1.04%	1.07E-05	0.77%	9.61E-06	0.77%
	Total	Fissions/s.p.	E%	1.64E-06	1.01%	1.22E-04	0.43%	2.43E-05	0.49%
25	[MeV]	5.34E-13	94.08%	Fissions/s.p.	E%	Fissions/s.p.	E%	Fissions/s.p.	E%
	1.00E-07	1.66E-05	3.01%	2.80E-20	94.25%	9.95E-13	94.56%	1.99E-17	94.08%
	5.00E-03	3.68E-05	0.62%	2.72E-10	6.49%	1.51E-05	3.51%	9.38E-08	9.82%
	1.00E+00	7.88E-07	1.87%	1.08E-08	3.85%	3.58E-05	0.59%	3.34E-06	1.51%
	2.00E+01	5.42E-05	1.01%	1.51E-07	2.61%	1.24E-06	1.87%	1.11E-06	1.88%
	Total	Fissions/s.p.	E%	1.62E-07	2.45%	5.21E-05	1.10%	4.54E-06	1.22%
35	[MeV]	6.65E-09	41.53%	Fissions/s.p.	E%	Fissions/s.p.	E%	Fissions/s.p.	E%
	1.00E-07	1.55E-05	2.99%	3.39E-16	41.65%	1.13E-08	41.69%	2.48E-13	41.53%
	5.00E-03	1.28E-05	0.96%	1.67E-10	7.03%	1.66E-05	5.62%	6.68E-08	4.94%
	1.00E+00	1.08E-07	6.48%	2.05E-09	1.51%	1.15E-05	0.90%	6.89E-07	1.17%
	2.00E+01	2.84E-05	1.69%	1.86E-08	15.54%	1.70E-07	6.61%	1.51E-07	6.79%
	Total	Fissions/s.p.	E%	2.08E-08	13.88%	2.83E-05	3.31%	9.08E-07	1.49%
45	[MeV]	4.85E-07	15.64%	Fissions/s.p.	E%	Fissions/s.p.	E%	Fissions/s.p.	E%
	1.00E-07	2.20E-05	3.88%	2.34E-14	15.54%	7.39E-07	15.48%	1.82E-11	15.64%

	5.00E-03	2.47E-06	2.51%	1.14E-10	6.17%	4.07E-05	9.61%	6.57E-08	6.68%
	1.00E+00	1.45E-08	6.57%	3.60E-10	8.41%	2.09E-06	2.19%	1.06E-07	4.66%
	2.00E+01	2.50E-05	3.45%	2.18E-09	7.46%	2.29E-08	6.55%	2.03E-08	6.47%
	Total	Fissions/s.p.	E%	2.65E-09	6.24%	4.36E-05	8.99%	1.92E-07	3.52%
55	[MeV]	1.75E-07	16.34%	Fissions/s.p.	E%	Fissions/s.p.	E%	Fissions/s.p.	E%
	1.00E-07	6.33E-06	5.82%	8.45E-15	16.24%	2.66E-07	16.15%	6.54E-12	16.34%
	5.00E-03	2.27E-07	7.13%	4.02E-11	30.86%	1.16E-05	8.63%	1.39E-08	5.92%
	1.00E+00	2.61E-09	17.55%	2.99E-11	6.02%	1.89E-07	5.33%	1.10E-08	4.40%
	2.00E+01	6.73E-06	5.50%	6.97E-10	29.54%	4.13E-09	17.62%	3.70E-09	17.84%
	Total	5.83E-07	40.51%	7.67E-10	26.89%	1.20E-05	8.32%	2.86E-08	4.08%

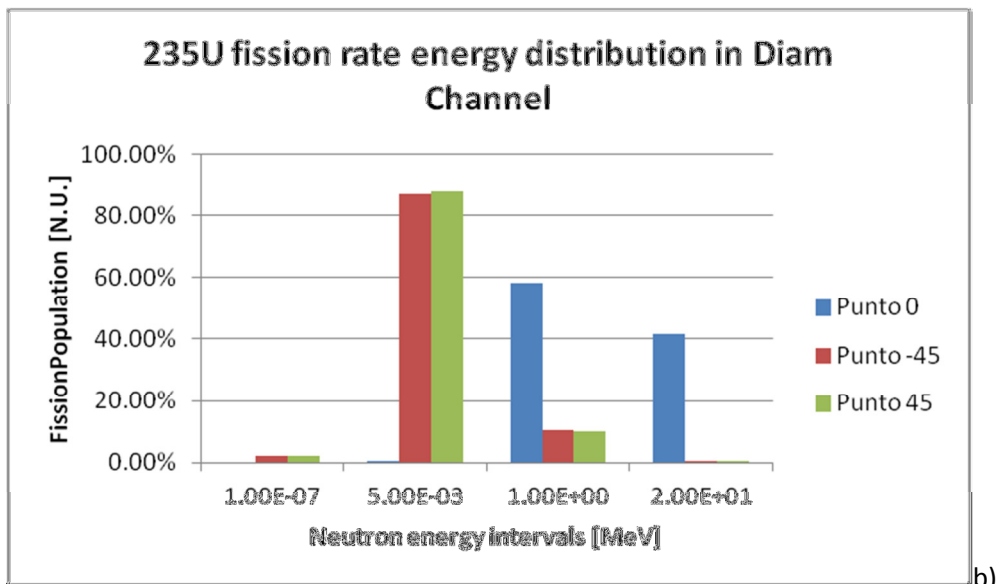
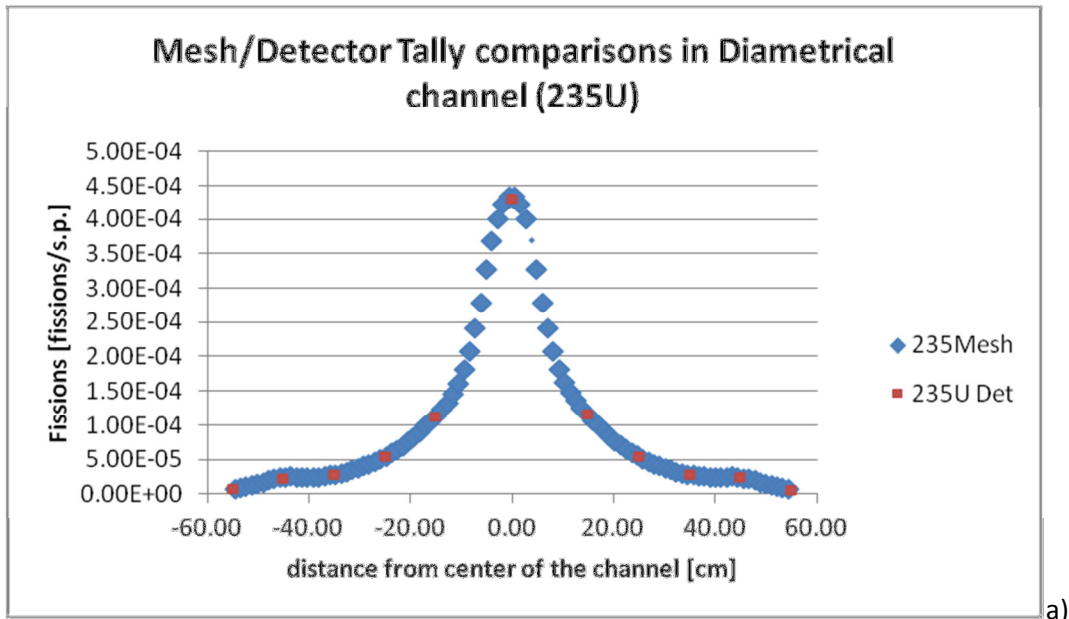


Figure 27 a) Comparison of mesh tally and detector tally responses for fission rate of  $^{235}\text{U}$  along the axis of the diametrical channel b) Four energy bins representation of the fission rate spectrum in three selected point detectors along the diametrical channel.



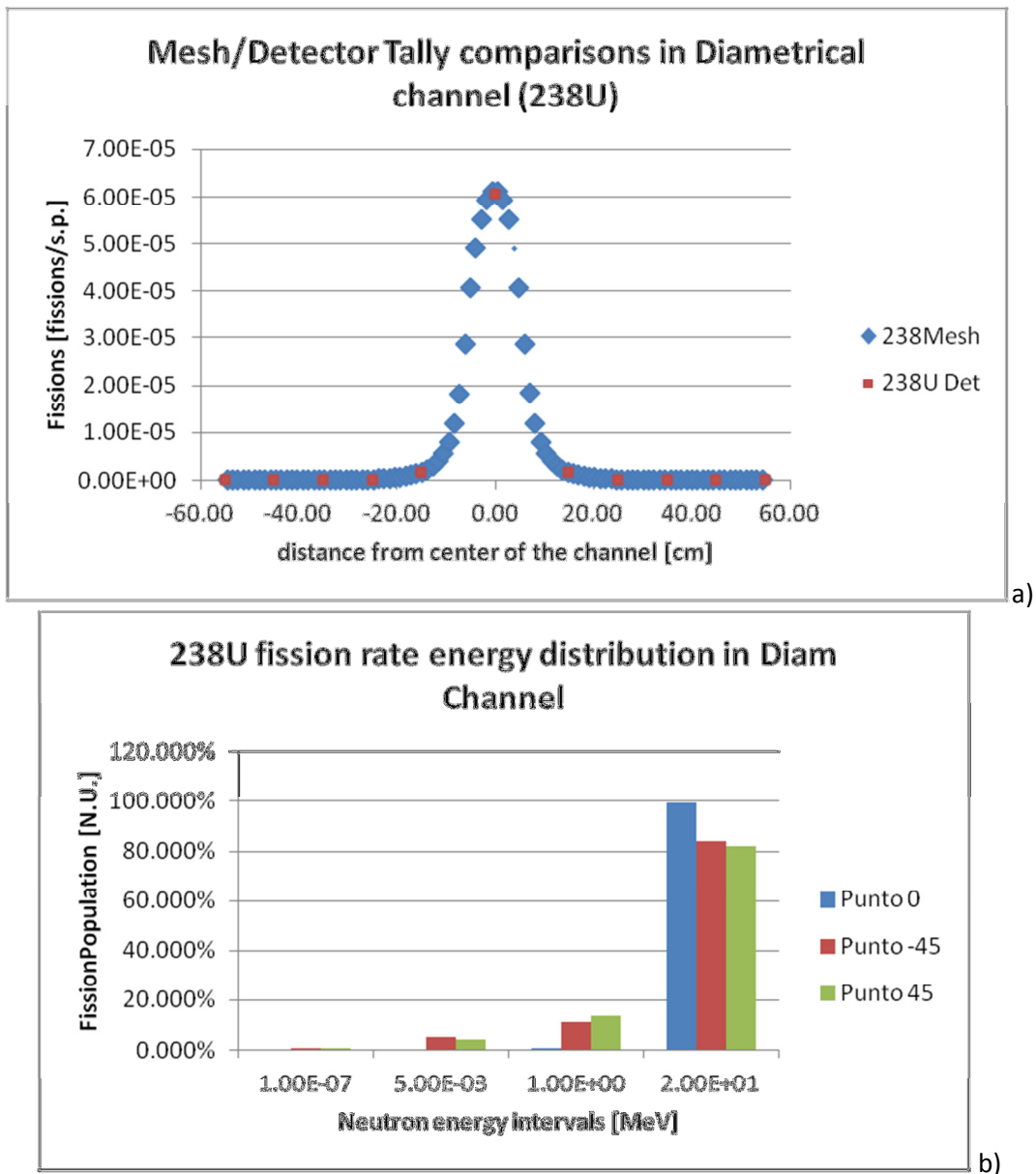
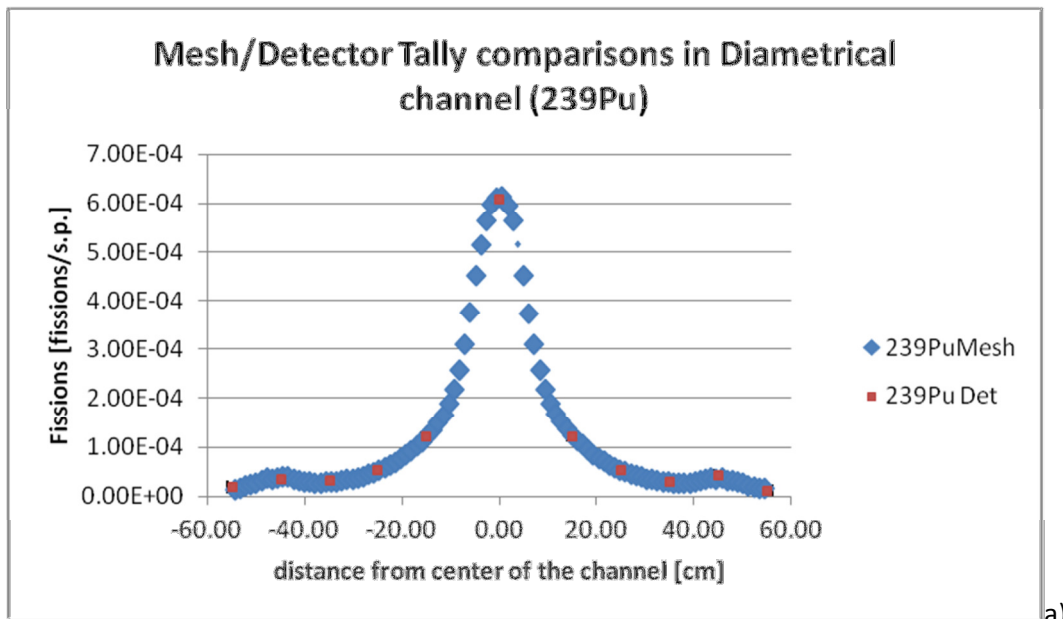
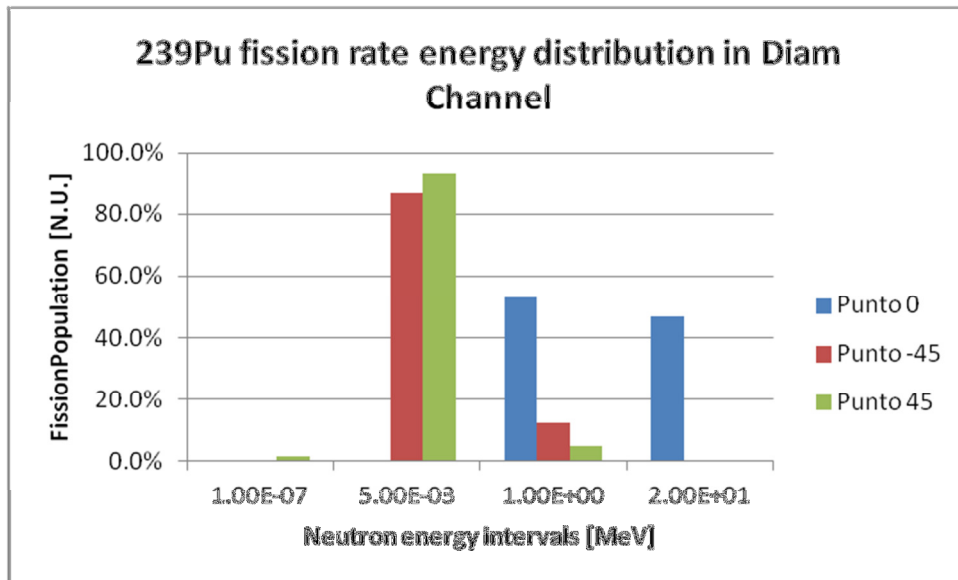


Figure 28 a) Comparison of mesh tally and detector tally responses for fission rate  $^{238}\text{U}$  along the axis of the diametrical channel. b) Four energy bins representation of the fission rate spectrum in three selected point detectors along the diametrical channel.



a)



b)

Figure 29 a) Comparison of mesh tally and detector tally responses for fission rate  $^{239}\text{Pu}$  along the axis of the diametrical channel. b) Four energy bins representation of the fission rate spectrum in three selected point detectors along the diametrical channel.

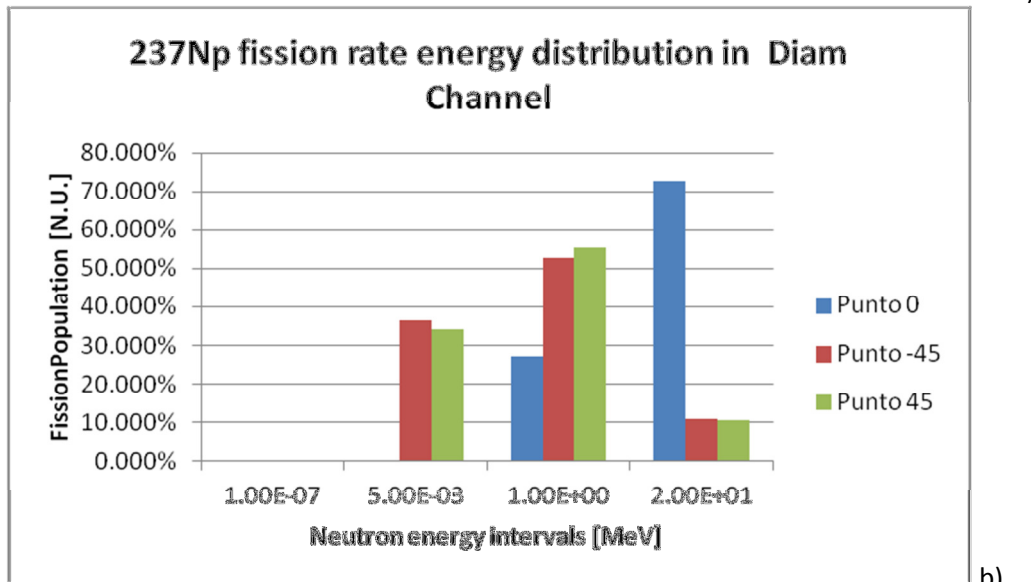
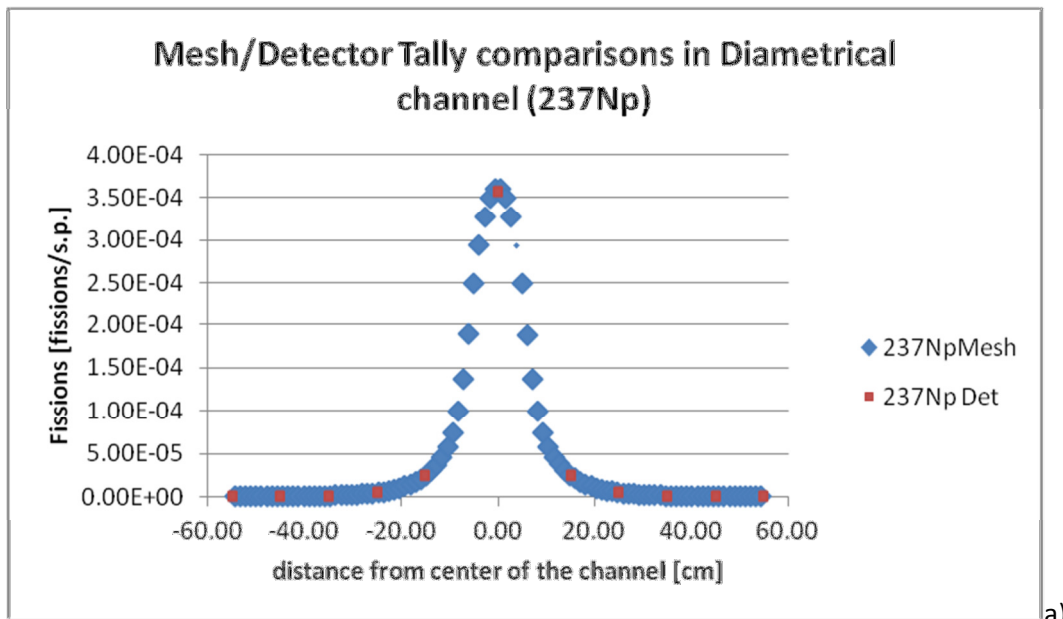


Figure 30 a) Comparison of mesh tally and detector tally responses for fission rate of  $^{237}\text{Np}$  along the axis of the diametrical channel. b) Four energy bins representation of the fission rate spectrum in three selected point detectors along the diametrical channel.

Radial channel

Table 20 Five energy bins representation of fission rates for <sup>239</sup>Pu, <sup>235</sup>U, <sup>238</sup>U and <sup>237</sup>Np detector tallies in Radial 1 channel (Total flux estimations).

Distance [cm]	Upper Energy Bins [MeV]	U235		U238		Pu239		Np237	
		Fissions/s.p.	E%	Fissions/s.p.	E%	Fissions/s.p.	E%	Fissions/s.p.	E%
9	1.00E-07	2.83E-10	50.47%	1.40E-17	50.32%	4.45E-10	50.16%	1.06E-14	50.47%
	5.00E-03	1.81E-05	3.45%	3.03E-10	4.86%	1.71E-05	9.10%	9.79E-08	3.38%
	1.00E+00	1.47E-04	0.21%	1.39E-07	0.31%	1.71E-04	0.20%	3.77E-05	0.29%
	2.00E+01	3.64E-05	0.71%	1.07E-05	1.10%	5.77E-05	0.73%	5.21E-05	0.74%
	Total	2.02E-04	0.37%	1.08E-05	1.09%	2.46E-04	0.67%	8.99E-05	0.45%
15	1.00E-07	2.42E-09	79.19%	1.23E-16	80.63%	4.17E-09	82.30%	9.04E-14	79.14%
	5.00E-03	2.23E-05	0.53%	4.00E-10	2.58%	1.99E-05	1.16%	1.15E-07	0.74%
	1.00E+00	8.79E-05	0.07%	5.27E-08	0.14%	9.50E-05	0.06%	1.54E-05	0.10%
	2.00E+01	9.16E-06	0.11%	2.41E-06	0.14%	1.45E-05	0.11%	1.31E-05	0.11%
	Total	1.19E-04	0.11%	2.46E-06	0.14%	1.29E-04	0.19%	2.85E-05	0.08%
25	1.00E-07	1.25E-09	27.57%	6.19E-17	28.18%	2.00E-09	28.96%	4.69E-14	27.55%
	5.00E-03	2.16E-05	0.60%	3.59E-10	2.88%	2.06E-05	0.97%	1.04E-07	0.86%
	1.00E+00	3.66E-05	0.11%	1.17E-08	0.26%	3.60E-05	0.10%	3.69E-06	0.18%
	2.00E+01	1.38E-06	0.26%	3.35E-07	0.31%	2.19E-06	0.26%	1.97E-06	0.26%
	Total	5.96E-05	0.23%	3.47E-07	0.30%	5.88E-05	0.35%	5.76E-06	0.15%
35	1.00E-07	2.18E-08	32.05%	1.09E-15	31.91%	3.55E-08	31.56%	8.15E-13	32.03%
	5.00E-03	1.91E-05	0.73%	2.45E-10	3.87%	2.10E-05	1.65%	8.18E-08	1.34%
	1.00E+00	1.30E-05	0.18%	2.67E-09	0.49%	1.20E-05	0.18%	8.64E-07	0.35%
	2.00E+01	2.77E-07	0.50%	6.95E-08	0.54%	4.38E-07	0.50%	3.94E-07	0.50%
	Total	3.24E-05	0.44%	7.25E-08	0.52%	3.35E-05	1.04%	1.34E-06	0.29%
45	1.00E-07	4.79E-07	10.99%	2.32E-14	10.92%	7.35E-07	10.78%	1.79E-11	10.98%
	5.00E-03	2.02E-05	0.75%	1.45E-10	5.55%	3.09E-05	1.76%	6.94E-08	1.68%
	1.00E+00	2.69E-06	0.37%	5.16E-10	0.89%	2.37E-06	0.35%	1.59E-07	0.69%
	2.00E+01	7.94E-08	0.73%	2.30E-08	0.79%	1.26E-07	0.73%	1.14E-07	0.73%
	Total	2.35E-05	0.69%	2.36E-08	0.77%	3.41E-05	1.61%	3.42E-07	0.54%
55	1.00E-07	1.47E-07	18.68%	7.13E-15	18.73%	2.26E-07	18.87%	5.50E-12	18.68%
	5.00E-03	6.57E-06	6.24%	2.67E-11	22.02%	1.17E-05	13.15%	1.64E-08	7.41%
	1.00E+00	2.85E-07	4.50%	7.40E-11	7.76%	2.56E-07	4.18%	2.34E-08	8.12%
	2.00E+01	1.48E-08	5.75%	4.06E-09	7.02%	2.33E-08	5.64%	2.10E-08	5.62%
	Total	7.01E-06	5.87%	4.16E-09	6.86%	1.22E-05	12.62%	6.08E-08	4.22%

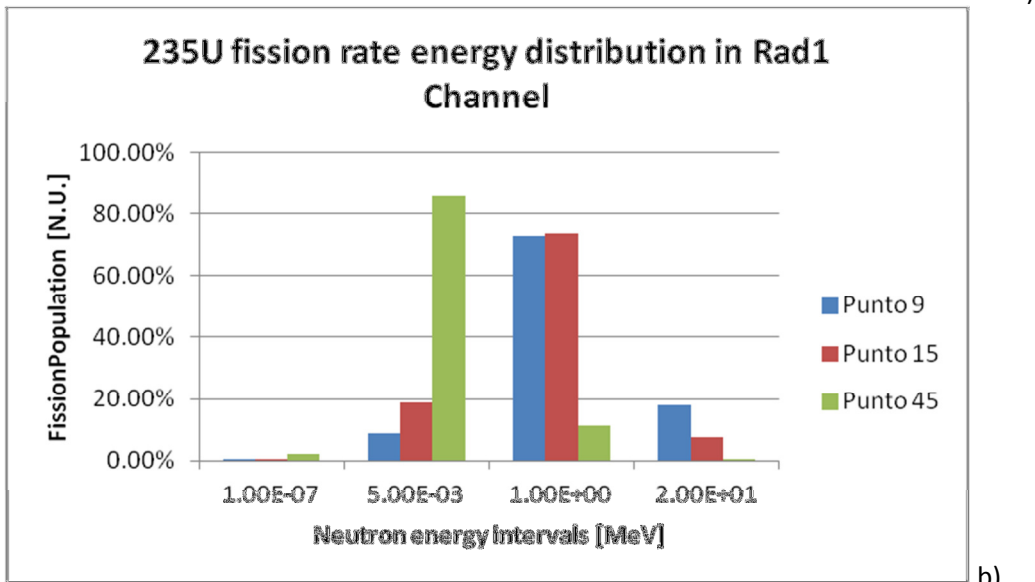
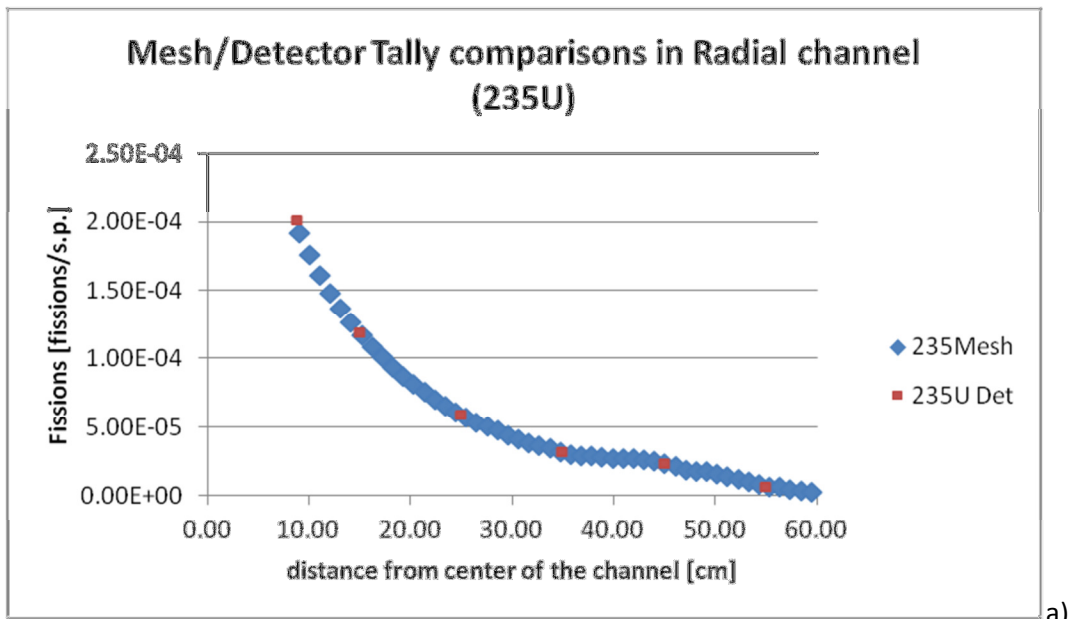


Figure 31 a) Comparison of mesh tally and detector tally responses for fission rate of <sup>235</sup>U along the axis of the Radial 1 channel. b) Four energy bins representation of the fission rate spectrum in three selected point detectors along the radial 1 channel.

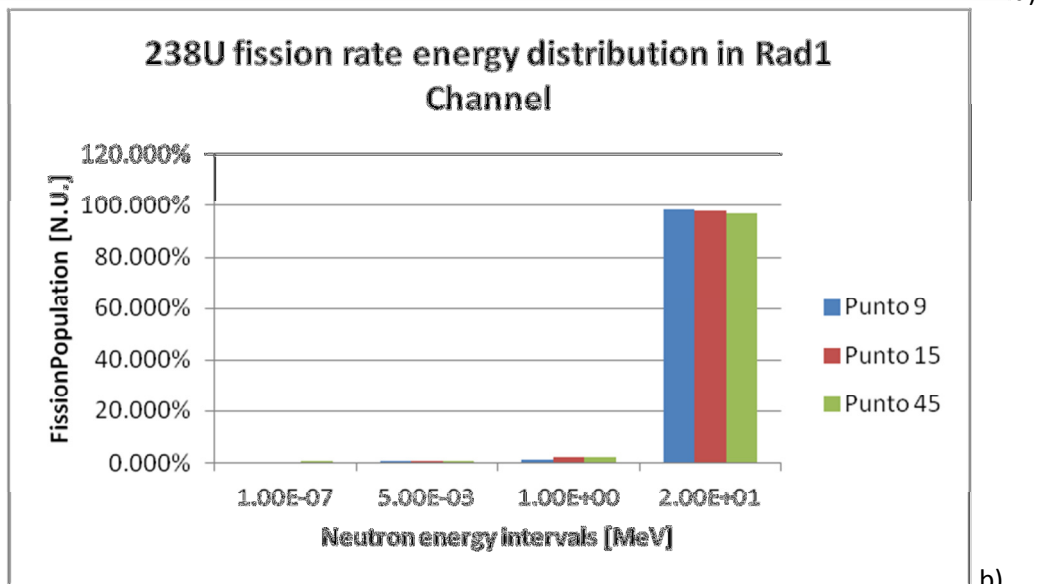
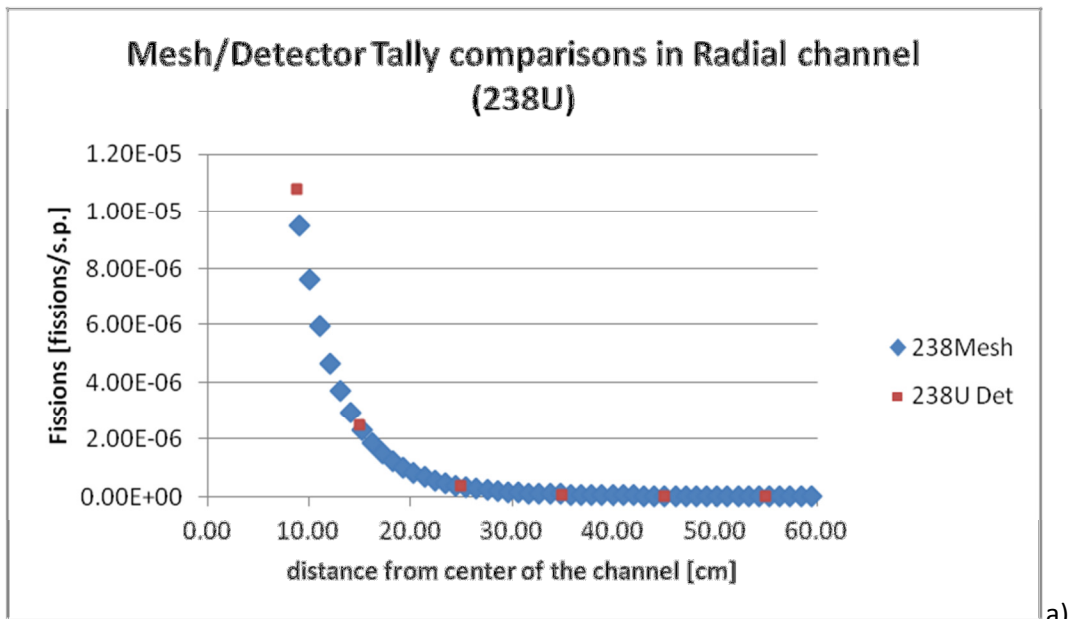


Figure 32 a) Comparison of mesh tally and detector tally responses for fission rate of  $^{238}\text{U}$  along the axis of the Radial 1 channel. b) Four energy bins representation of the fission rate spectrum in three selected point detectors along the radial 1 channel.

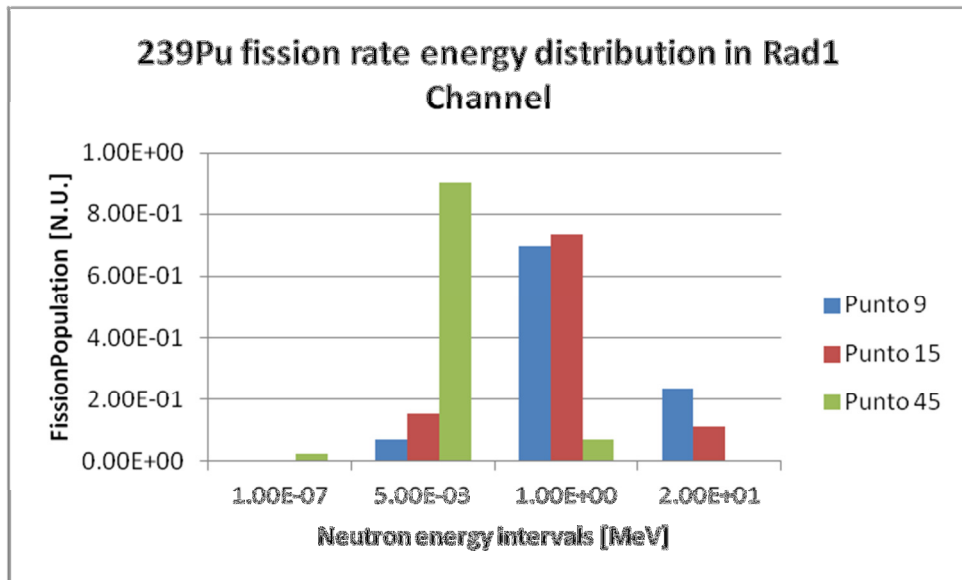
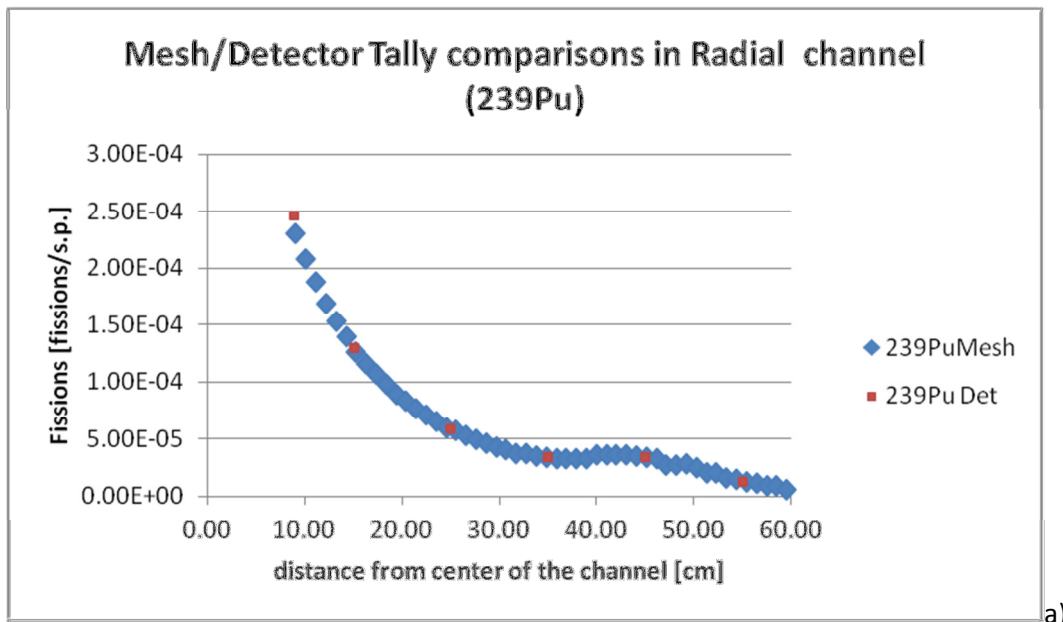


Figure 33 a) Comparison of mesh tally and detector tally responses for fission rate of  $^{239}\text{Pu}$  along the axis of the Radial 1 channel. b) Four energy bins representation of the fission rate spectrum in three selected point detectors along the radial 1 channel.

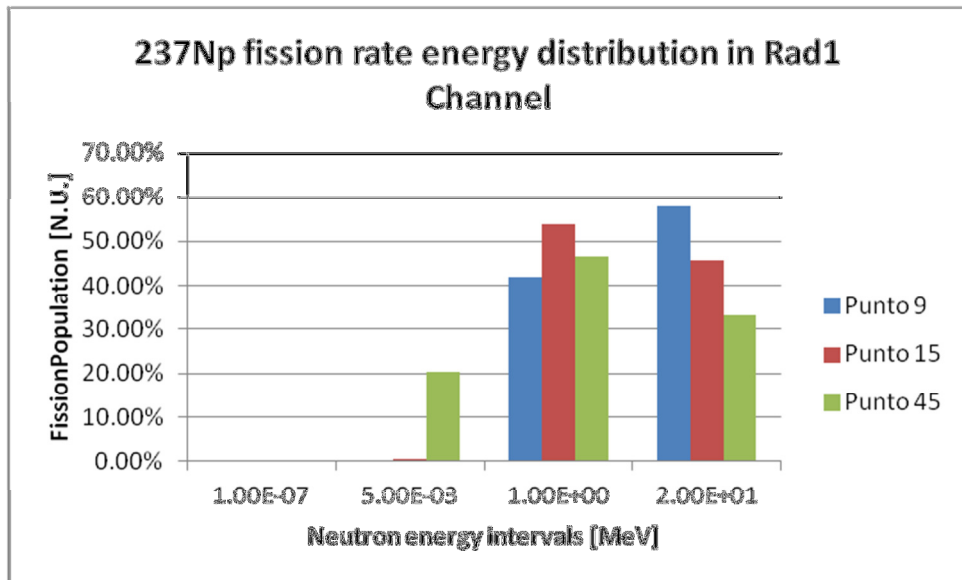
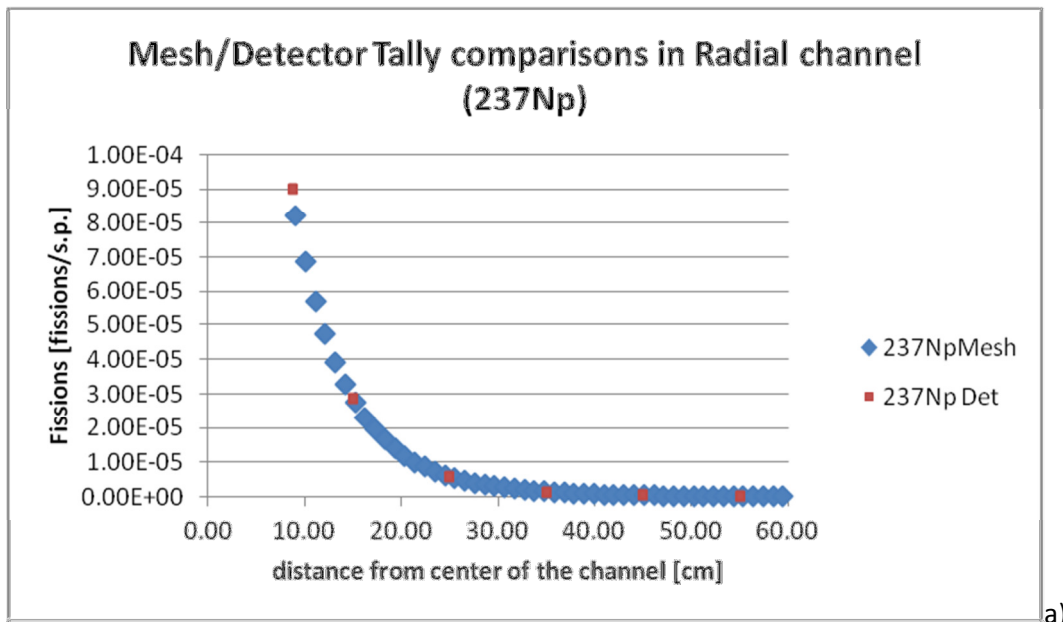


Figure 34 a) Comparison of mesh tally and detector tally responses for fission rate of <sup>237</sup>Np along the axis of the Radial 1 channel. b) Four energy bins representation of the fission rate spectrum in three selected point detectors along the radial 1 channel.



Tangential Channel

Table 21 Five energy bins representation of fission rates for <sup>239</sup>Pu, <sup>235</sup>U, <sup>238</sup>U and <sup>237</sup>Np detector tallies in Tangential channel (Total flux estimations).

Distance [cm]	Upper Energy Bins	U235		U238		Pu239		Np237	
	[MeV]	Fissions/s.p.	E%	Fissions/s.p.	E%	Fissions/s.p.	E%	Fissions/s.p.	E%
-50	1.00E-07	8.64E-07	20.29%	4.17E-14	20.28%	1.32E-06	20.52%	3.24E-11	E%
	5.00E-03	1.24E-05	6.04%	7.29E-11	26.86%	3.20E-05	32.04%	3.35E-08	20.30%
	1.00E+00	5.49E-07	5.44%	7.28E-11	10.13%	4.74E-07	5.96%	2.42E-08	6.60%
	2.00E+01	5.36E-09	9.40%	1.15E-09	10.69%	8.48E-09	9.40%	7.59E-09	5.85%
	Total	1.38E-05	5.63%	1.30E-09	9.63%	3.38E-05	30.35%	6.53E-08	9.42%
-40	1.00E-07	9.05E-08	17.64%	4.51E-15	18.05%	1.48E-07	18.60%	3.38E-12	E%
	5.00E-03	1.85E-05	4.86%	1.38E-10	9.49%	3.06E-05	16.16%	6.53E-08	17.63%
	1.00E+00	4.94E-06	1.40%	6.77E-10	4.26%	4.26E-06	1.63%	2.21E-07	5.81%
	2.00E+01	2.58E-08	3.67%	4.03E-09	5.60%	4.07E-08	3.68%	3.61E-08	4.60%
	Total	2.36E-05	3.84%	4.84E-09	4.70%	3.50E-05	14.11%	3.22E-07	3.69%
-30	1.00E-07	2.76E-10	48.22%	1.41E-17	48.67%	4.77E-10	49.29%	1.03E-14	E%
	5.00E-03	1.99E-05	16.28%	2.12E-10	6.92%	1.53E-05	3.26%	7.36E-08	48.22%
	1.00E+00	1.86E-05	0.90%	3.77E-09	6.83%	1.72E-05	0.99%	1.22E-06	5.08%
	2.00E+01	1.89E-07	3.21%	3.26E-08	6.72%	2.98E-07	3.23%	2.65E-07	3.52%
	Total	3.86E-05	8.39%	3.66E-08	6.03%	3.28E-05	1.61%	1.56E-06	3.28%
-20	1.00E-07	2.10E-11	76.59%	1.10E-18	77.32%	3.91E-11	78.55%	7.83E-16	E%
	5.00E-03	1.79E-05	1.95%	3.06E-10	5.61%	1.57E-05	2.81%	9.39E-08	76.59%
	1.00E+00	4.35E-05	0.56%	1.36E-08	1.30%	4.30E-05	0.55%	4.37E-06	2.92%
	2.00E+01	1.17E-06	1.50%	2.24E-07	1.29%	1.85E-06	1.50%	1.65E-06	1.01%
	Total	6.25E-05	0.68%	2.38E-07	1.22%	6.05E-05	0.83%	6.11E-06	1.49%
-10	1.00E-07	7.01E-19	33.27%	3.50E-26	33.75%	1.15E-18	34.57%	2.62E-23	E%
	5.00E-03	2.08E-05	2.03%	6.46E-10	45.49%	1.88E-05	5.05%	1.04E-07	33.26%
	1.00E+00	8.45E-05	0.41%	4.40E-08	1.13%	8.99E-05	0.39%	1.32E-05	2.10%
	2.00E+01	6.00E-06	1.05%	1.40E-06	1.65%	9.48E-06	1.05%	8.50E-06	0.58%
	Total	1.11E-04	0.49%	1.44E-06	1.60%	1.18E-04	0.86%	2.18E-05	1.05%
0	1.00E-07	1.54E-17	36.02%	7.57E-25	35.66%	2.41E-17	35.15%	5.75E-22	E%
	5.00E-03	2.04E-05	2.13%	4.28E-10	19.69%	1.86E-05	5.00%	1.05E-07	36.02%
	1.00E+00	1.16E-04	0.32%	8.52E-08	0.69%	1.30E-04	0.31%	2.42E-05	1.90%
	2.00E+01	1.57E-05	0.72%	4.06E-06	0.65%	2.49E-05	0.72%	2.24E-05	0.53%
	Total	1.53E-04	0.38%	4.14E-06	0.64%	1.74E-04	0.59%	4.67E-05	0.70%
10	1.00E-07	1.95E-18	52.38%	9.70E-26	52.47%	3.13E-18	52.54%	7.27E-23	E%
	5.00E-03	2.17E-05	2.06%	4.65E-10	21.36%	1.89E-05	2.90%	1.14E-07	52.38%
	1.00E+00	8.59E-05	0.41%	4.58E-08	1.40%	9.15E-05	0.39%	1.37E-05	2.89%
	2.00E+01	6.20E-06	0.80%	1.45E-06	0.93%	9.80E-06	0.80%	8.79E-06	0.77%
	Total	1.14E-04	0.50%	1.50E-06	0.90%	1.20E-04	0.55%	2.26E-05	0.79%
20	1.00E-07	1.35E-12	99.70%	7.15E-20	99.71%	2.56E-12	99.73%	5.05E-17	E%
	5.00E-03	1.91E-05	3.06%	3.43E-10	8.31%	1.62E-05	3.60%	9.02E-08	99.70%
	1.00E+00	4.29E-05	0.56%	1.31E-08	1.33%	4.22E-05	0.55%	4.23E-06	2.98%
	2.00E+01	1.15E-06	2.57%	2.20E-07	2.54%	1.82E-06	2.56%	1.62E-06	1.16%
	Total	6.32E-05	1.00%	2.33E-07	2.40%	6.02E-05	1.04%	5.94E-06	2.55%
30	1.00E-07	3.12E-10	51.45%	1.58E-17	51.30%	5.28E-10	50.80%	1.17E-14	E%
	5.00E-03	1.49E-05	2.14%	2.12E-10	6.65%	1.52E-05	4.26%	7.07E-08	51.45%
	1.00E+00	1.78E-05	0.92%	3.18E-09	1.59%	1.63E-05	0.91%	1.06E-06	3.89%
	2.00E+01	1.78E-07	3.20%	2.98E-08	3.92%	2.81E-07	3.19%	2.50E-07	1.40%
	Total	3.29E-05	1.09%	3.32E-08	3.52%	3.17E-05	2.09%	1.38E-06	3.19%
40	1.00E-07	2.07E-07	23.57%	9.97E-15	23.08%	3.12E-07	22.48%	7.76E-12	E%

	5.00E-03	1.80E-05	4.22%	1.48E-10	15.30%	2.39E-05	5.43%	6.23E-08	23.57%
	1.00E+00	4.89E-06	1.87%	5.68E-10	1.74%	4.16E-06	1.72%	1.94E-07	3.19%
	2.00E+01	2.72E-08	10.07%	3.53E-09	4.94%	4.29E-08	10.07%	3.78E-08	1.88%
	Total	2.32E-05	3.32%	4.24E-09	4.15%	2.85E-05	4.58%	2.94E-07	9.85%
50	[MeV]	Fissions/s.p.	E%	Fissions/s.p.	E%	Fissions/s.p.	E%	Fissions/s.p.	E%
	1.00E-07	6.15E-07	35.38%	2.83E-14	33.40%	8.56E-07	31.75%	2.31E-11	1.90%
	5.00E-03	1.13E-05	3.83%	4.05E-11	10.32%	2.63E-05	13.94%	3.75E-08	35.53%
	1.00E+00	5.20E-07	6.81%	5.72E-11	3.25%	4.34E-07	6.58%	2.21E-08	17.73%
	2.00E+01	3.85E-09	8.00%	8.52E-10	13.97%	6.09E-09	7.99%	5.45E-09	4.12%
	Total	1.24E-05	3.95%	9.50E-10	12.54%	2.76E-05	13.32%	6.51E-08	8.10%

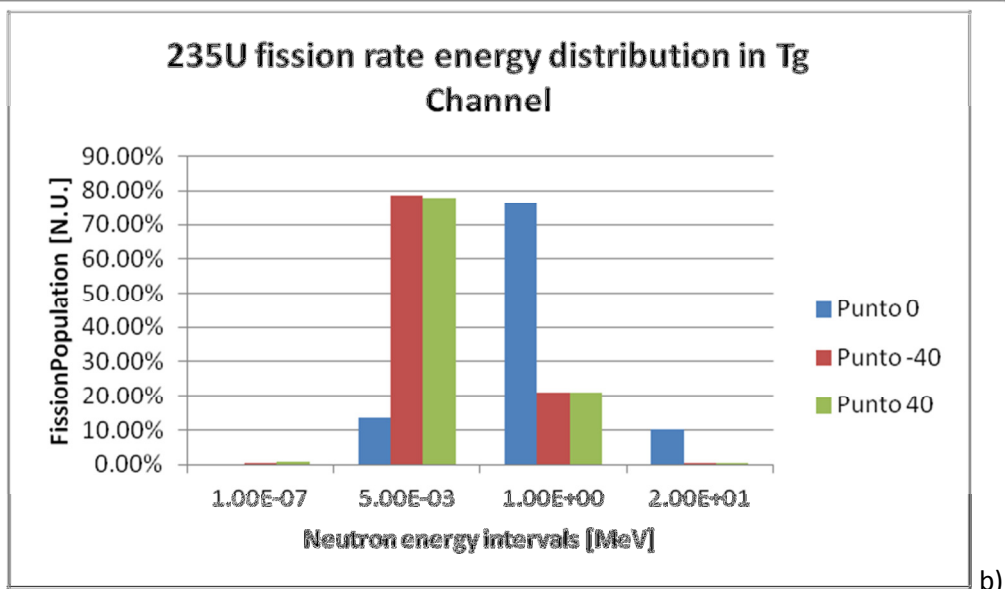
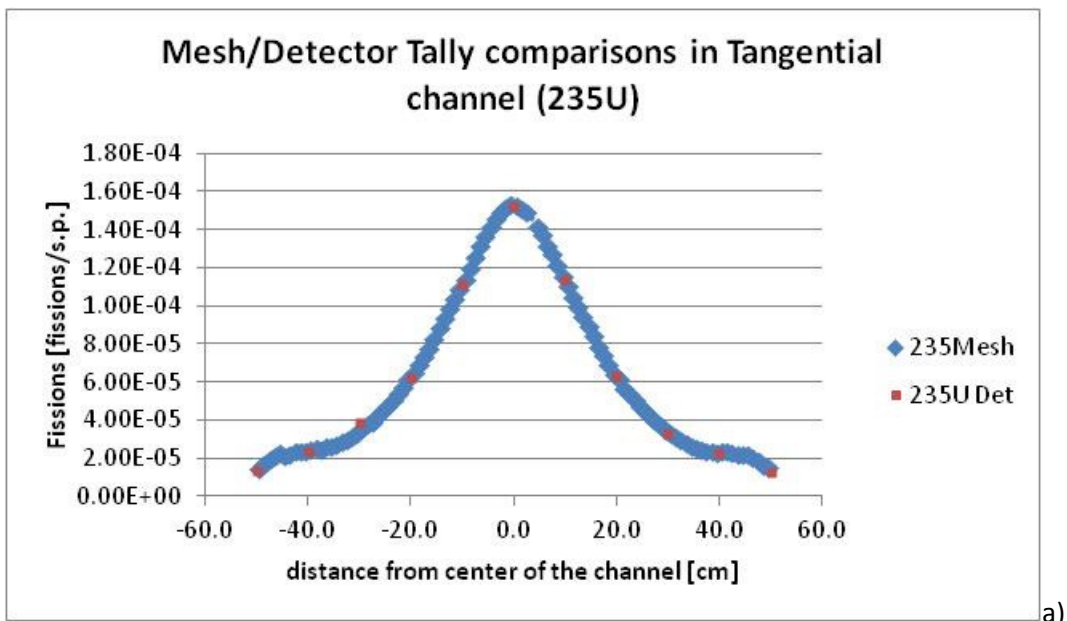
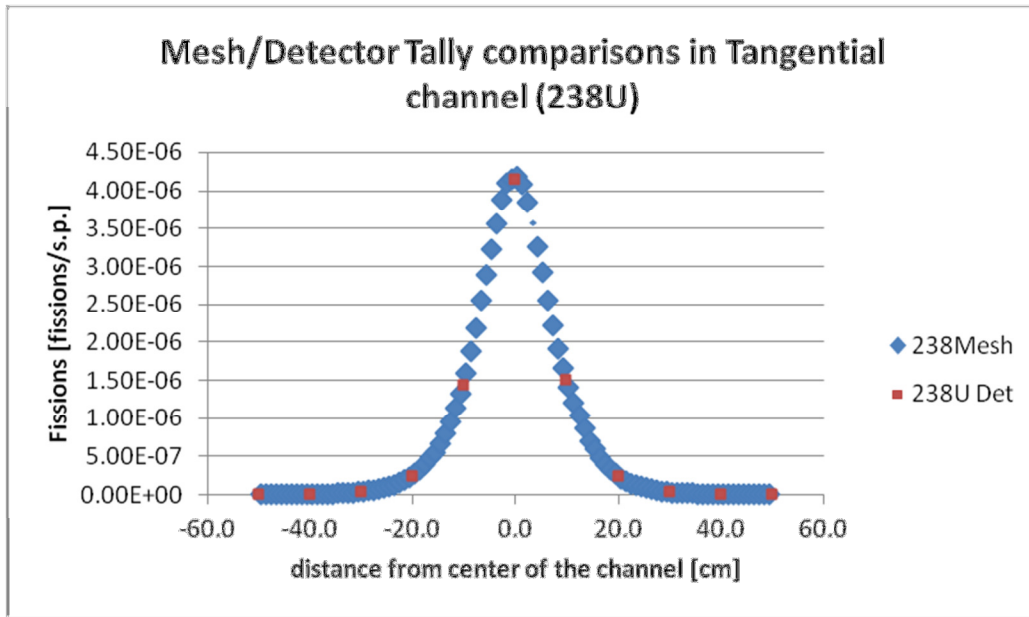
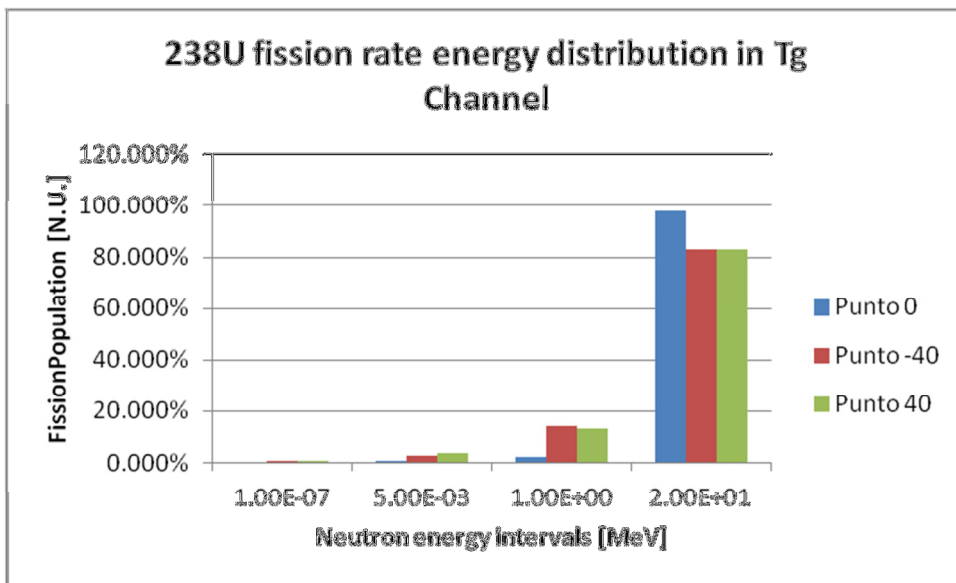


Figure 35 a) Comparison of mesh tally and detector tally responses for fission rate of <sup>235</sup>U along the axis of the Tangential channel. b) Four energy bins representation of the fission rate spectrum in three selected point detectors along the tangential channel.



a)



b)

Figure 36 a) Comparison of mesh tally and detector tally responses for fission rate of <sup>238</sup>U along the axis of the Tangential channel. b) Four energy bins representation of the fission rate spectrum in three selected point detectors along the tangential channel.

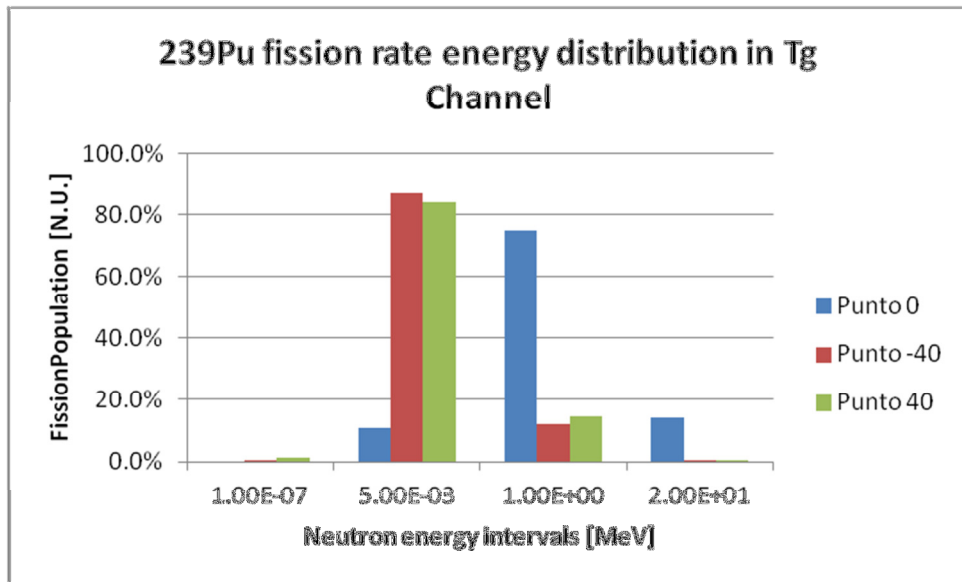
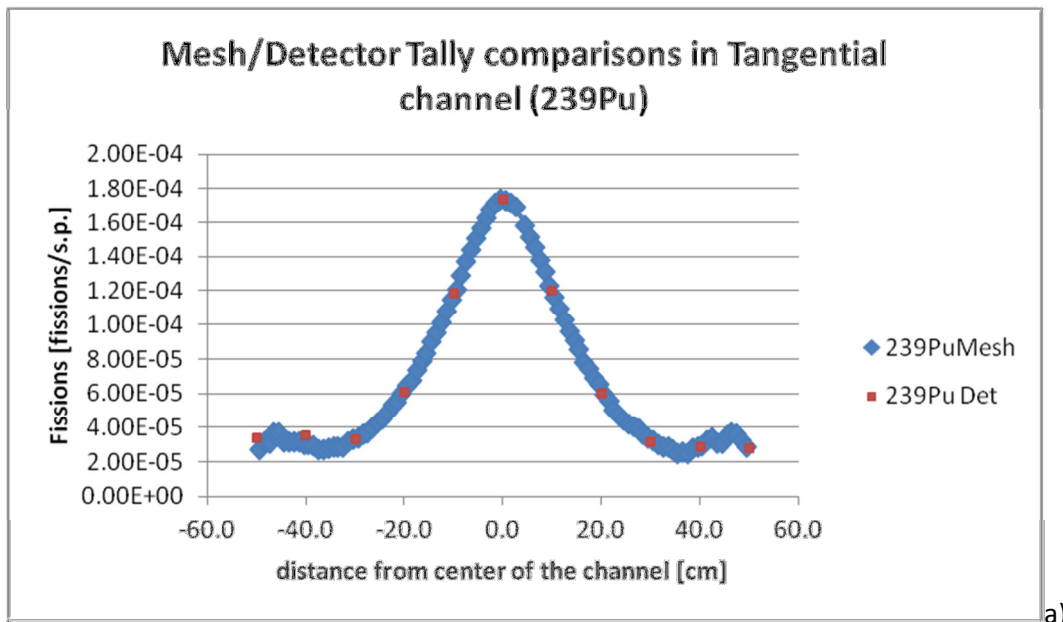


Figure 37 a) Comparison of mesh tally and detector tally responses for fission rate of <sup>239</sup>Pu along the axis of the tangential channel. b) Four energy bins representation of the fission rate spectrum in three selected point detectors along the tangential channel.

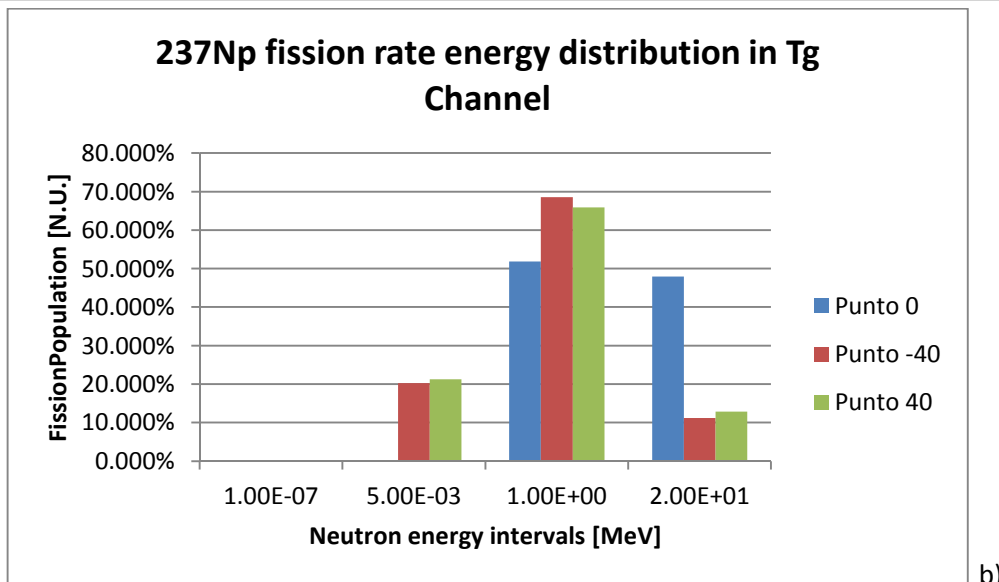
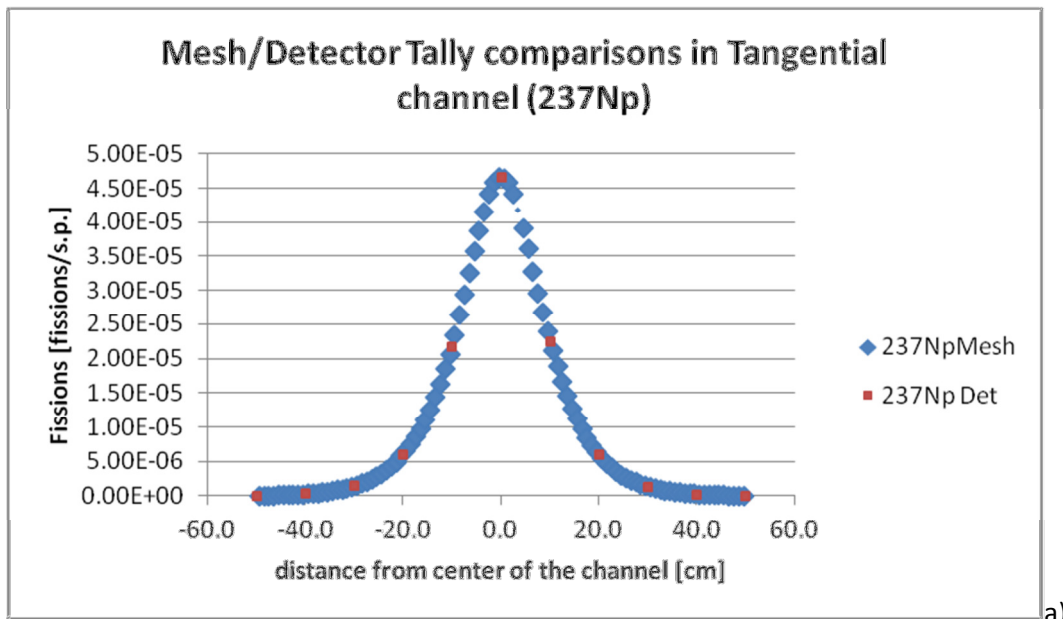


Figure 38 a) Comparison of mesh tally and detector tally responses for fission rate of  $^{237}\text{Np}$  along the axis of the tangential channel b) Four energy bins representation of the fission rate spectrum in three selected point detectors along the tangential channel.

## Reaction Rate Traverses

Accordingly, with reference [2], neutron induced reaction rates on  $^{45}\text{Sc}$ ,  $^{197}\text{Au}$ ,  $^{58}\text{Ni}$  and  $^{59}\text{Co}$  foils have been estimated along the same traverses in diametrical, radial1 and tangential channels. Table 22 reports properties of the metallic foils used in the simulations:  $^{59}\text{Co}$ ,  $^{197}\text{Au}$ ,  $^{45}\text{Sc}$  are mono-isotopic and the  $^{58}\text{Ni}$  has an isotopic abundance of 68%.

Table 22 Some nuclear properties of interest of the metallic foils

Foils	Reaction	Isotopic Abundance	Decay Modality of the product
<b>Metallic Cobalt</b>	$^{59}\text{Co}(n,\gamma)^{60}\text{Co}$	100%	$^{60\text{m}}\text{Co}$ , $t_{1/2}=10.47$ min. I.T. $^{60}\text{Co}$ , $t_{1/2}=5$ years, $\beta^-$
<b>Metallic Gold</b>	$^{197}\text{Au}(n,\gamma)^{198}\text{Au}$	100%	$^{198}\text{Au}$ ,
<b>Metallic Ni</b>	$^{58}\text{Ni}(n,p)^{58}\text{Co}$	68.08%	$^{58\text{m}}\text{Co}$ , $t_{1/2}=8.9$ hours, I.T. $^{58}\text{Co}$ , $t_{1/2}=70.85$ days, $\beta^+$ and E.C.
<b>Metallic Scandium</b>	$^{45}\text{Sc}(n,\gamma)^{46}\text{Sc}$	100%	$^{46\text{m}}\text{Sc}$ , $t_{1/2}=18.65$ s, I.T. $^{46}\text{Sc}$ , $t_{1/2}=83.78$ days, $\beta^-$

The irradiation of thin foils (from 20 to 100  $\mu\text{m}$  of thickness) allows an activation modality where transport phenomena in the foil volumes could be neglected and the reaction of interest is promoted by the incident neutron flux without spectral modification. In this condition is possible (as already done for fission rate) to compare the microscopic cross section of the four nuclides. Figure 39 reports the radiative capture microscopic cross section of  $^{59}\text{Co}$ . It is characterized by an almost  $1/v$  behavior (linear in the logarithmic scale of the figure) that breaks at the neutron energy of 20 eV in a broad peak whose maximum is located at about 200 eV (epithermal range) at the values of 900-1000 Barn. All the subsequent resonance peaks are below 10 barns (Energy range 1 keV-0.1MeV).

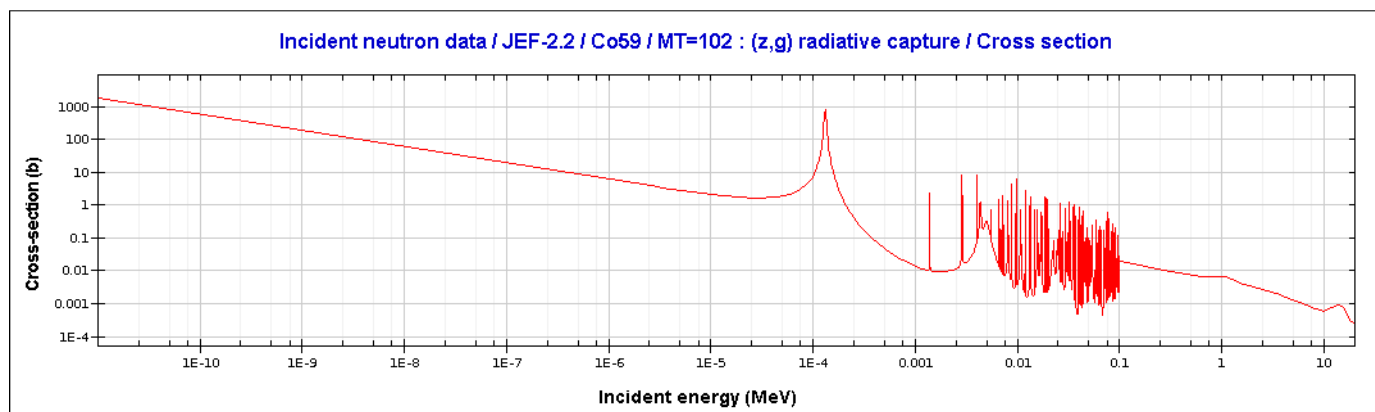


Figure 39 Microscopic cross section for the neutron radiative capture of  $^{59}\text{Co}$

Figure 40 reports the radiative capture for  $^{197}\text{Au}$ . In this case the  $1/v$  behavior breaks at 1 eV and a broad peak ( $> 10000$  Barn) is present at 6 eV. All the subsequent resonance peaks are in the range of 1000 – 80 Barn (Energy range 50 eV - 7 KeV).

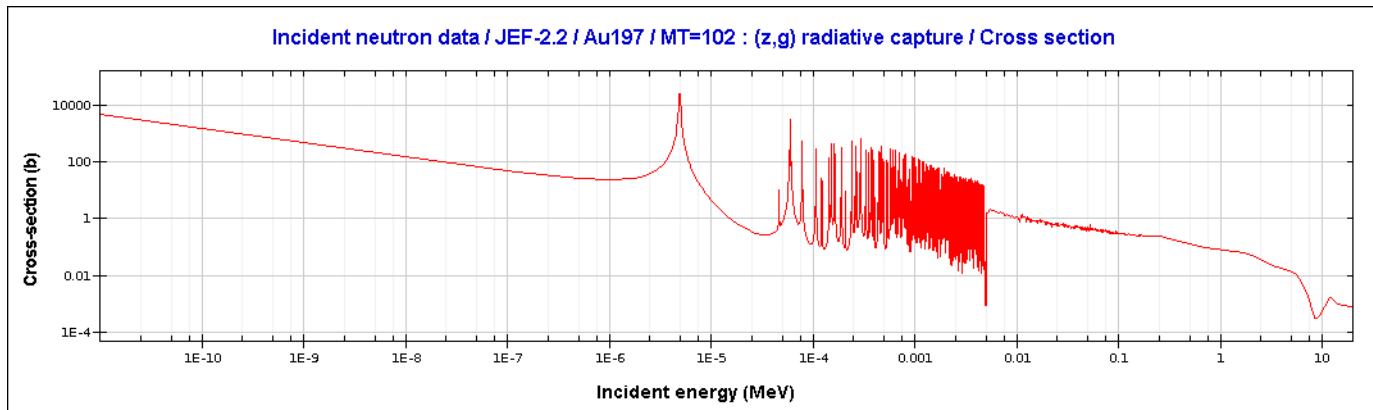


Figure 40 Microscopic cross section for the neutron radiative capture of  $^{197}\text{Au}$

In the case  $^{58}\text{Ni}$  (see Figure 41) the (n,p) reaction shows the typical behavior of a threshold reaction that is triggered at 1.5-2MeV of incident neutron energy.

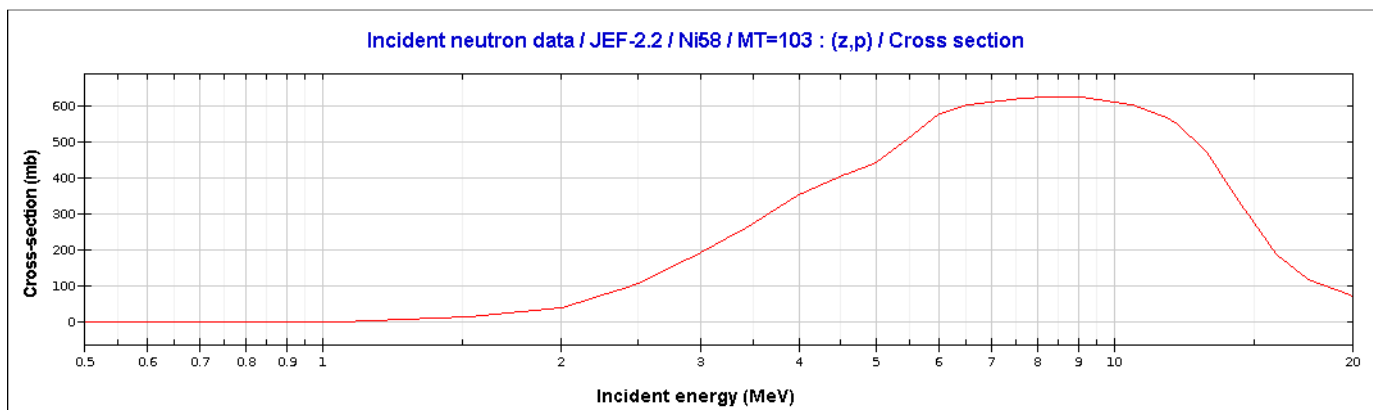


Figure 41 Microscopic cross section for the (n,p) reaction of  $^{58}\text{Ni}$ . it is evident the neutron energy threshold of 1.5-2 MeV

Finally, Figure 42 illustrated the behavior of  $^{45}\text{Sc}$  radiative capture cross section in function of the incident neutron energy. The cross section decrease monotonically up to epithermal energies and all resonances peak are well below 10 Barn (Energy range 1 keV-0.1MeV). In the fast energy range 0.1-2 MeV the cross section is higher than the one of the  $^{58}\text{Ni}$ .

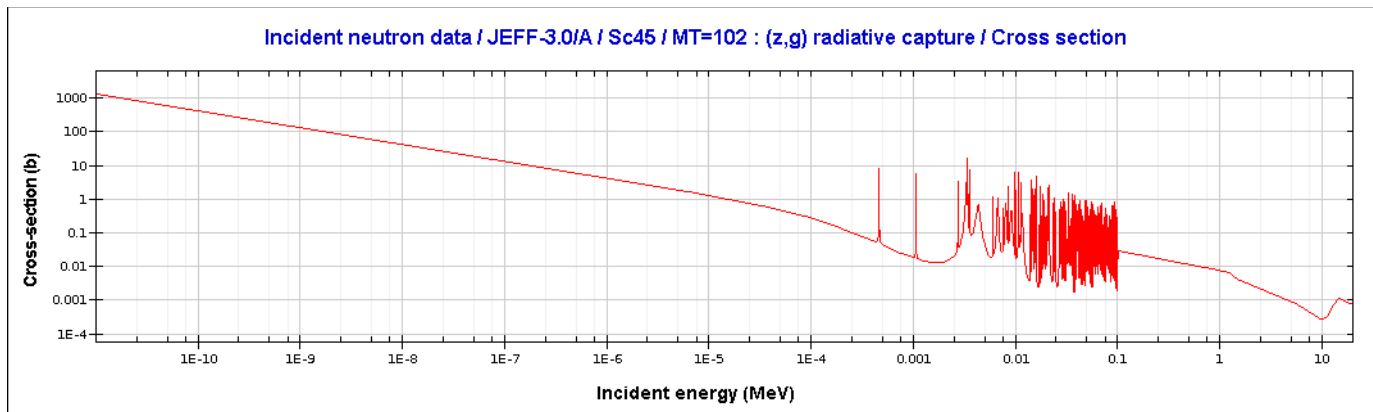


Figure 42 Microscopic cross section for the neutron radiative capture of <sup>45</sup>Sc

## MESH Tally reaction rate traverses

Table 23 reports the main features of the related simulation.

Table 23 Simulation plan for the Mesh Tally estimation of the Ni, Co, Au, Sc reaction rates

Simulations	Description
<b>ALLTgRdDiBigR</b>	<p>Mesh Tally for <sup>59</sup>Co, <sup>197</sup>Au, <sup>45</sup>Sc radiative capture and <sup>58</sup>Ni n,p reaction in tangential, radial and diametrical channels.                      Voxel dimensions are 1X1X1 cm<sup>3</sup>.                      Traverses range: from -55 to +55 cm in Diametrical channel, from -50 to +50 cm in Tangential channel, from 8.55 to 60 cm in Radial 1 channel.                      No pellets in Diametrical channel.                      JEFF31 cross section dataset.                      4000 iterations for KCODE.</p>

### Diametrical channel

The <sup>59</sup>Co(n,γ)<sup>60</sup>Co reaction rate, that is particularly sensible to epithermal neutrons (Figure 39), shows in the diametrical channels (accordingly with the neutron spectrum reported in Table 11) a minimum in the central position and a very noisy tendency to progressively increase the reaction rate as epithermal neutron components grows moving from core to periphery (see Figure 43).

Also in the case of <sup>197</sup>Au(n,γ)<sup>198</sup>Au reaction rate (see Figure 44), that shows an high capture cross section both for thermal range and epithermal range (Figure 40), the rate grows with the increase of the distance from core axis. The results are in agreement with the spectral properties of the channels (see again Table 11). The high uncertainty associated with the results should be a direct consequence of the weak intensity of the thermal and epithermal components of the spectrum joined with the shift of energy resonance region at lower energy compared to <sup>59</sup>Co. Both <sup>59</sup>Co and <sup>197</sup>Au responses retains an almost symmetric pattern between the two branch of the channel.



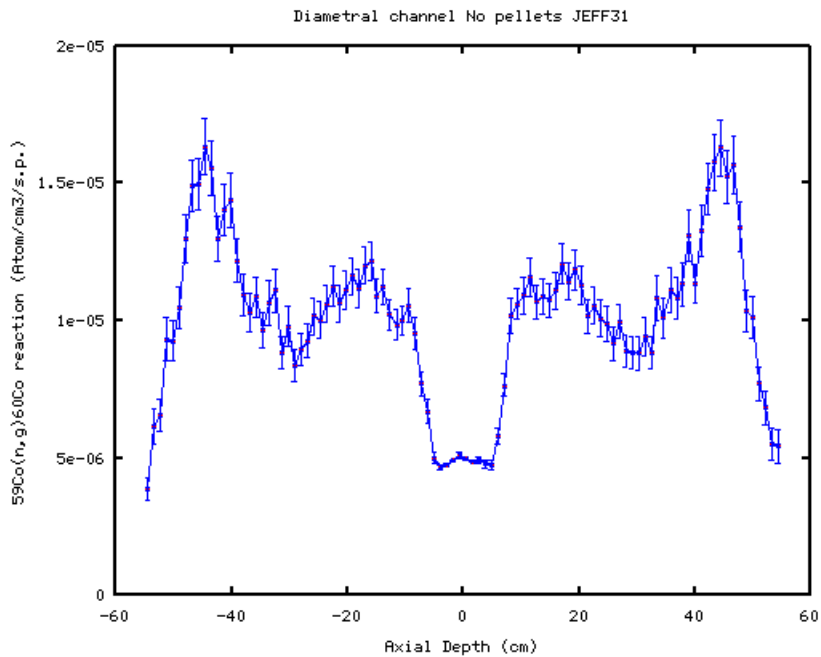


Figure 43 Monte Carlo estimates of  $^{59}\text{Co}(n,\gamma)^{60}\text{Co}$  reaction rate on mesh tally in the diametrical channel of TAPIRO (JEFF31 data set, no pellet, Mesh voxel  $1 \times 1 \times 1 \text{ cm}^3$ ).

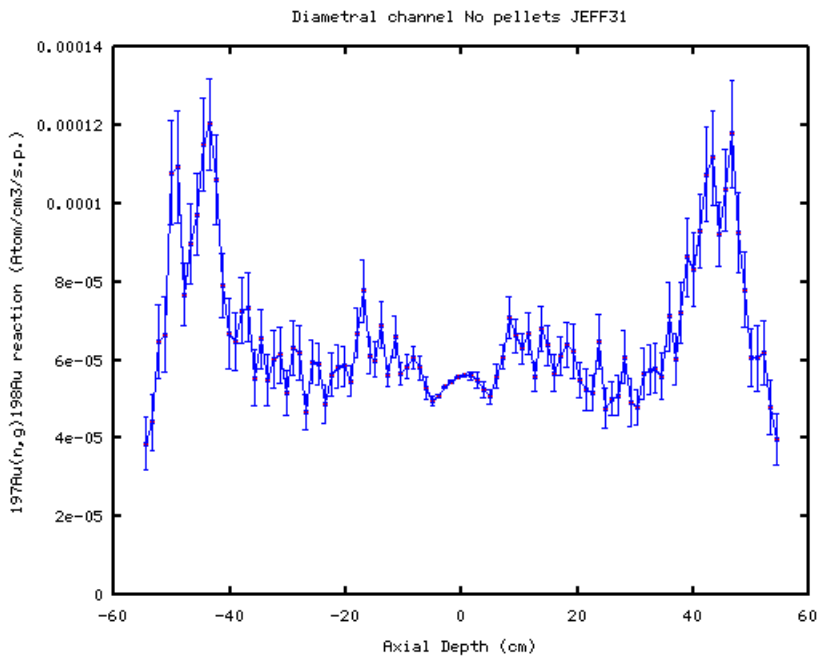


Figure 44 Monte Carlo estimates of  $^{197}\text{Au}(n,\gamma)^{198}\text{Au}$  reaction rate on mesh tally for in the diametrical channel of TAPIRO (JEFF31 data set, no pellet, Mesh voxel  $1 \times 1 \times 1 \text{ cm}^3$ ).

Figure 45 reports  $^{58}\text{Ni}(n,p)^{58}\text{Co}$  reaction rates in diametrical channel (Energy threshold at about 2 MeV – see Figure 41). As expected, the reaction rate follows the spectral behavior of the fast neutron population that monotonically decreases (see Table 11) when the distance from the core axis increases. The behavior in the two halves of the diametrical channel is rather symmetric.

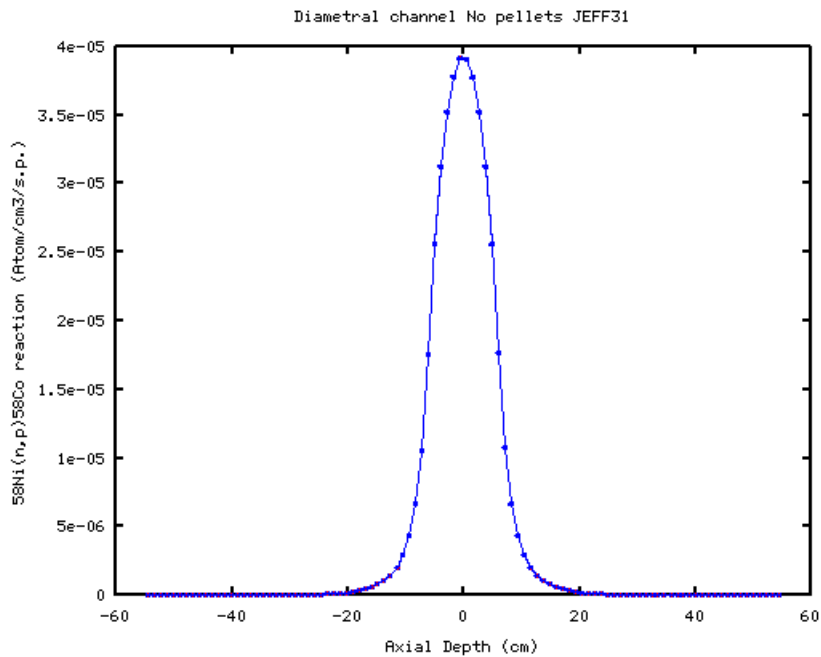


Figure 45 Monte Carlo estimates of  $^{58}\text{Ni}(n,p)^{58}\text{Co}$  reaction rate on mesh tally in the diametrical channel of TAPIRO (JEFF31 data set, no pellet, Mesh voxel  $1 \times 1 \times 1 \text{ cm}^3$ ).

Finally, the  $^{45}\text{Sc}(n,\gamma)^{46}\text{Sc}$  reaction rate (Figure 46) is characterized by an overall decreasing behavior with some relative maximum positioned at 15 cm and 45 cm from the axis core. This behavior should be caused by the contemporary decrease of the fast neutron population and the increase of epithermal neutrons population in the neutron spectra (see Table 11) with distance from core axis.

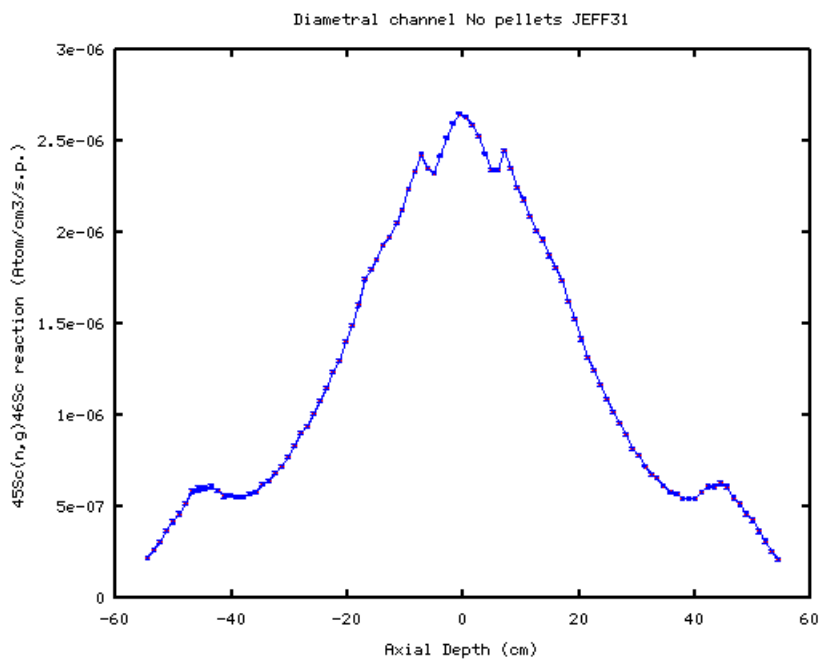


Figure 46 Monte Carlo estimates of  $^{45}\text{Sc}(n,\gamma)^{46}\text{Sc}$  reaction rate on mesh tally in the diametrical channel of TAPIRO (JEFF31 data set, no pellet, Mesh voxel  $1 \times 1 \times 1 \text{ cm}^3$ ).

### Tangential Channel

Table 12 shows the spectral properties of neutron flux in the tangential channel: the epithermal and the fast neutron component of the spectrum monotonically decreases from the core axis to periphery, whereas the thermal component increases becoming not negligible for distance greater than 30 cm. The  $^{59}\text{Co}(n,\gamma)^{60}\text{Co}$  activation rate responses, up to 30 cm of distance from core axis, is dominated by decrease of intensity of the epithermal and fast components (see Figure 47). For distance greater than 30 cm, due to the contribution of the thermal neutron population (see Table 12), the  $^{59}\text{Co}$  reaction rate increases sustained also by the very slow decreases of the epithermal neutron population. The  $^{197}\text{Au}(n,\gamma)^{198}\text{Au}$  reaction rate response (see Figure 48) resembles the one of  $^{59}\text{Co}$  with an increased level of the uncertainty probably due to its greater sensitivity to the thermal neutron population (see Figure 40).

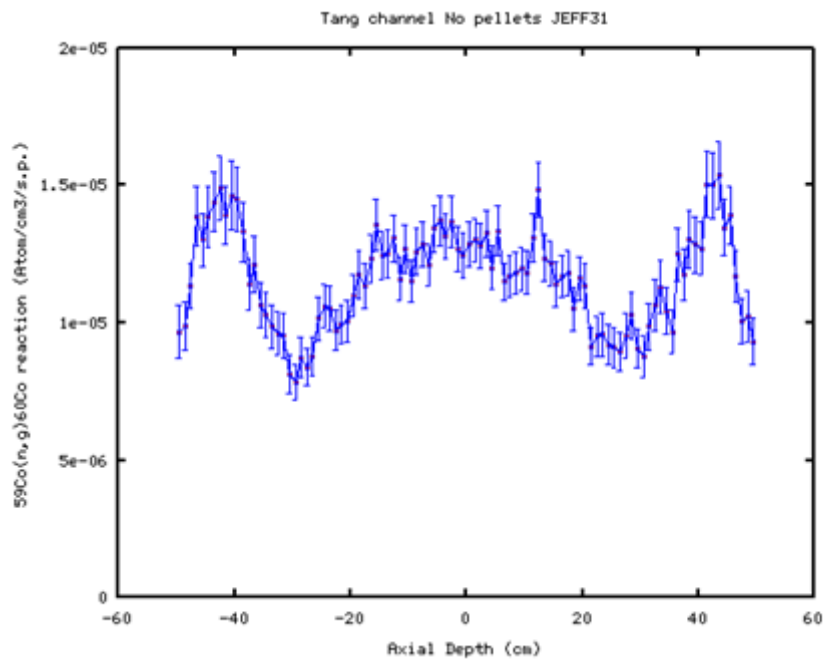


Figure 47 Monte Carlo estimates of  $^{59}\text{Co}(n,\gamma)^{60}\text{Co}$  reaction rate on mesh tally for in the tangential channel of TAPIRO (JEFF31 data set, no pellet, Mesh voxel  $1 \times 1 \times 1 \text{ cm}^3$ ).

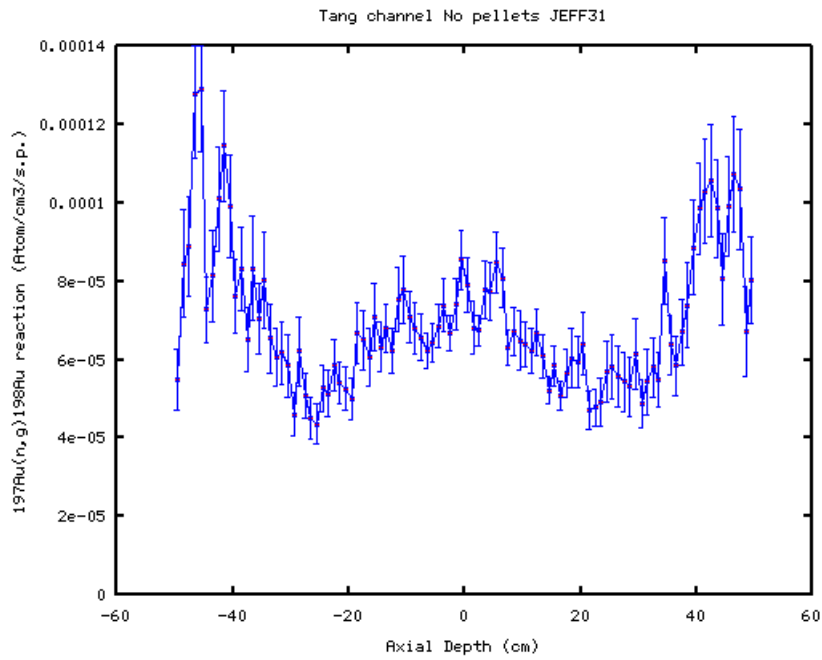


Figure 48 Monte Carlo estimates of  $^{197}\text{Au}(n,\gamma)^{198}\text{Au}$  reaction rate on mesh tally for in the tangential channel of TAPIRO (JEFF31 data set, no pellet, Mesh voxel 1x1x1 cm<sup>3</sup>).

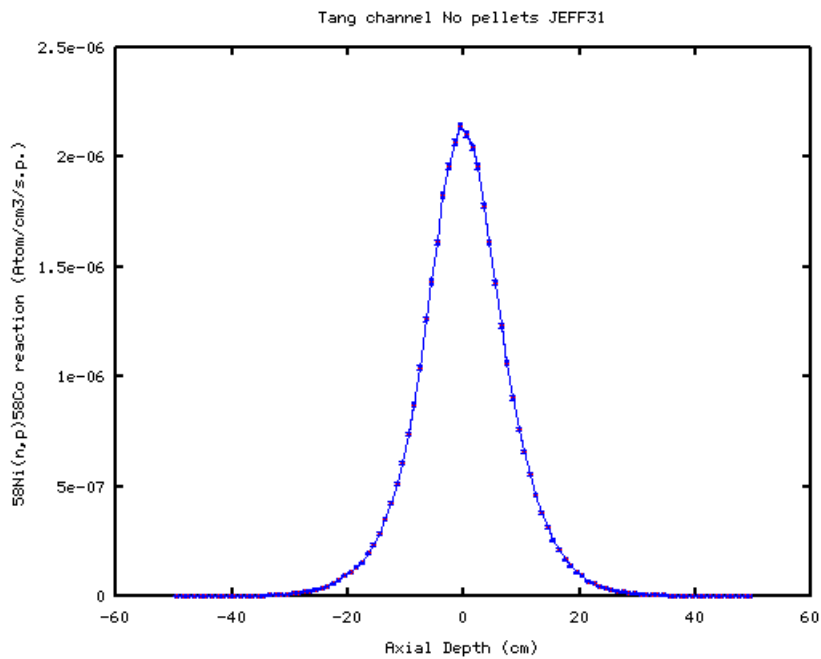


Figure 49 Monte Carlo estimates of  $^{58}\text{Ni}(n,p)^{58}\text{Co}$  reaction rate on mesh tally in the tangential channel of TAPIRO (JEFF31 data set, no pellet, Mesh voxel 1x1x1 cm<sup>3</sup>).

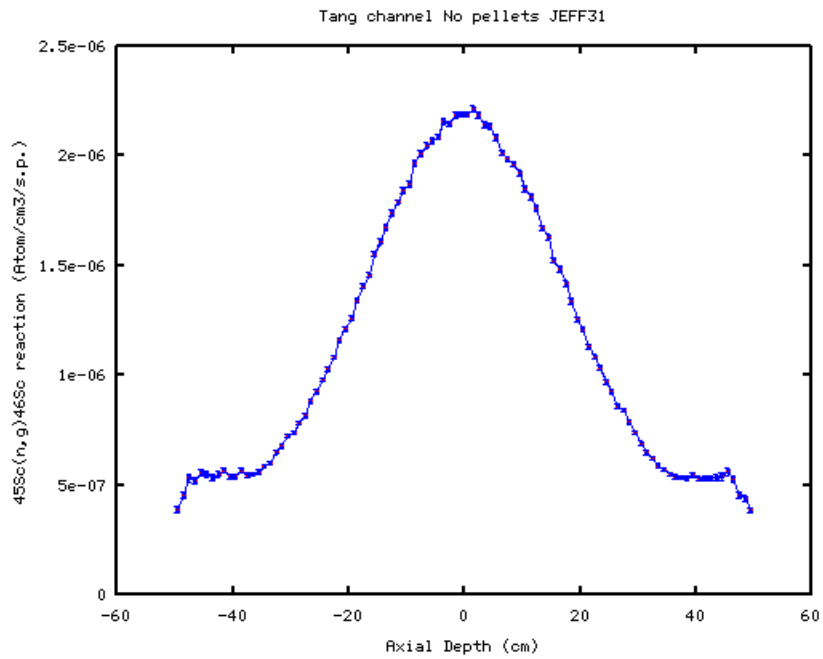


Figure 50 Monte Carlo estimates of  $^{45}\text{Sc}(n,\gamma)^{46}\text{Sc}$  reaction rate on mesh tally in the tangential channel of TAPIRO (JEFF31 data set, no pellet, Mesh voxel  $1 \times 1 \times 1 \text{ cm}^3$ ).

*Radial channel*

The results obtained in the radial channel (see Figure 51 to Figure 54) are in agreement with the spectral characteristics of the neutron flux (see Table 13). Alike diametrical and tangential channels, <sup>59</sup>Co and <sup>197</sup>Au reaction rates in the radial channel are affected by a relatively degree of uncertainty in the mesh tally responses. This feature should be imputed to the strong resonances present in the epithermal range of both nuclides and to the difficult sampling of the rare thermal neutrons population for which the nuclides show very high capture cross section (especially <sup>197</sup>Au).

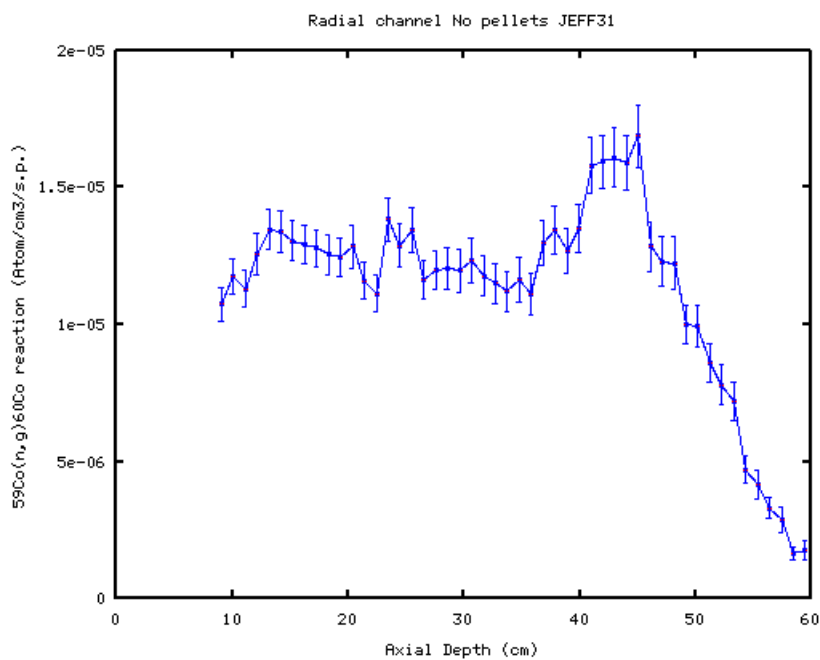


Figure 51 Monte Carlo estimates of <sup>59</sup>Co(n,γ)<sup>60</sup>Co reaction rate on mesh tally in the radial channel of TAPIRO (JEFF31 data set, no pellet, Mesh voxel 1x1x1 cm<sup>3</sup>).

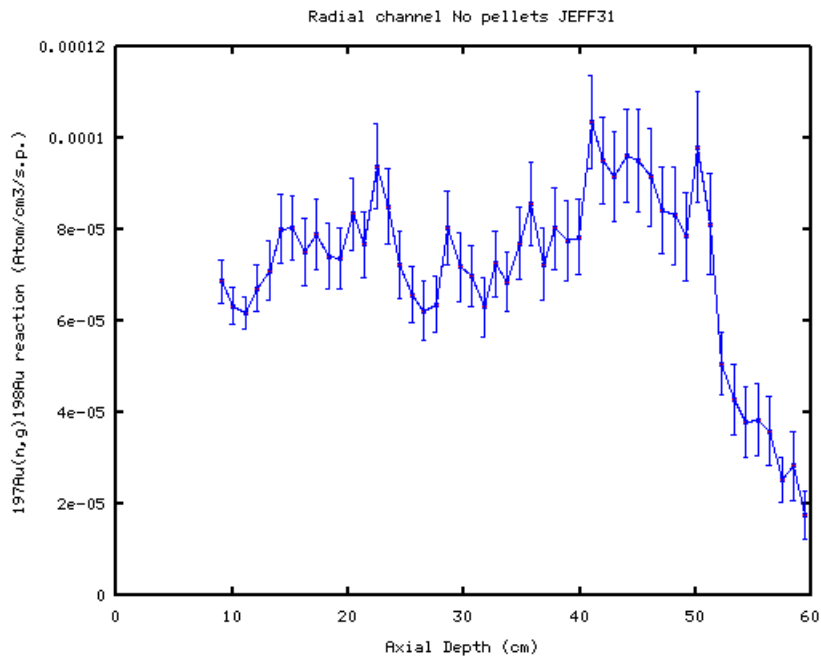


Figure 52 Monte Carlo estimates of  $^{197}\text{Au}(n,\gamma)^{198}\text{Au}$  reaction rate on mesh tally for in the radial channel of TAPIRO (JEFF31 data set, no pellet, Mesh voxel  $1 \times 1 \times 1 \text{ cm}^3$ ).

$^{58}\text{Ni}(n,p)^{58}\text{Co}$  reaction rate decreases with distance for core axis accordingly with the decreases of fast neutron population.

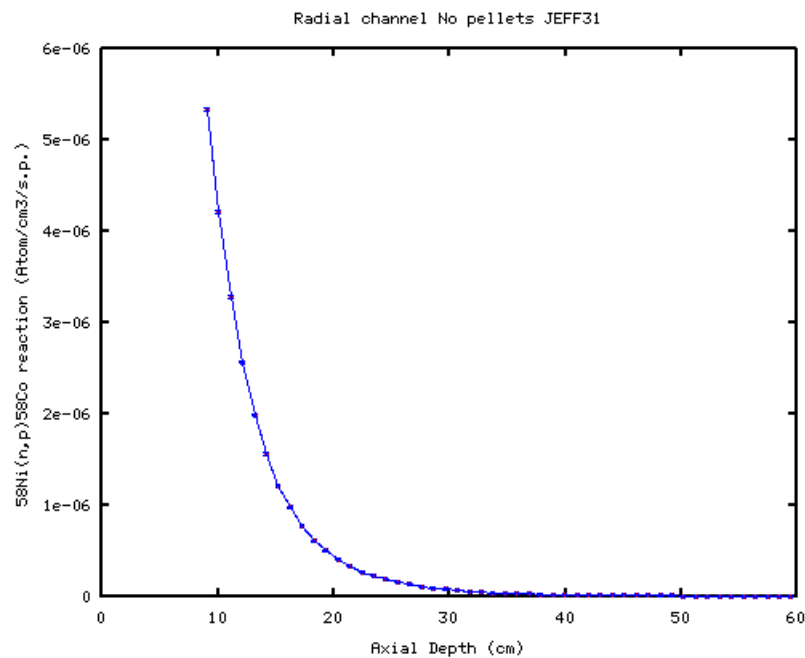


Figure 53 Monte Carlo estimates of  $^{58}\text{Ni}(n,p)^{58}\text{Co}$  reaction rate on mesh tally in the radial channel of TAPIRO (JEFF31 data set, no pellet, Mesh voxel  $1 \times 1 \times 1 \text{ cm}^3$ ).

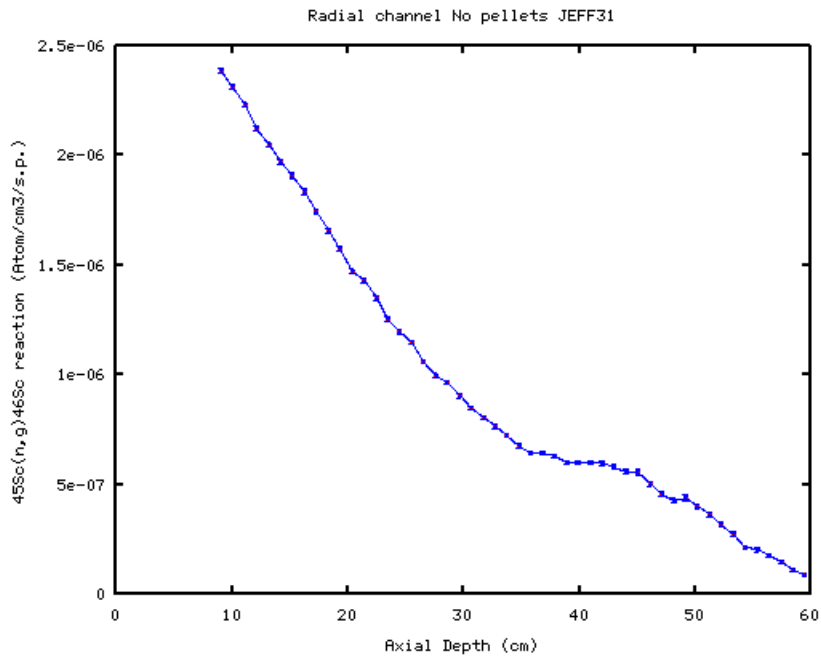


Figure 54 Monte Carlo estimates of  $^{45}\text{Sc}(n,\gamma)^{46}\text{Sc}$  reaction rate on mesh tally in the tangential channel of TAPIRO (JEFF31 data set, no pellet, Mesh voxel 1x1x1 cm<sup>3</sup>).

Finally,  $^{45}\text{Sc}(n,\gamma)^{46}\text{Sc}$  reaction rate decreases with the increasing of the distance from the core axis generating some local flex points and maximum where the thermal-epithermal neutron population increases for the slowing down effects.



## The detector tally (F5) reaction rate responses

The reaction rate for the four selected metals have been estimated in 3 irradiation channels in the same selected points already used for fission rates. Table 24 resumes the calculation plan.

**Table 24 Simulation plan for the F5 detector tally estimations of neutron reaction rate in Radial, Diametrical and Tangential channels**

Simulations	Description
<b>RDetectorTang</b>	Detector Tallies for $^{59}\text{Co}$ , $^{197}\text{Au}$ , $^{45}\text{Sc}$ radiative capture and $^{58}\text{Ni}$ n,p reaction in tangential channel. 11 estimations points from -50 to +50 cm along axis channel. Channel axis is parallel to the X axis of the reference system. No pellets in Diametrical channel. JEFF31 cross section dataset. 4000 iterations for KCODE.
<b>RDetectorDiam</b>	Detector Tallies for $^{59}\text{Co}$ , $^{197}\text{Au}$ , $^{45}\text{Sc}$ radiative capture and $^{58}\text{Ni}$ n,p reaction in Diametrical channel. 11 estimation points from -55 to +55 cm along axis channel. Channel axis is coincident with the Y axis of the reference system. No pellets in Diametrical channel. JEFF31 cross section dataset. 4000 iterations for KCODE.
<b>RDetectorRad</b>	Detector Tallies for $^{59}\text{Co}$ , $^{197}\text{Au}$ , $^{45}\text{Sc}$ radiative capture and $^{58}\text{Ni}$ n,p reaction in Diametrical channel. 6 estimation points from 9 cm to +55 cm along axis channel. Channel axis is coincident with the X axis of the reference system. No pellets in Diametrical channel. JEFF31 cross section dataset. 4000 iterations for KCODE.

### Diametrical channel

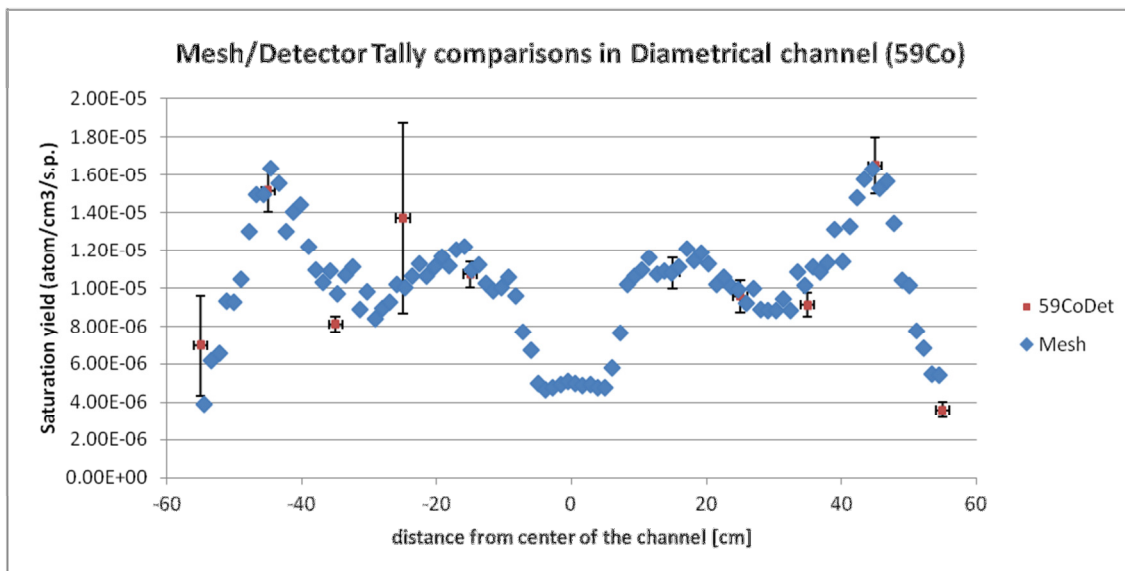


Figure 55 Detector Tally response for  $^{59}\text{Co}(n,\gamma)^{60}\text{Co}$  reaction in the diametrical channel.

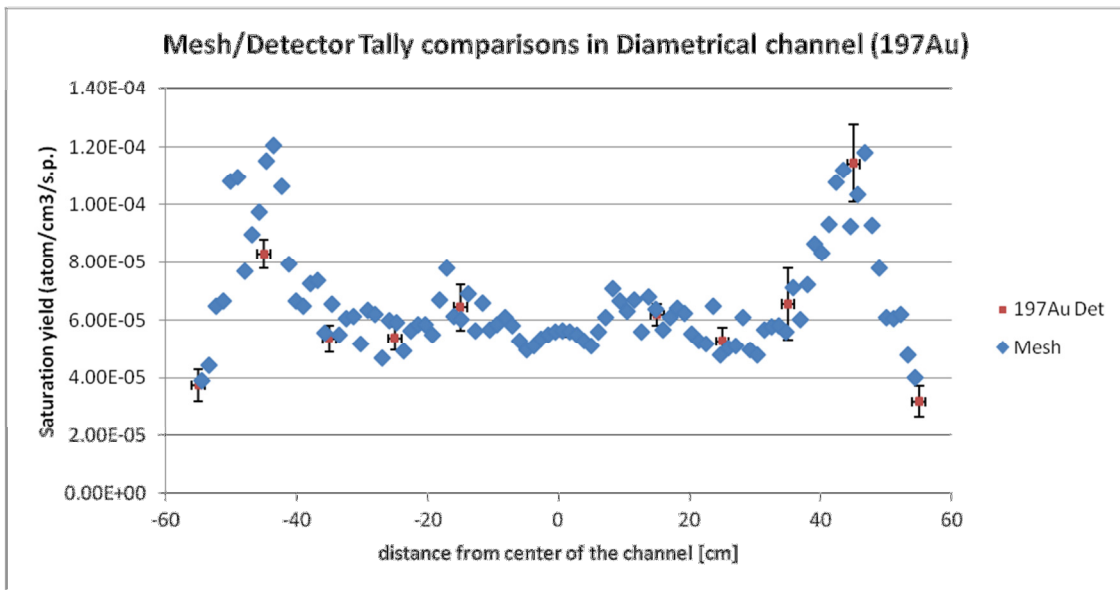


Figure 56 Detector Tally response for  $^{197}\text{Au}(n,\gamma)^{198}\text{Au}$  reaction in the diametrical channel.

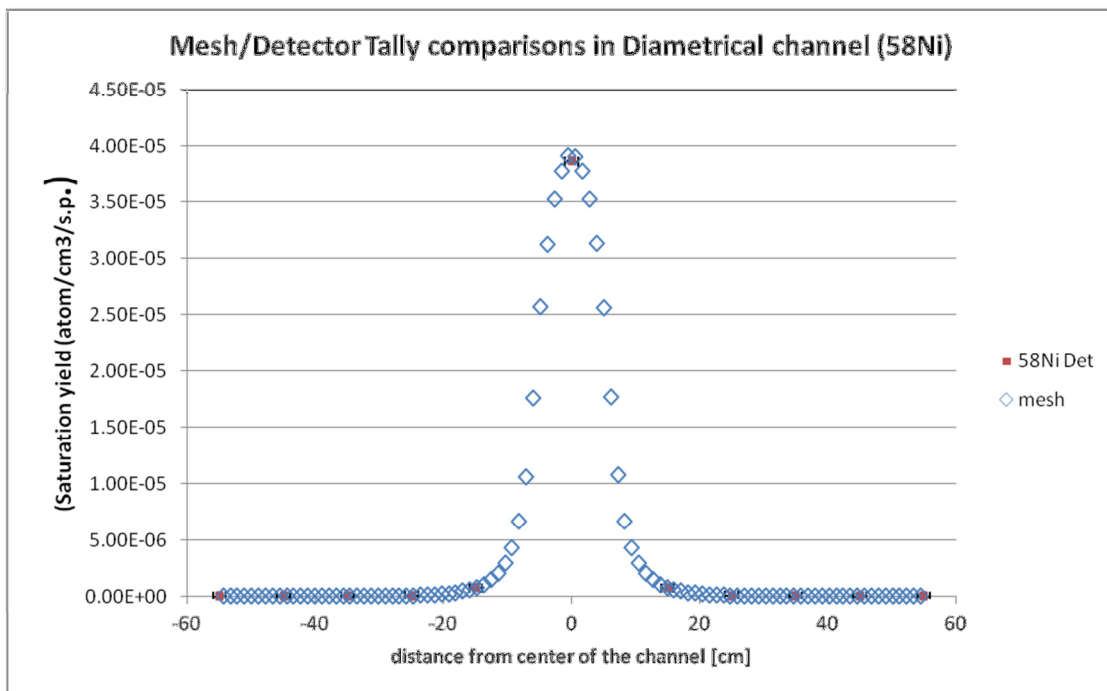


Figure 57 Detector Tally response for  $^{58}\text{Ni}(n,p)^{58}\text{Co}$  reaction in the diametrical channel.

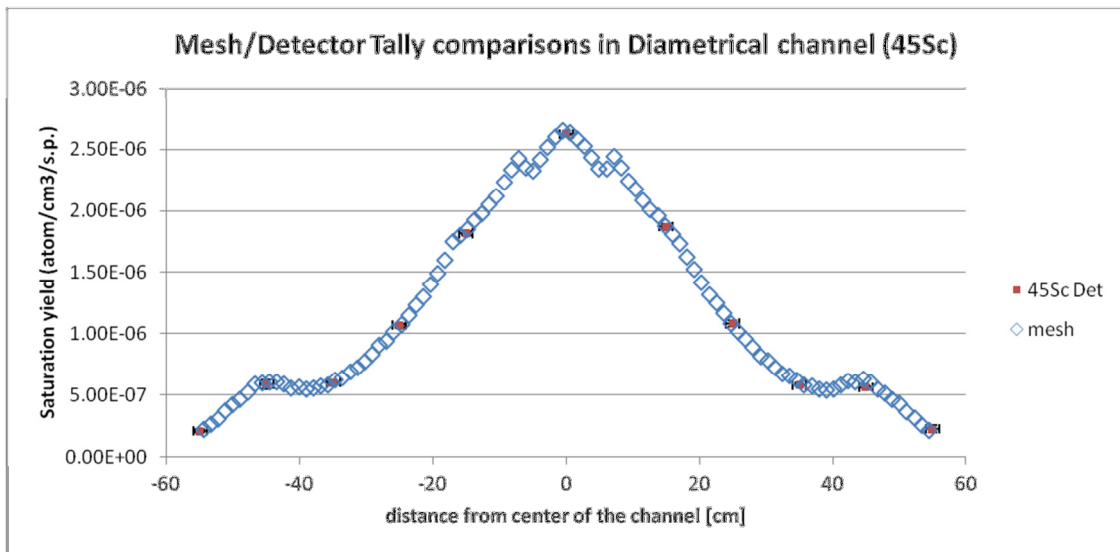


Figure 58 Detector Tally response for  $^{45}\text{Sc}(n,\gamma)^{46}\text{Sc}$  reaction in the diametrical channel.

*Tangential channel*

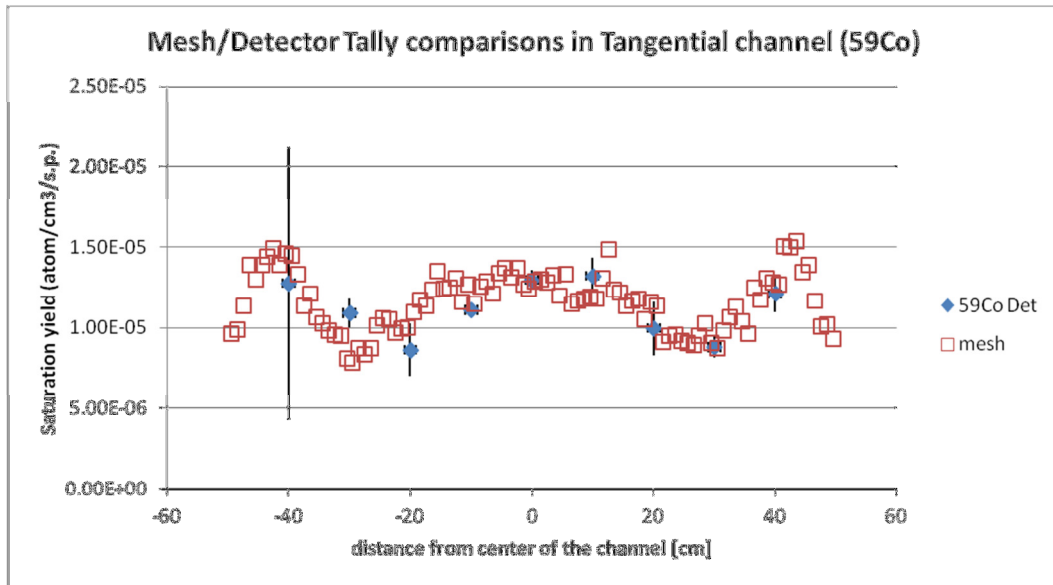


Figure 59 Detector Tally response for  $^{59}\text{Co}(n,\gamma)^{60}\text{Co}$  reaction in the tangential channel.

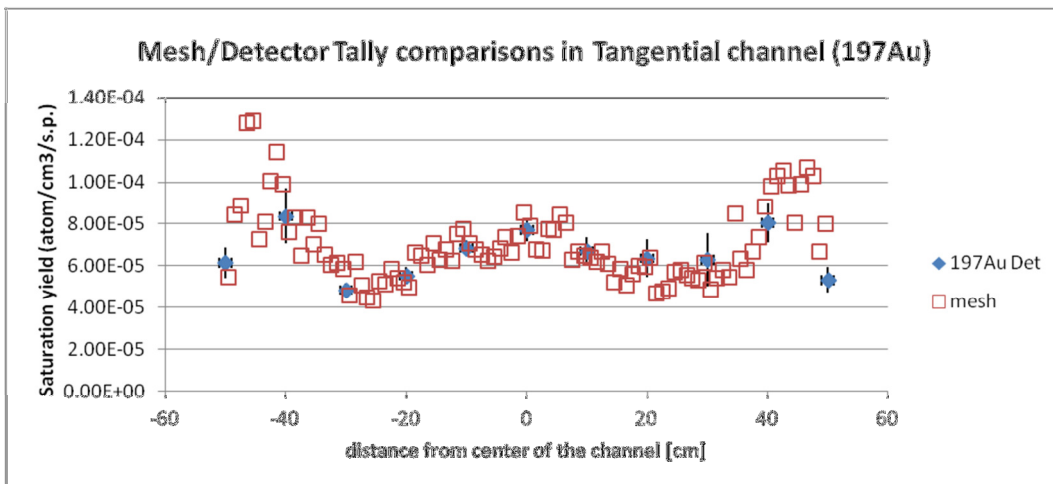


Figure 60 Detector Tally response for  $^{197}\text{Au}(n,\gamma)^{198}\text{Au}$  reaction in the tangential channel.

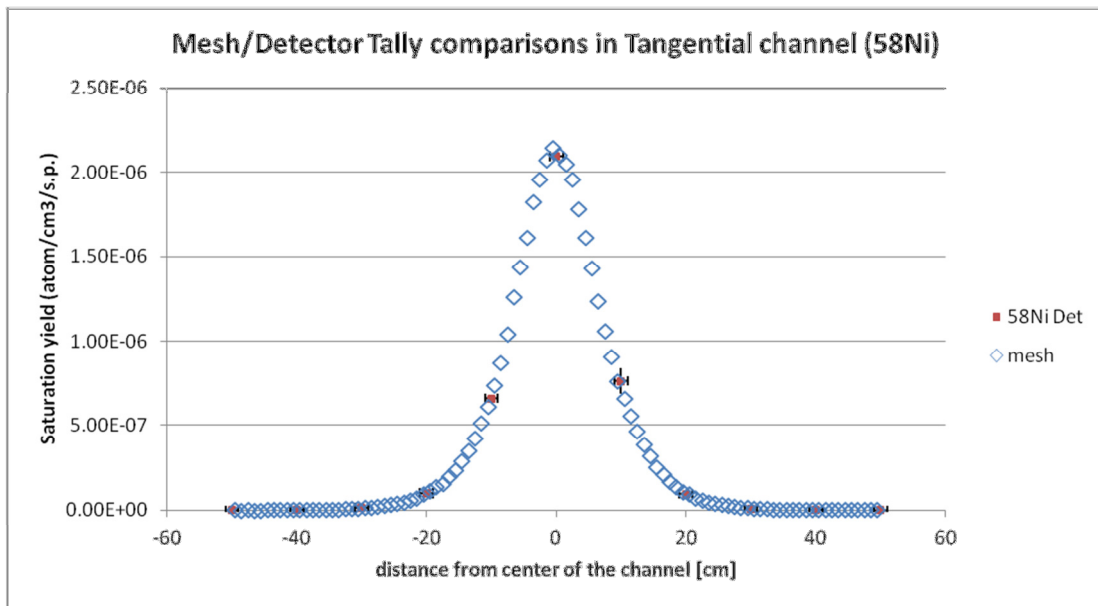


Figure 61 Detector Tally response for  $^{58}\text{Ni}(n,p)^{58}\text{Co}$  reaction in the tangential channel.

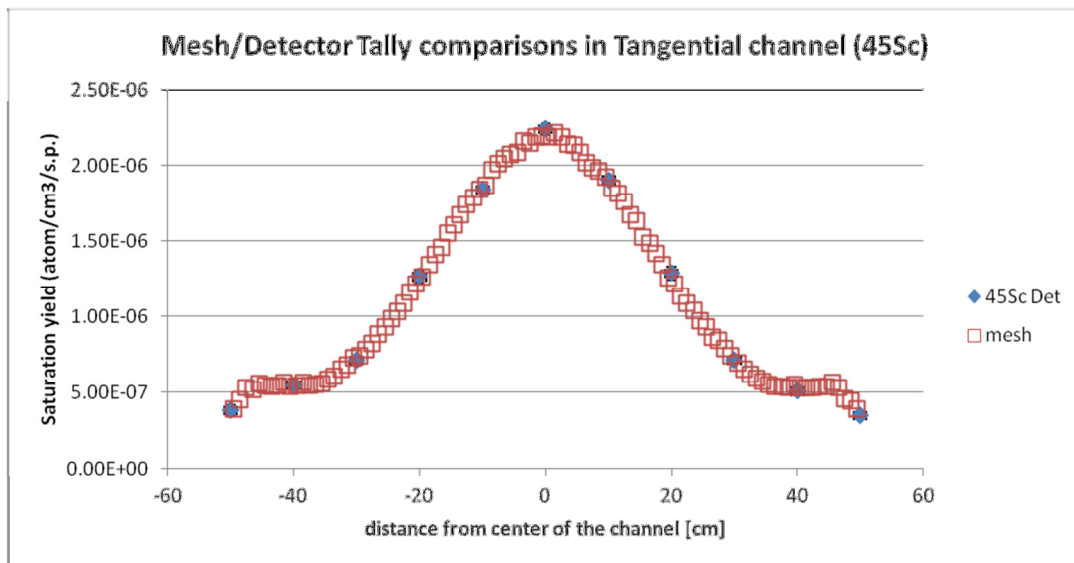


Figure 62 Detector Tally response for  $^{45}\text{Sc}(n,\gamma)^{46}\text{Sc}$  reaction in the tangential channel.

Radial channel

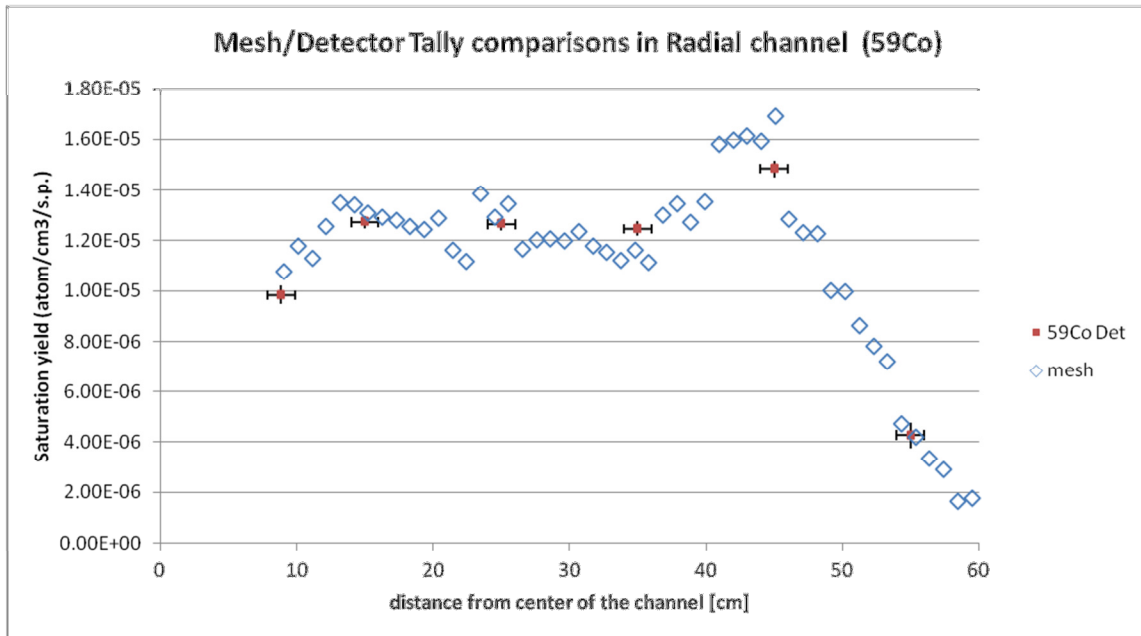


Figure 63 Detector Tally response for  $^{59}\text{Co}(n,\gamma)^{60}\text{Co}$  reaction in the radial channel.

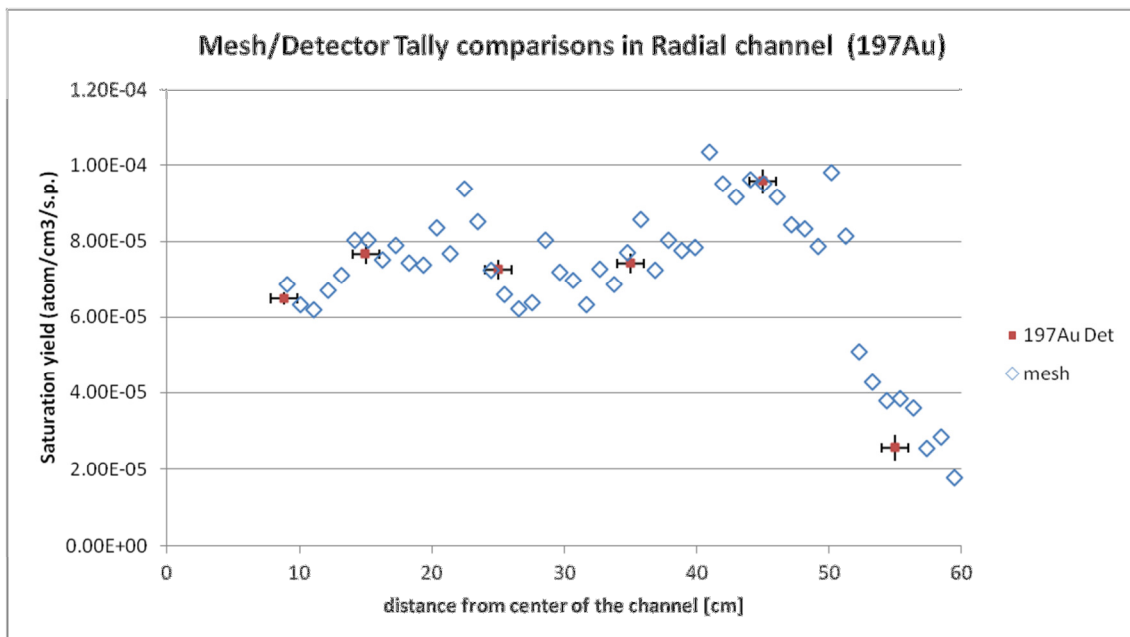


Figure 64 Detector Tally response for  $^{197}\text{Au}(n,\gamma)^{198}\text{Au}$  reaction in the radial channel.

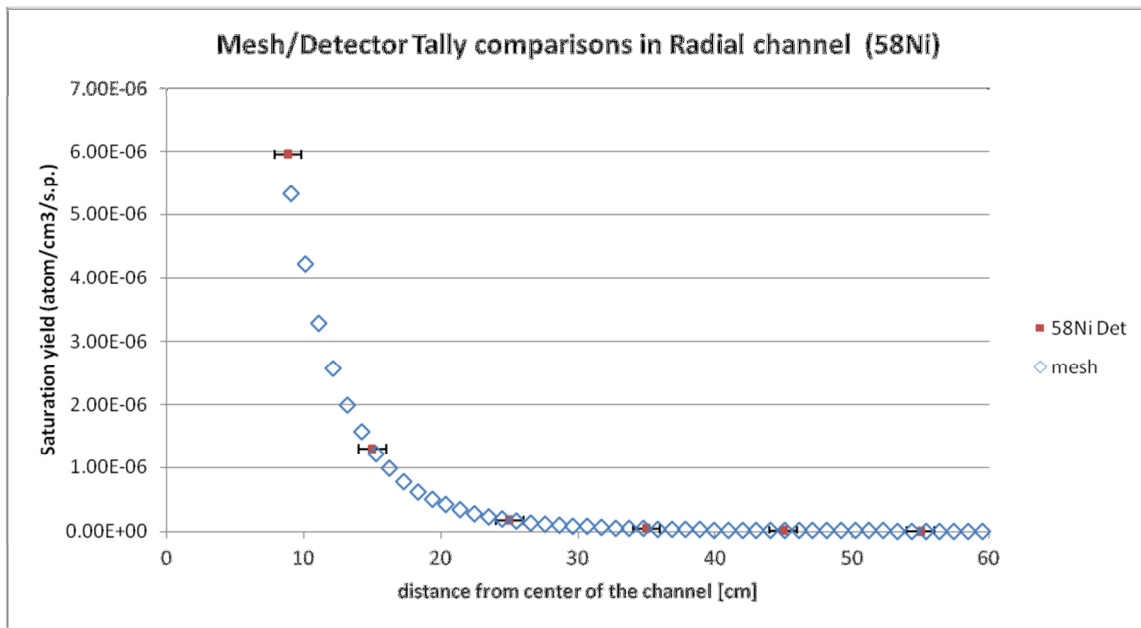


Figure 65 Detector Tally response for  $^{58}\text{Ni}(n,p)^{58}\text{Co}$  reaction in the tangential channel.

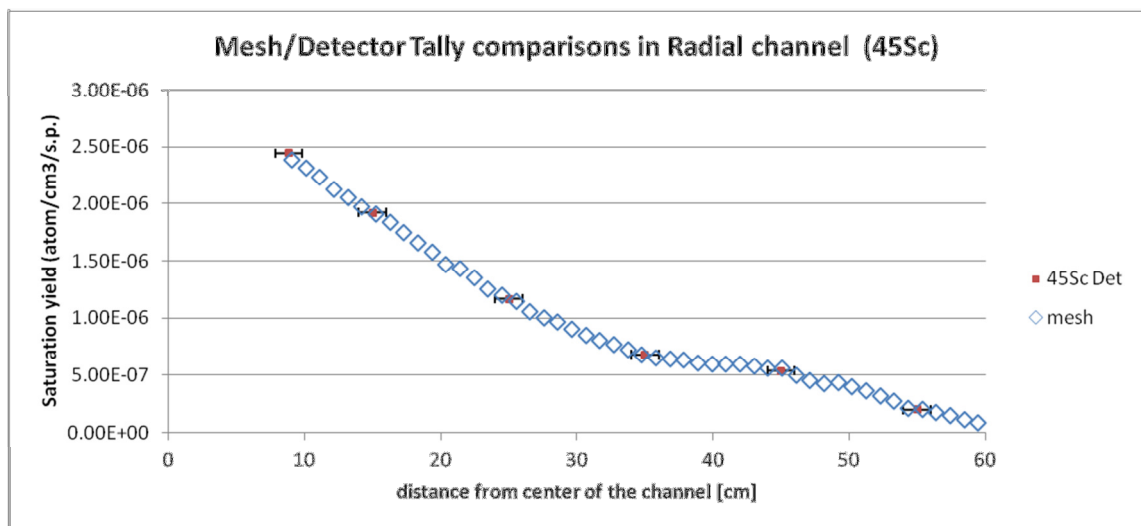


Figure 66 Detector Tally response for  $^{45}\text{Sc}(n,\gamma)^{46}\text{Sc}$  reaction in the radial channel.

In all cases, the comparison between the simulation results of tally F5/detectors and MESH tally appear to furnish statistically equivalent results.

## Comparison of the simulation outcomes with experimental results

As reported in **Errore. L'autoriferimento non è valido per un segnalibro.**, the late experimental raw data have been presented in report [2] normalized accordingly to three normalization method.

Table 25 Normalization method of the late experimental results

Type of measurement	Detector	Units	Method of normalization
Fission rate	Fission chambers	Count per Main monitor Count	Count of fission chamber are divided for the main monitor counter that monitoring reactor power.
Reaction Rate	Metallic foils	Absolute Reaction Rate per Unit Source [Bq/atom/fission]	The saturation activity is divided for the TAPIRO neutron source term as evaluated in [2] Volume 1, section 7.
Reaction Rate	Metallic Foils	Equivalent fission flux per main monitor count [n/cm <sup>2</sup> /s/cps]	Saturation activity is divided for the averaged <sup>235</sup> U fission cross section and for the main monitor counts.

Despite simulated and experimental measurements have been performed in the same ranges of positions, they are generally not coincident. Consequently, the simulated data have been post-processed accordingly with the following algorithm:

1. The  $\beta$ -splines coefficients of the simulated mesh data have been calculated for each considered reaction along the traverses of each channel [8].
2. The values of the simulated reaction rates were calculated by spline interpolation exactly in the same positions where measurements have been performed.
3. Both measured and simulated data sets were normalized at their respective maximum.
4. Measured and simulated data are reported in tabular and graphical formats for comparison.

Experimental data are taken from the various tables reported in Volume 2, section 8 of reference [2]. In the following paragraphs, the late experimental data are reported with their original table numbers.



## Fission rates of <sup>235</sup>U, <sup>238</sup>U, <sup>237</sup>Np and <sup>239</sup>Pu fission chambers.

### Radial Channel 1

As reported in Figure 67 and Figure 68 (see also Table 26 and Table 27), <sup>237</sup>Np and <sup>238</sup>U fission rates show a satisfactory agreement with the experimental data. Both simulated behavior tends to overestimate the experimental data in the zone of major rate change of the fission curve (distance range of 10 cm to 22 cm). <sup>235</sup>U fission (Figure 70 and Table 29) data are in good agreement with experimental findings. The agreement between experimental and simulated data for <sup>239</sup>Pu fission rates is good up to the distance of 40 cm from the core axis (Figure 69 and Table 28). The subsequent maximum at 45 cm is not reproduced by the simulated data. Finally, the <sup>238</sup>U to <sup>235</sup>U fission ratios have been reported for both experimental and simulated data (Figure 71). The simulated results seems to slightly overestimated the fast neutron fraction with respect to the experimental findings.

**Table 26 Comparison of Measured fission rate (Table 8.3.2) and simulated <sup>237</sup>Np fission rate in selected positions on the Radial 1 channel axis.**

*Distance [cm]	Measured Rate		Estimated Rate	
	Fission Rate [Count per Main monitor Count]	Normalized	Fission Rate [fission per s.p.]	Normalized
11.60	8.31E-01	1.00E+00	5.21E-05	1.00E+00
12.74	6.51E-01	7.83E-01	4.24E-05	8.14E-01
13.94	5.07E-01	6.10E-01	3.43E-05	6.58E-01
15.14	4.03E-01	4.85E-01	2.78E-05	5.33E-01
16.40	3.15E-01	3.79E-01	2.23E-05	4.29E-01
17.74	2.47E-01	2.97E-01	1.81E-05	3.47E-01
18.94	2.04E-01	2.45E-01	1.49E-05	2.85E-01
20.14	1.67E-01	2.01E-01	1.22E-05	2.34E-01
21.44	1.37E-01	1.65E-01	9.88E-06	1.90E-01
23.94	9.43E-02	1.13E-01	6.74E-06	1.29E-01
26.44	6.42E-02	7.73E-02	4.64E-06	8.92E-02
28.94	4.39E-02	5.28E-02	3.22E-06	6.18E-02
31.44	3.01E-02	3.62E-02	2.26E-06	4.33E-02
33.94	2.09E-02	2.52E-02	1.58E-06	3.03E-02
36.44	1.44E-02	1.73E-02	1.11E-06	2.12E-02
38.94	9.89E-03	1.19E-02	7.64E-07	1.47E-02
41.44	6.71E-03	8.07E-03	5.53E-07	1.06E-02
43.94	4.69E-03	5.64E-03	3.96E-07	7.61E-03
46.44	3.47E-03	4.18E-03	2.80E-07	5.37E-03
48.94	2.61E-03	3.14E-03	2.13E-07	4.09E-03
50.14	2.24E-03	2.70E-03	1.95E-07	3.74E-03
51.44	1.76E-03	2.12E-03	1.51E-07	2.91E-03
52.74	1.38E-03	1.66E-03	1.06E-07	2.03E-03
53.94	1.07E-03	1.29E-03	7.94E-08	1.53E-03
56.44	6.34E-04	7.63E-04	4.71E-08	9.05E-04
58.94	3.73E-04	4.49E-04	2.61E-08	5.01E-04
61.44	2.15E-04	2.59E-04	2.63E-08	5.04E-04

\* For radial and diametrical channel distance on channel axis taking origin in the intersection of core axis with channel axis . For tangential channel the origin is the intersection of the translation of the core axis (- 10.6 cm along y axis of MCNP reference system) with the channel axis.

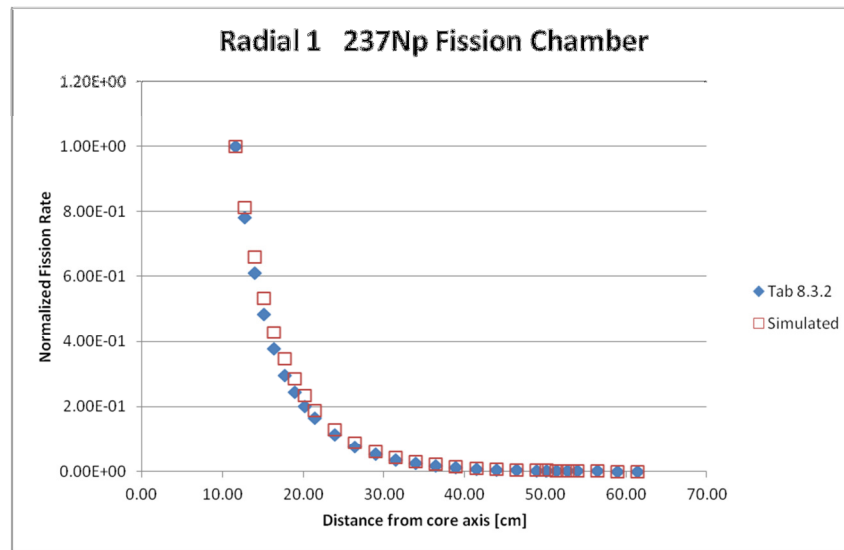


Figure 67 Comparison of experimental vs. simulated responses of <sup>237</sup>Np fission chambers along Radial 1 channel.

Table 27 Comparison of Measured fission rate (Table 8.3.6) and simulated <sup>238</sup>U fission rate in selected positions on the Radial 1 channel axis.

*Distance [cm]	Measured Rate		Estimated Rate	
	Fission Rate [Count per Main monitor Count]	Normalized	Fission Rate [fission per s.p.]	Normalized
11.59	1.40E-01	1.00E+00	5.33E-06	1.00E+00
12.69	1.01E-01	7.21E-01	4.11E-06	7.71E-01
13.89	7.24E-02	5.17E-01	3.13E-06	5.87E-01
15.09	5.27E-02	3.76E-01	2.39E-06	4.49E-01
16.39	3.79E-02	2.71E-01	1.79E-06	3.37E-01
17.69	2.76E-02	1.97E-01	1.38E-06	2.59E-01
18.89	2.06E-02	1.47E-01	1.09E-06	2.04E-01
20.09	1.58E-02	1.13E-01	8.55E-07	1.61E-01
21.39	1.18E-02	8.43E-02	6.66E-07	1.25E-01
23.39	6.98E-03	4.99E-02	4.21E-07	7.89E-02
26.39	4.13E-03	2.95E-02	2.75E-07	5.16E-02
28.89	2.51E-03	1.79E-02	1.81E-07	3.40E-02
31.39	1.52E-03	1.09E-02	1.25E-07	2.35E-02
33.89	9.45E-04	6.75E-03	8.65E-08	1.62E-02
36.39	5.98E-04	4.27E-03	6.19E-08	1.16E-02
38.89	3.86E-04	2.76E-03	4.47E-08	8.40E-03
41.39	2.45E-04	1.75E-03	3.51E-08	6.60E-03
43.89	1.73E-04	1.24E-03	2.62E-08	4.93E-03
46.39	1.32E-04	9.43E-04	2.09E-08	3.93E-03

\* For radial and diametrical channel distance on channel axis taking origin in the intersection of core axis with channel axis . For tangential channel the origin is the intersection of the translation of the core axis (- 10.6 cm along y axis of MCNP reference system) with the channel axis.

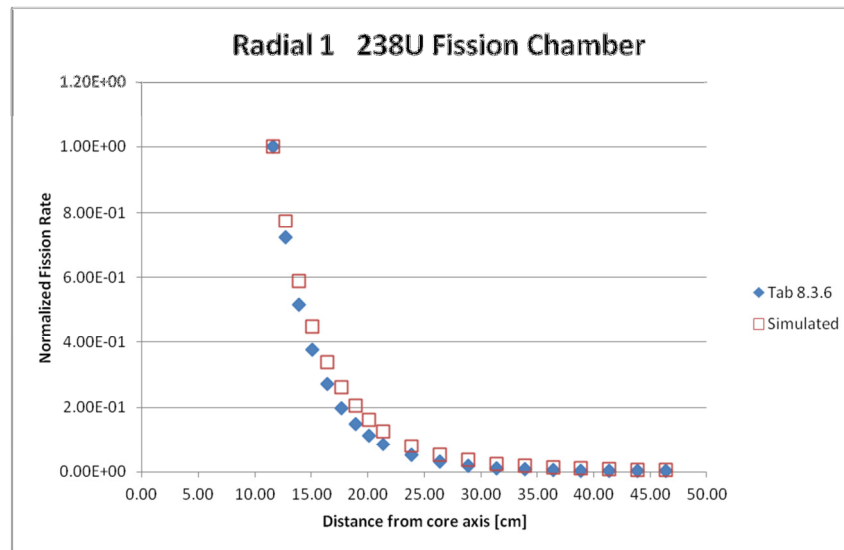


Figure 68 : Comparison of experimental vs. simulated responses <sup>238</sup>U fission chambers along Radial 1 channel.

Table 28 Comparison of Measured fission rate (Table 8.3.22) and simulated <sup>239</sup>Pu fission rate in selected positions on the Radial 1 channel axis.

*Distance [cm]	Measured Rate		Estimated Rate	
	Fission Rate [Count per Main monitor Count]	Normalized	Fission Rate [fission per s.p.]	Normalized
1.12E+01	2.46E+00	1.00E+00	1.86E-04	1.00E+00
1.16E+01	2.34E+00	9.51E-01	1.79E-04	9.60E-01
1.26E+01	2.09E+00	8.50E-01	1.62E-04	8.68E-01
1.38E+01	1.87E+00	7.60E-01	1.45E-04	7.75E-01
1.50E+01	1.66E+00	6.75E-01	1.29E-04	6.91E-01
1.63E+01	1.49E+00	6.06E-01	1.16E-04	6.21E-01
1.76E+01	1.33E+00	5.41E-01	1.04E-04	5.60E-01
1.88E+01	1.22E+00	4.96E-01	9.37E-05	5.03E-01
2.00E+01	1.12E+00	4.55E-01	8.56E-05	4.59E-01
2.13E+01	1.03E+00	4.19E-01	7.76E-05	4.16E-01
2.38E+01	8.65E-01	3.52E-01	6.37E-05	3.42E-01
2.63E+01	7.30E-01	2.97E-01	5.38E-05	2.89E-01
2.88E+01	6.20E-01	2.52E-01	4.57E-05	2.45E-01
3.13E+01	5.31E-01	2.16E-01	3.87E-05	2.07E-01
3.38E+01	4.60E-01	1.87E-01	3.53E-05	1.89E-01
3.63E+01	4.18E-01	1.70E-01	3.24E-05	1.74E-01
3.88E+01	4.07E-01	1.65E-01	3.28E-05	1.76E-01
4.13E+01	4.51E-01	1.83E-01	3.61E-05	1.94E-01
4.38E+01	7.39E-01	3.00E-01	3.50E-05	1.88E-01
4.63E+01	9.18E-01	3.73E-01	3.19E-05	1.71E-01
4.88E+01	7.48E-01	3.04E-01	2.85E-05	1.53E-01
5.13E+01	4.52E-01	1.84E-01	2.08E-05	1.12E-01
52.28	-	-	2.06E-05	1.11E-01
53.31	-	-	1.64E-05	8.81E-02
54.34	-	-	1.49E-05	8.01E-02
55.37	-	-	1.24E-05	6.67E-02
56.40	-	-	1.16E-05	6.24E-02
57.43	-	-	9.70E-06	5.20E-02
58.46	-	-	8.93E-06	4.79E-02
59.49	-	-	6.38E-06	3.42E-02

\* For radial and diametrical channel distance on channel axis taking origin in the intersection of core axis with channel axis . For tangential channel the origin is the intersection of the translation of the core axis (- 10.6 cm on y axis of MCNP reference system) with the channel axis.

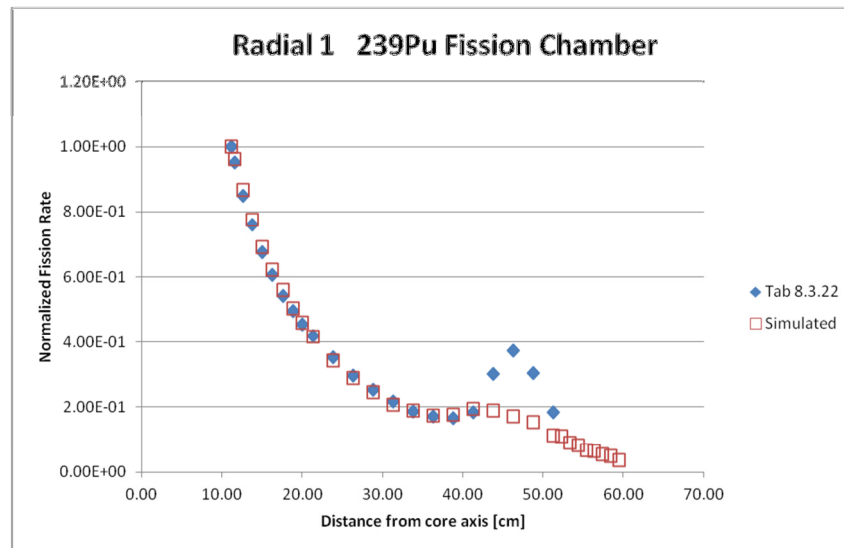
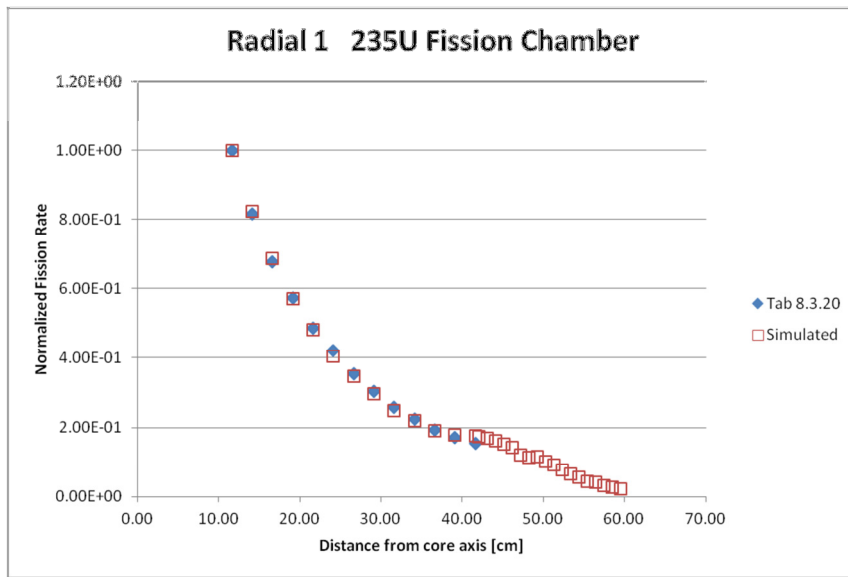


Figure 69 Comparison of experimental vs. simulated responses of <sup>239</sup>Pu fission chambers along Radial 1 channel.

Table 29 Comparison of Measured fission rate (Table 8.3.20) and simulated <sup>235</sup>U fission rate in selected positions on the Radial 1 channel axis.

*Distance [cm]	Measured Rate		Estimated Rate	
	Fission Rate [Count per Main monitor Count]	Normalized	Fission Rate [fission per s.p.]	Normalized
1.16E+01	3.91E+00	1.00E+00	1.55E-04	1.00E+00
1.41E+01	3.19E+00	8.16E-01	1.28E-04	8.25E-01
1.66E+01	2.65E+00	6.78E-01	1.06E-04	6.86E-01
1.91E+01	2.24E+00	5.73E-01	8.84E-05	5.70E-01
2.16E+01	1.90E+00	4.86E-01	7.46E-05	4.81E-01
2.41E+01	1.65E+00	4.22E-01	6.29E-05	4.05E-01
2.66E+01	1.39E+00	3.55E-01	5.37E-05	3.46E-01
2.91E+01	1.19E+00	3.04E-01	4.60E-05	2.97E-01
3.16E+01	1.01E+00	2.58E-01	3.85E-05	2.48E-01
3.41E+01	8.75E-01	2.24E-01	3.42E-05	2.21E-01
3.66E+01	7.57E-01	1.94E-01	2.96E-05	1.91E-01
3.91E+01	6.68E-01	1.71E-01	2.78E-05	1.79E-01
4.16E+01	6.06E-01	1.55E-01	2.73E-05	1.76E-01
41.9925	-	-	2.7E-05	1.74E-01
43.0215	-	-	2.63E-05	1.69E-01
44.0505	-	-	2.52E-05	1.63E-01
45.0795	-	-	2.36E-05	1.52E-01
46.1085	-	-	2.2E-05	1.42E-01
47.1375	-	-	1.9E-05	1.22E-01
48.1665	-	-	1.76E-05	1.14E-01
49.1955	-	-	1.79E-05	1.15E-01
50.2245	-	-	1.58E-05	1.02E-01
51.2535	-	-	1.42E-05	9.16E-02
52.2825	-	-	1.21E-05	7.82E-02
53.3115	-	-	1.03E-05	6.66E-02
54.3405	-	-	8.81E-06	5.68E-02
55.3695	-	-	6.93E-06	4.47E-02
56.3985	-	-	6.42E-06	4.14E-02
57.4275	-	-	5.15E-06	3.32E-02
58.4565	-	-	4.39E-06	2.83E-02
59.4855	-	-	3.36E-06	2.17E-02

\* For radial and diametrical channel distance on channel axis taking origin in the intersection of core axis with channel axis . For tangential channel the origin is the intersection of the translation of the core axis (- 10.6 cm on y axis of MCNP reference system) with the channel axis.



b)

Figure 70 Comparison of experimental vs. simulated responses of <sup>235</sup>U fission chambers along Radial 1 channel.

Table 30 Comparison of the measured and estimated <sup>238</sup>U/<sup>235</sup>U fissions ratio in the Radial channel 1

*Distance [cm]	Measured Fissions Rate ratio	Simulated Fission Ratio
11.62	3.55E-02	3.41E-02
14.12	2.13E-02	2.32E-02
16.62	1.35E-02	1.61E-02
19.12	8.72E-03	1.18E-02
21.62	5.90E-03	8.55E-03
24.12	4.04E-03	6.43E-03
26.62	2.83E-03	4.93E-03
29.12	2.02E-03	3.79E-03
31.62	1.44E-03	3.14E-03
34.12	1.04E-03	2.45E-03
36.62	7.58E-04	2.03E-03
39.12	5.55E-04	1.57E-03
41.62	3.89E-04	1.26E-03

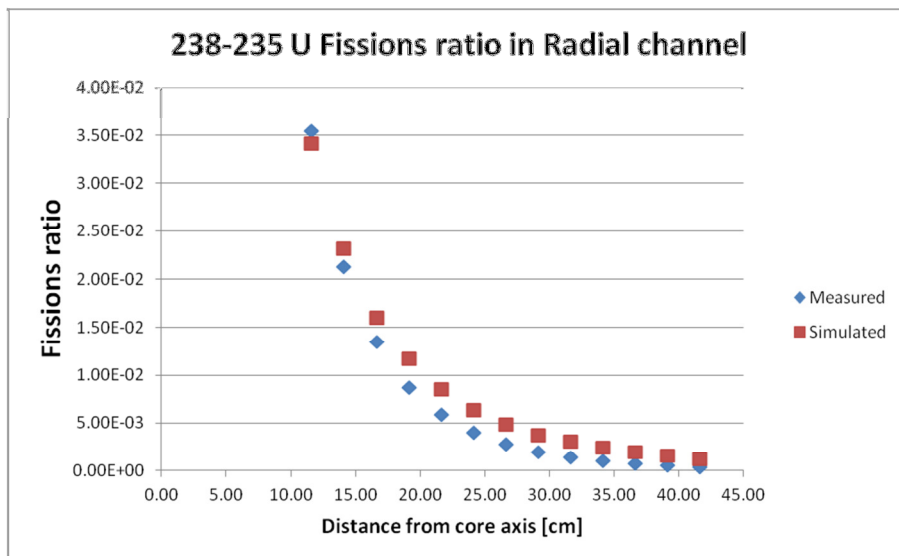


Figure 71 Comparison of the measured and estimated <sup>238</sup>U/<sup>235</sup>U fissions ratio in the Radial channel 1.

*Tangential Channel (A)*

As reported in Figure 4, the branch A of the tangential channel is the one from the side of the Helium duct. <sup>238</sup>U (see Figure 73 and Table 32) and <sup>237</sup>Np (see Figure 72 and Table 31) fission rate data are in good agreement with the experimental behavior with a slightly tendency to overestimation. <sup>239</sup>Pu (Figure 74 and Table 33) fission data are also in good agreement with the experimental findings with a slightly overestimation of the experimental data up to 15 cm of distance to core axis. For distance greater than 15 cm, simulated data underestimate experimental data.

**Table 31 Comparison of Measured fission rate (Table 8.3.5) and simulated <sup>237</sup>Np fission rate in selected positions on the Tangential channel (A) axis.**

*Distance [cm]	Measured Rate		Estimated Rate	
	Fission Rate [Count per Main monitor Count]	Normalized	Fission Rate [fission per s.p.]	Normalized
5.51	7.03E-01	1.00E+00	3.59E-05	1.00E+00
5.83	6.81E-01	9.69E-01	3.49E-05	9.72E-01
6.38	6.40E-01	9.10E-01	3.31E-05	9.23E-01
7.09	5.89E-01	8.38E-01	3.07E-05	8.57E-01
7.99	5.28E-01	7.51E-01	2.79E-05	7.78E-01
8.99	4.64E-01	6.60E-01	2.50E-05	6.96E-01
9.97	4.08E-01	5.80E-01	2.20E-05	6.14E-01
11.00	3.55E-01	5.05E-01	1.95E-05	5.44E-01
12.14	3.07E-01	4.37E-01	1.71E-05	4.76E-01
13.05	2.70E-01	3.84E-01	1.52E-05	4.25E-01
14.43	2.27E-01	3.23E-01	1.27E-05	3.55E-01
16.77	1.67E-01	2.38E-01	9.47E-06	2.64E-01
19.15	1.27E-01	1.81E-01	6.90E-06	1.92E-01
21.56	9.24E-02	1.31E-01	4.91E-06	1.37E-01
23.99	6.59E-02	9.37E-02	3.52E-06	9.80E-02
26.43	4.72E-02	6.71E-02	2.50E-06	6.96E-02

\* For radial and diametrical channel distance on channel axis taking origin in the intersection of core axis with channel axis . For tangential channel the origin is the intersection of the translation of the core axis (- 10.6 cm on y axis of MCNP reference system) with the channel axis.

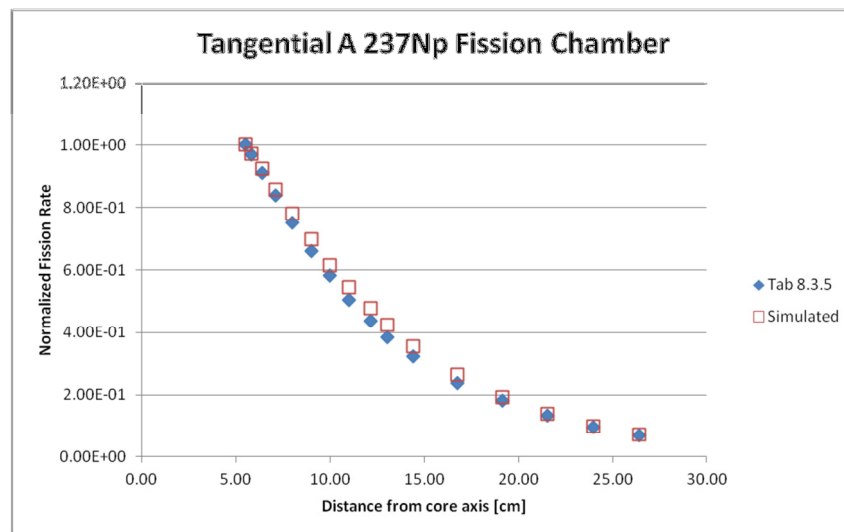


**Figure 72 Comparison of experimental vs. simulated responses <sup>237</sup>Np fission chambers along Tangential A channel.**

Table 32 Comparison of Measured fission rate (Table 8.3.9) and simulated <sup>238</sup>U fission rate in selected positions on the Tangential channel (A) axis.

*Distance [cm]	Measured Rate		Estimated Rate	
	Fission Rate [Count per Main monitor Count]	Normalized	Fission Rate [fission per s.p.]	Normalized
5.51	1.08E-01	1.00E+00	2.88E-06	1.00E+00
5.81	1.03E-01	9.54E-01	2.78E-06	9.66E-01
6.35	9.54E-02	8.83E-01	2.60E-06	9.05E-01
7.05	8.56E-02	7.93E-01	2.34E-06	8.14E-01
7.95	7.35E-02	6.81E-01	2.04E-06	7.09E-01
8.95	6.15E-02	5.69E-01	1.75E-06	6.07E-01
9.93	5.18E-02	4.80E-01	1.46E-06	5.08E-01
10.95	4.31E-02	3.99E-01	1.23E-06	4.27E-01
12.10	3.51E-02	3.25E-01	1.02E-06	3.54E-01
13.00	3.02E-02	3.00E-01	8.66E-07	3.01E-01
14.38	2.29E-02	2.12E-01	6.77E-07	2.35E-01
16.72	1.51E-02	1.40E-01	4.49E-07	1.56E-01
19.10	1.02E-02	9.44E-02	2.93E-07	1.02E-01
21.51	6.95E-03	6.44E-02	1.88E-07	6.52E-02
23.94	4.49E-03	4.16E-02	1.17E-07	4.07E-02

\* For radial and diametrical channel distance on channel axis taking origin in the intersection of core axis with channel axis . For tangential channel the origin is the intersection of the translation of the core axis (- 10.6 cm on y axis of MCNP reference system) with the channel axis.

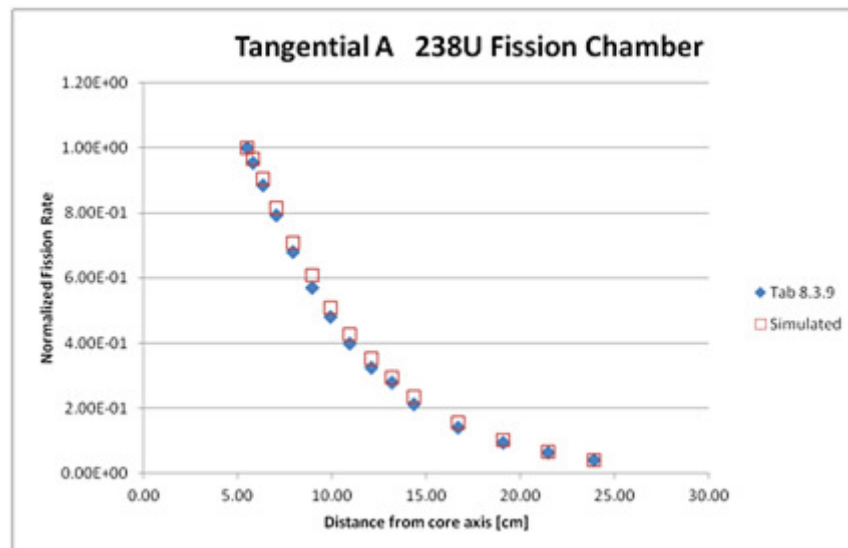


Figure 73 Comparison of experimental vs. simulated responses <sup>238</sup>U fission chambers along Tangential A channel.

Table 33 Comparison of Measured fission rate (Table 8.3.25) and simulated <sup>239</sup>Pu fission rate in selected positions on the Tangential channel (A) axis.

*Distance [cm]	Measured Rate		Estimated Rate	
	Fission Rate [Count per Main monitor Count]	Normalized	Fission Rate [fission per s.p.]	Normalized
5.55	2.17E+00	1.00E+00	1.51E-04	1.00E+00
5.78	2.13E+00	9.82E-01	1.49E-04	9.90E-01
6.30	2.08E+00	9.59E-01	1.45E-04	9.65E-01
6.99	2.00E+00	9.22E-01	1.41E-04	9.33E-01
7.88	1.89E+00	8.71E-01	1.34E-04	8.90E-01
8.87	1.79E+00	8.25E-01	1.26E-04	8.36E-01
9.84	1.70E+00	7.83E-01	1.19E-04	7.89E-01
10.87	1.59E+00	7.33E-01	1.13E-04	7.47E-01
12.01	1.49E+00	6.87E-01	1.04E-04	6.93E-01
12.91	1.41E+00	6.50E-01	9.83E-05	6.53E-01
14.29	1.31E+00	6.04E-01	9.12E-05	6.05E-01
16.63	1.14E+00	5.25E-01	7.83E-05	5.19E-01
19.01	1.00E+00	4.61E-01	6.57E-05	4.36E-01
21.42	8.63E-01	3.98E-01	5.54E-05	3.68E-01
23.84	7.43E-01	3.42E-01	4.74E-05	3.14E-01
26.28	6.42E-01	2.96E-01	4.03E-05	2.68E-01
28.74	5.61E-01	2.59E-01	3.56E-05	2.36E-01
31.19	4.92E-01	2.27E-01	3.20E-05	2.12E-01
33.66	4.39E-01	2.02E-01	2.90E-05	1.92E-01
36.13	3.99E-01	1.84E-01	2.74E-05	1.82E-01
38.60	3.75E-01	1.73E-01	2.92E-05	1.94E-01

\* For radial and diametrical channel distance on channel axis taking origin in the intersection of core axis with channel axis . For tangential channel the origin is the intersection of the translation of the core axis (- 10.6 cm on y axis of MCNP reference system) with the channel axis.

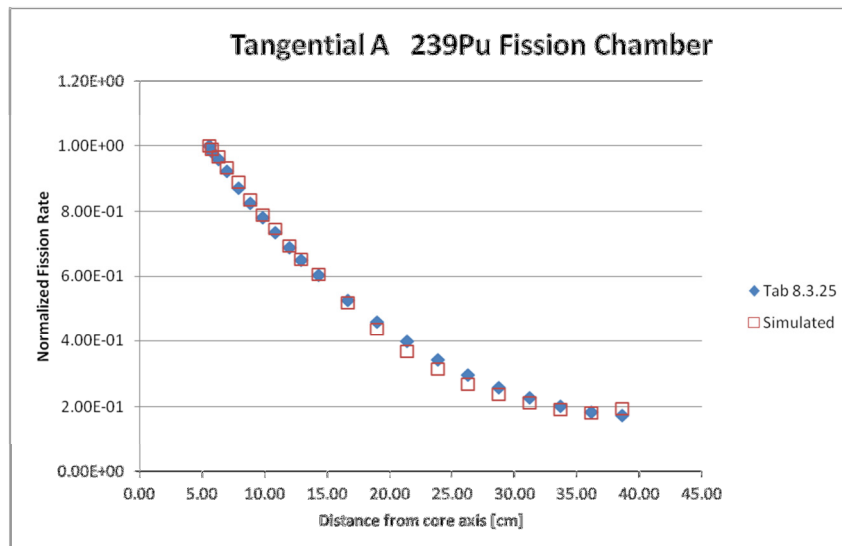


Figure 74 Comparison of experimental vs. simulated responses of <sup>239</sup>Pu fission chambers along Tangential A channel.



### Tangential Channel (B)

Branch B of the tangential channel is the one from the side of the regulation rod RR (see Figure 4). As already observed for Tangential channel (A),  $^{238}\text{U}$  (see Figure 76 and Table 35) and  $^{237}\text{Np}$  (see Figure 75 and Table 34) experimental and simulated data are in good agreement, in both cases a slight overestimation of the experimental behavior is present.  $^{239}\text{Pu}$  (Figure 77 and Table 36) fission data show the same trend already observed in Tangential channel (A). Up to 20 cm of distance to core axis, simulated data overestimate experimental data and, for distance greater than 20 cm, they begin to underestimate experimental data.

**Table 34 Comparison of Measured fission rate (Table 8.3.4) and simulated  $^{237}\text{Np}$  fission rate in selected positions on the Tangential channel (B) axis.**

*Distance [cm]	Measured Rate		Estimated Rate	
	Fission Rate [Count per Main monitor Count]	Normalized	Fission Rate [fission per s.p.]	Normalized
5.96	6.83E-01	1.00E+00	3.46E-05	1.00E+00
6.25	6.54E-01	9.58E-01	3.36E-05	9.72E-01
6.76	6.16E-01	9.02E-01	3.20E-05	9.24E-01
7.42	5.66E-01	8.29E-01	2.98E-05	8.62E-01
8.28	5.06E-01	7.41E-01	2.74E-05	7.92E-01
9.25	4.51E-01	6.60E-01	2.46E-05	7.12E-01
10.20	3.93E-01	5.75E-01	2.20E-05	6.35E-01
11.21	3.42E-01	5.01E-01	1.95E-05	5.65E-01
12.33	2.95E-01	4.32E-01	1.71E-05	4.96E-01
13.22	2.62E-01	3.84E-01	1.53E-05	4.41E-01
14.58	2.15E-01	3.15E-01	1.27E-05	3.66E-01
16.90	1.58E-01	2.31E-01	9.20E-06	2.66E-01
19.26	1.15E-01	1.68E-01	6.60E-06	1.91E-01
21.66	8.34E-02	1.22E-01	4.67E-06	1.35E-01
24.08	5.90E-02	8.64E-02	3.29E-06	9.50E-02
26.51	4.27E-02	6.25E-02	2.31E-06	6.67E-02
31.40	2.19E-02	3.21E-02	1.13E-06	3.27E-02
36.33	1.12E-02	1.64E-02	5.44E-07	1.57E-02

\* For radial and diametrical channel distance on channel axis taking origin in the intersection of core axis with channel axis . For tangential channel the origin is the intersection of the translation of the core axis (- 10.6 cm on y axis of MCNP reference system) with the channel axis.

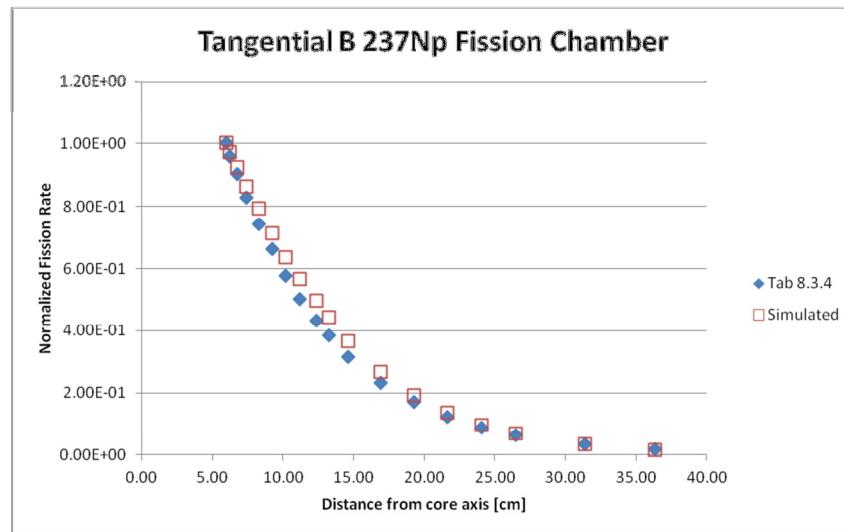


Figure 75 Comparison of experimental vs. simulated responses of <sup>237</sup>Np fission chambers along Tangential B channel.

Table 35 Comparison of Measured fission rate (Table 8.3.8) and simulated <sup>238</sup>U fission rate in selected positions on the Tangential channel (B) axis.

*Distance [cm]	Measured Rate		Estimated Rate	
	Fission Rate [Count per Main monitor Count]	Normalized	Fission Rate [fission per s.p.]	Normalized
5.95	1.03E-01	1.00E+00	2.74E-06	1.00E+00
6.23	9.79E-02	9.50E-01	2.64E-06	9.62E-01
6.73	8.99E-02	8.73E-01	2.46E-06	8.97E-01
7.39	7.99E-02	7.76E-01	2.24E-06	8.18E-01
8.25	6.85E-02	6.65E-01	1.98E-06	7.23E-01
9.21	5.75E-02	5.58E-01	1.72E-06	6.29E-01
10.16	4.81E-02	4.67E-01	1.48E-06	5.40E-01
11.16	4.03E-02	3.91E-01	1.26E-06	4.60E-01
12.29	3.29E-02	3.19E-01	1.07E-06	3.89E-01
13.18	2.76E-02	2.68E-01	9.11E-07	3.32E-01
14.54	2.12E-02	2.06E-01	6.97E-07	2.54E-01
16.85	1.37E-02	1.33E-01	4.42E-07	1.61E-01
19.22	8.68E-03	8.43E-02	2.83E-07	1.03E-01
21.61	5.88E-03	5.71E-02	1.75E-07	6.39E-02

\* For radial and diametrical channel distance on channel axis taking origin in the intersection of core axis with channel axis . For tangential channel the origin is the intersection of the translation of the core axis (- 10.6 cm on y axis of MCNP reference system) with the channel axis.

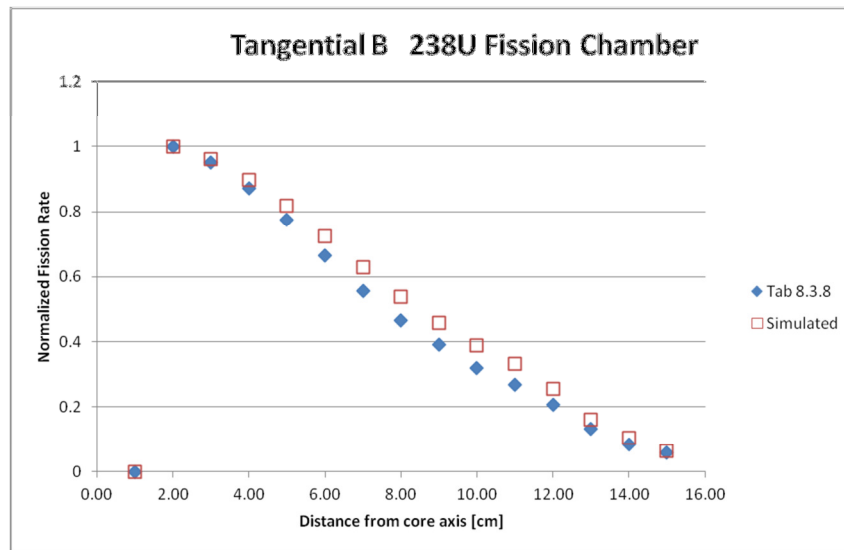


Figure 76 Comparison of experimental vs. simulated responses of 238U fission chambers along Tangential B channel.

Table 36 Comparison of Measured fission rate (Table 8.3.24) and simulated <sup>239</sup>Pu fission rate in selected positions on the Tangential channel (B) axis.

*Distance [cm]	Measured Rate		Estimated Rate	
	Fission Rate [Count per Main monitor Count]	Normalized	Fission Rate [fission per s.p.]	Normalized
5.95	2.15E+00	1.00E+00	1.48E-04	1.00E+00
6.20	2.12E+00	9.86E-01	1.47E-04	9.90E-01
6.68	2.05E+00	9.53E-01	1.44E-04	9.70E-01
7.33	1.96E+00	9.12E-01	1.39E-04	9.39E-01
8.18	1.87E+00	8.70E-01	1.33E-04	8.99E-01
9.13	1.76E+00	8.19E-01	1.26E-04	8.49E-01
10.08	1.66E+00	7.72E-01	1.19E-04	8.02E-01
11.08	1.55E+00	7.21E-01	1.12E-04	7.55E-01
12.20	1.44E+00	6.70E-01	1.05E-04	7.07E-01
13.09	1.38E+00	6.42E-01	9.90E-05	6.68E-01
14.45	1.28E+00	5.95E-01	9.14E-05	6.16E-01
16.76	1.11E+00	5.16E-01	7.68E-05	5.18E-01
19.12	9.59E-01	4.46E-01	6.68E-05	4.50E-01
21.52	8.28E-01	3.85E-01	5.52E-05	3.73E-01
23.93	7.14E-01	3.32E-01	4.62E-05	3.11E-01
26.36	6.15E-01	2.86E-01	4.07E-05	2.74E-01
28.80	5.41E-01	2.52E-01	3.49E-05	2.36E-01
31.26	4.76E-01	2.21E-01	3.07E-05	2.07E-01
33.71	4.26E-01	1.98E-01	2.81E-05	1.90E-01
36.18	3.90E-01	1.81E-01	2.57E-05	1.73E-01
38.65	3.67E-01	1.71E-01	2.82E-05	1.90E-01

\* For radial and diametrical channel distance on channel axis taking origin in the intersection of core axis with channel axis . For tangential channel the origin is the intersection of the translation of the core axis (- 10.6 cm on y axis of MCNP reference system) with the channel axis.

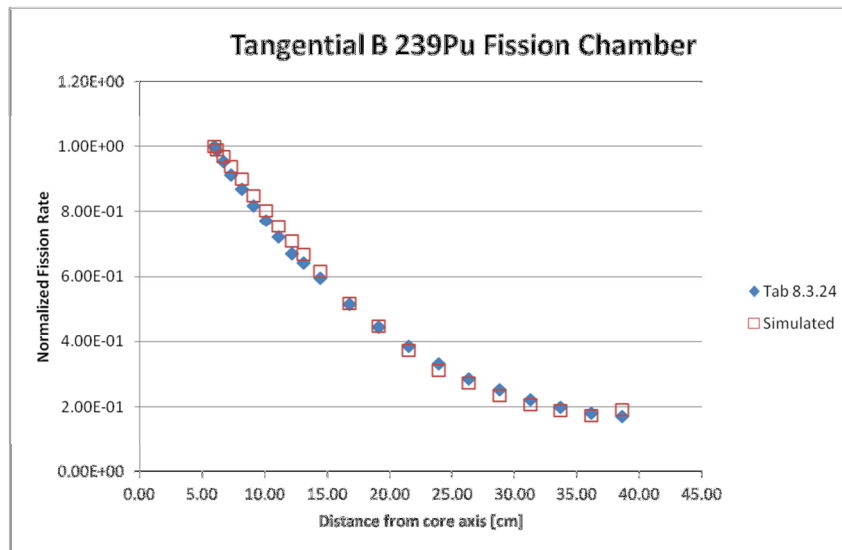


Figure 77 Comparison of experimental vs. simulated responses of <sup>239</sup>Pu fission chambers along Tangential B channel.

### Diametrical Channel

As reported in Figure 78 and Table 37, the simulated responses of  $^{237}\text{Np}$  fission chamber are in good agreement with the experimental values.

**Table 37 Comparison of Measured fission rate (Table 8.3.1) and simulated  $^{237}\text{Np}$  fission rate in selected positions on the Diametrical channel axis.**

*Distance [cm]	Measured Rate		Estimated Rate	
	Fission Rate [Count per Main monitor Count]	Normalized	Fission Rate [fission per s.p.]	Normalized
0.55	7.20E-17	1.00E+00	3.60E-04	1.00E+00
6.67	3.23E-17	4.49E-01	1.57E-04	4.36E-01
7.73	2.28E-17	3.17E-01	1.15E-04	3.18E-01
9.15	1.61E-17	2.24E-01	7.75E-05	2.15E-01
10.60	1.13E-17	1.57E-01	5.55E-05	1.54E-01

\* For radial and diametrical channel distance on channel axis taking origin in the intersection of core axis with channel axis . For tangential channel the origin is the intersection of the translation of the core axis (- 10.6 cm on y axis of MCNP reference system) with the channel axis.

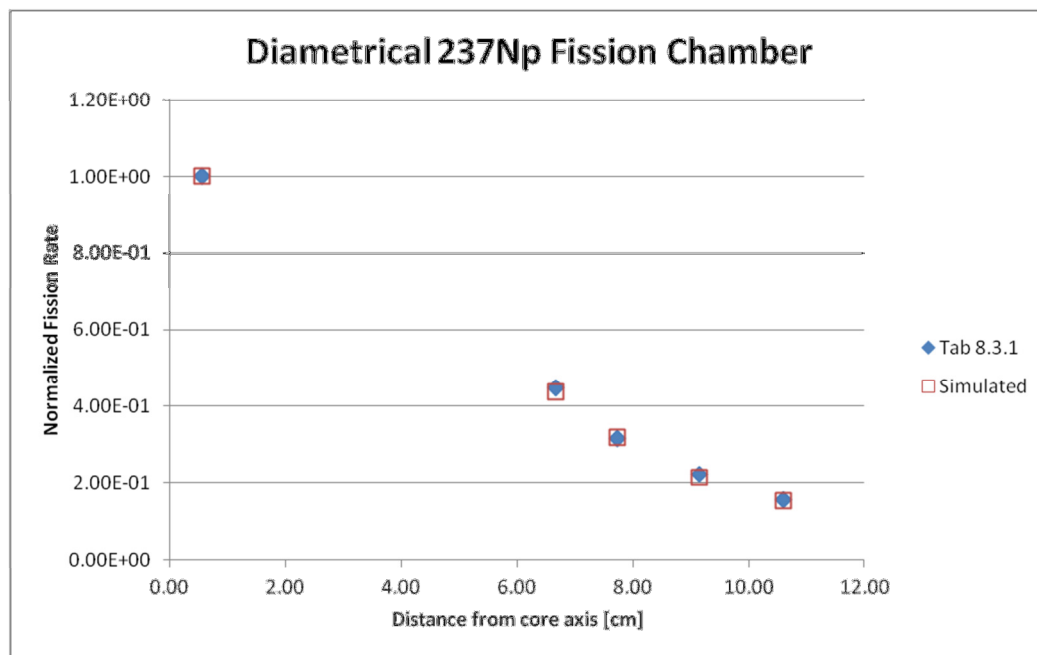


**Figure 78 Comparison of experimental vs. simulated responses for  $^{237}\text{Np}$  fission chamber along Diametrical channel.**

## Activation rates for Au, Ni, Co and Sc activation foils.

### Diametrical channel (B)

As already stated, the branch B of the diametrical channel is the one located on the side of the regulation rod (RR - see Figure 4). Table 38 and Figure 79, clearly show that simulated activation rate for the reaction  $^{45}\text{Sc}(n,\gamma)^{46}\text{Sc}$  follows the same trend of the experimental findings with slightly tendency to overestimation. A very good agreement has been found for  $^{58}\text{Ni}(n,p)^{58}\text{Co}$  reaction (see Figure 80 and Table 39).  $^{59}\text{Co}(n,\gamma)^{60}\text{Co}$  is in relatively good agreement with experimental findings (see Table 40 and Figure 81). Conversely,  $^{197}\text{Au}(n,\gamma)^{198}\text{Au}$  simulated reaction rate responses (Figure 82 and Table 41) do not agree with the experimental findings.

Table 38 Comparison of measured (Table 8.3.33) and simulated  $^{45}\text{Sc}(n,\gamma)^{46}\text{Sc}$  reaction rate in selected positions on the Diametrical (B) channel axis.

*Distance [cm]	Measured Rate		Estimated Rate	
	Absolute Reaction Rate per Unit Source [Bq/atom/fission]	Normalized	Reaction Rate [atom/cm <sup>3</sup> per s.p.]	Normalized
0.37	6.98E-29	1.00E+00	2.64E-06	1.00E+00
6.77	6.17E-29	8.84E-01	2.42E-06	9.19E-01
7.93	6.22E-29	8.91E-01	2.39E-06	9.07E-01
9.44	5.76E-29	8.25E-01	2.24E-06	8.51E-01
11.00	5.43E-29	7.78E-01	2.14E-06	8.12E-01

\* For radial and diametrical channel distance on channel axis taking origin in the intersection of core axis with channel axis . For tangential channel the origin is the intersection of the translation of the core axis (- 10.6 cm on y axis of MCNP reference system) with the channel axis.

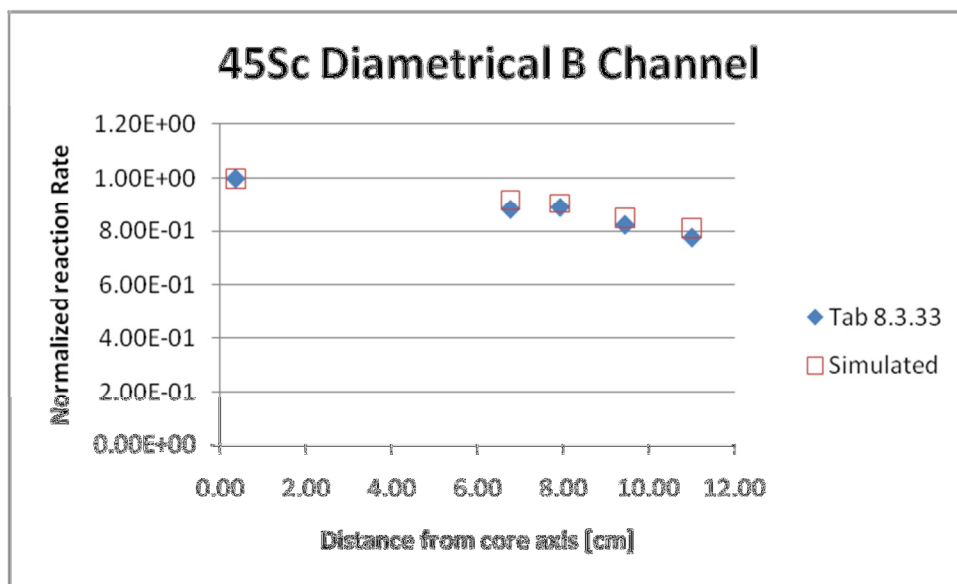


Figure 79 Comparison of experimental vs. simulated responses for  $^{45}\text{Sc}(n,\gamma)^{46}\text{Sc}$  reaction rate in Diametrical channel.

Table 39 Comparison of measured (Table 8.3.12) and simulated  $^{58}\text{Ni}(n,p)^{58}\text{Co}$  reaction rate in selected positions on the Diametrical (B) channel axis.

*Distance [cm]	Measured Rate		Estimated Rate	
	Reaction Rate Equivalent fission flux per main monitor count [n/cm <sup>2</sup> /s/cps]	Normalized	Reaction Rate [atom/cm <sup>3</sup> per s.p.]	Normalized
0.53	4.26E+07	1.00E+00	3.91E-05	1.00E+00
6.56	1.56E+07	3.66E-01	1.42E-05	3.63E-01
7.59	9.77E+06	2.29E-01	8.83E-06	2.26E-01
8.96	5.63E+06	1.32E-01	5.02E-06	1.28E-01
10.30	3.43E+06	8.05E-02	3.08E-06	7.87E-02
11.40	2.43E+06	5.70E-02	2.13E-06	5.45E-02
12.40	1.74E+06	4.08E-02	1.57E-06	4.02E-02
13.80	1.16E+06	2.72E-02	1.07E-06	2.73E-02
15.40	7.22E+05	1.69E-02	6.90E-07	1.77E-02
17.90	3.69E+05	8.66E-03	3.67E-07	9.39E-03
20.50	2.01E+05	4.72E-03	1.90E-07	4.85E-03
22.80	1.17E+05	2.75E-03	1.09E-07	2.80E-03

\* For radial and diametrical channel distance on channel axis taking origin in the intersection of core axis with channel axis . For tangential channel the origin is the intersection of the translation of the core axis (- 10.6 cm on y axis of MCNP reference system) with the channel axis.

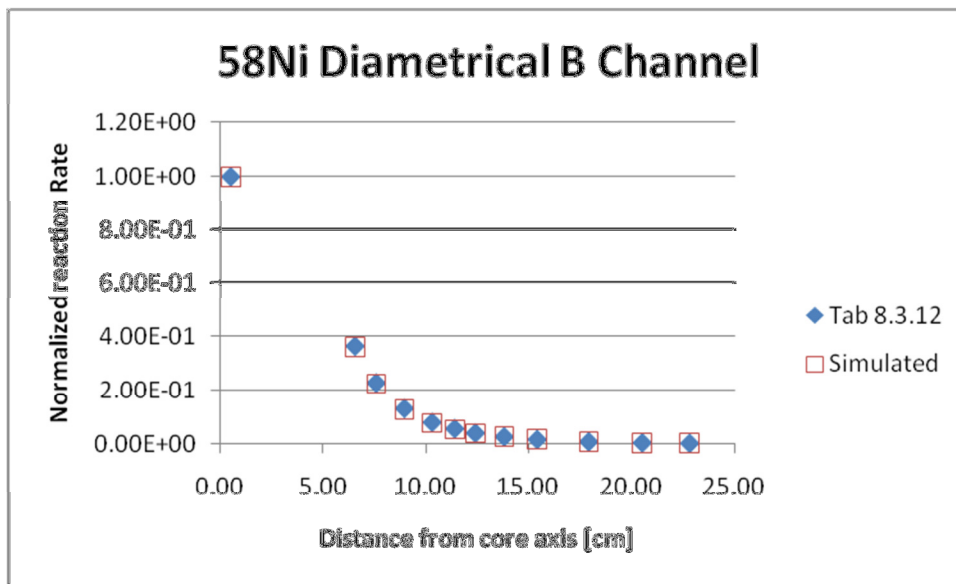


Figure 80 Comparison of experimental vs. simulated responses for  $^{58}\text{Ni}(n,p)^{58}\text{Co}$  reaction rate in Diametrical channel.

Table 40 Comparison of measured (Table 8.3.35) and simulated  $^{59}\text{Co}(n,\gamma)^{60}\text{Co}$  reaction rate in selected positions on the Diametrical (B) channel axis.

*Distance [cm]	Measured Rate		Estimated Rate	
	Absolute Reaction Rate per Unit Source* [Bq/atom/fission]	Normalized	Reaction Rate [atom/cm <sup>3</sup> per s.p.]	Normalized
0.51	5.70E-29	5.14E-01	4.96E-06	4.59E-01
6.53	7.32E-29	6.59E-01	6.46E-06	5.99E-01
7.54	9.09E-29	8.19E-01	8.62E-06	7.99E-01
8.90	1.01E-28	9.10E-01	1.06E-05	9.84E-01
10.26	1.11E-28	1.00E+00	1.08E-05	1.00E+00

\* For radial and diametrical channel distance on channel axis taking origin in the intersection of core axis with channel axis . For tangential channel the origin is the intersection of the translation of the core axis (- 10.6 cm on y axis of MCNP reference system) with the channel axis.

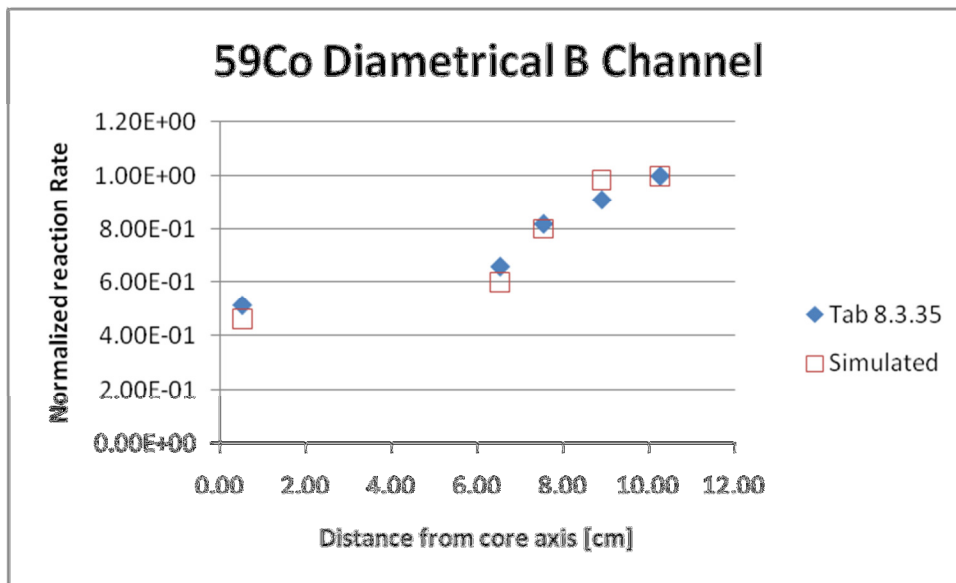


Figure 81 Comparison of experimental vs. simulated responses for  $^{59}\text{Co}(n,\gamma)^{60}\text{Co}$  reaction rate in Diametrical channel.



Table 41 Comparison of measured (Table 8.3.34) and simulated  $^{197}\text{Au}(n,\gamma)^{198}\text{Au}$  reaction rate in selected positions on the Diametrical (B) channel axis.

*Distance [cm]	Measured Rate		Estimated Rate	
	Absolute Reaction Rate per Main Monitor Count [Bq/atom/cps]	Normalized	Reaction Rate [atom/cm <sup>3</sup> per s.p.]	Normalized
0.51	2.17E-13	6.96E-01	5.60E-05	8.62E-01
7.58	2.49E-13	7.98E-01	6.50E-05	1.00E+00
10.29	2.91E-13	9.33E-01	6.25E-05	9.62E-01
12.32	2.98E-13	9.55E-01	5.76E-05	8.87E-01
15.31	3.10E-13	9.94E-01	5.97E-05	9.19E-01
20.33	3.12E-13	1.00E+00	5.52E-05	8.49E-01

\* For radial and diametrical channel distance on channel axis taking origin in the intersection of core axis with channel axis . For tangential channel the origin is the intersection of the translation of the core axis (- 10.6 cm on y axis of MCNP reference system) with the channel axis.

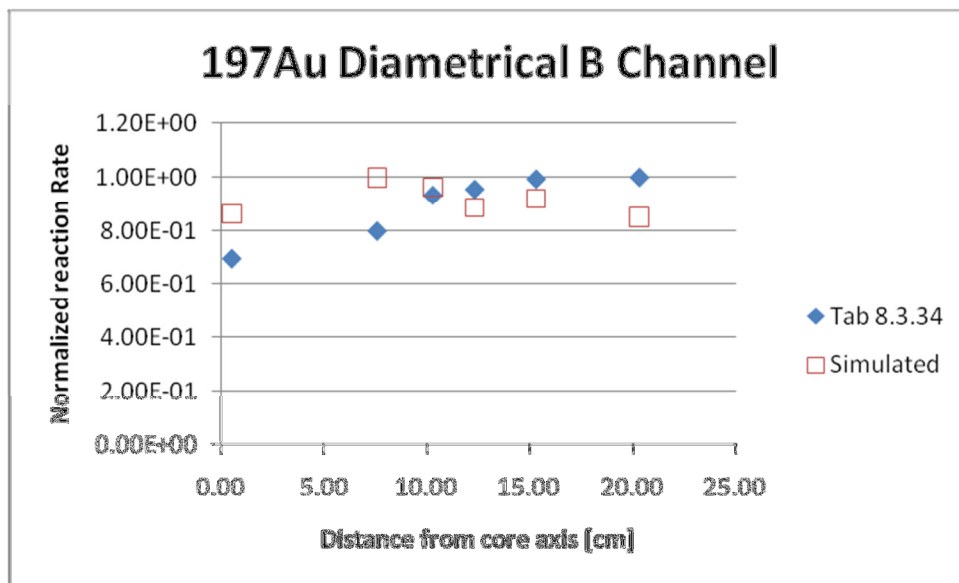


Figure 82 Comparison of experimental vs. simulated responses for  $^{197}\text{Au}(n,\gamma)^{198}\text{Au}$  reaction rate in Diametrical channel.

*Tangential Channel (B)*

Branch B of the Tangential channel is the one located to the regulation rod side of the core (see Figure 4). Measured and simulated  $^{45}\text{Sc}(n,\gamma)^{46}\text{Sc}$  reaction rate show a good agreement (see Figure 83 and Table 42). The same trend has been found for  $^{58}\text{Ni}(n,p)^{58}\text{Co}$  reaction rate (see Table 43 and Figure 84) again, simulated data tends to overestimate experimental data. Simulated  $^{59}\text{Co}(n,\gamma)^{60}\text{Co}$  data are in poor agreement with experimental data (see Table 44 and Figure 85). Simulated  $^{197}\text{Au}(n,\gamma)^{198}\text{Au}$  reaction rates (see Table 45 and Figure 86) are totally in disagreement with experimental findings.

**Table 42 Comparison of measured (Table 8.3.33) and simulated  $^{45}\text{Sc}(n,\gamma)^{46}\text{Sc}$  reaction rate in selected positions on the tangential (B) channel axis.**

*Distance [cm]	Measured Rate		Estimated Rate	
	Absolute Reaction Rate per Unit Source [Bq/atom/fission]	Normalized	Reaction Rate [atom/cm <sup>3</sup> per s.p.]	Normalized
5.18	5.52E-29	1.00E+00	2.11E-06	1.00E+00
7.70	5.10E-29	9.24E-01	1.98E-06	9.41E-01
11.98	4.58E-29	8.30E-01	1.79E-06	8.52E-01
16.72	3.90E-29	7.07E-01	1.47E-06	7.00E-01
21.53	3.08E-29	5.58E-01	1.13E-06	5.37E-01
26.46	2.40E-29	4.35E-01	8.60E-07	4.09E-01

\* For radial and diametrical channel distance on channel axis taking origin in the intersection of core axis with channel axis . For tangential channel the origin is the intersection of the translation of the core axis (- 10.6 cm on y axis of MCNP reference system) with the channel axis.

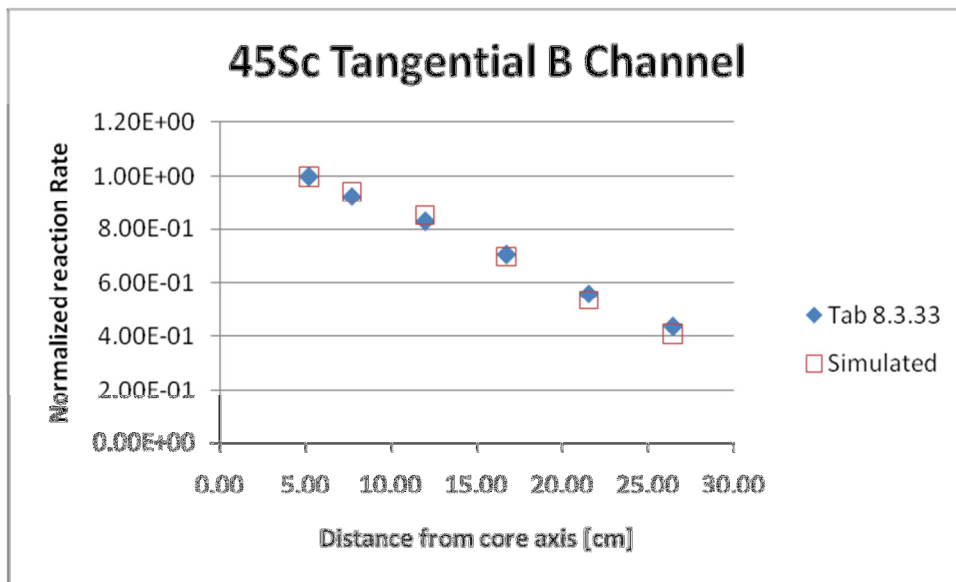


**Figure 83 Comparison of experimental vs. simulated responses for  $^{45}\text{Sc}(n,\gamma)^{46}\text{Sc}$  reaction rate in Tangential channel.**

Table 43 Comparison of measured (Table 8.3.14) and simulated  $^{58}\text{Ni}(n,p)^{58}\text{Co}$  reaction rate in selected positions on the tangential (B) channel axis.

*Distance [cm]	Measured Rate		Estimated Rate	
	Reaction Rate Equivalent fission flux per main monitor count [n/cm <sup>2</sup> /s/cps]	Normalized	Reaction Rate [atom/cm <sup>3</sup> per s.p.]	Normalized
5.18	4.72E+10	1.00E+00	1.49E-06	1.00E+00
8.03	2.54E+10	5.38E-01	9.77E-07	6.57E-01
12.38	1.05E+10	2.22E-01	4.74E-07	3.19E-01
17.08	3.81E+09	8.07E-02	1.85E-07	1.24E-01
21.98	1.49E+09	3.16E-02	6.41E-08	4.31E-02
26.78	4.93E+08	1.04E-02	2.38E-08	1.60E-02

\* For radial and diametrical channel distance on channel axis taking origin in the intersection of core axis with channel axis . For tangential channel the origin is the intersection of the translation of the core axis (- 10.6 cm on y axis of MCNP reference system) with the channel axis.

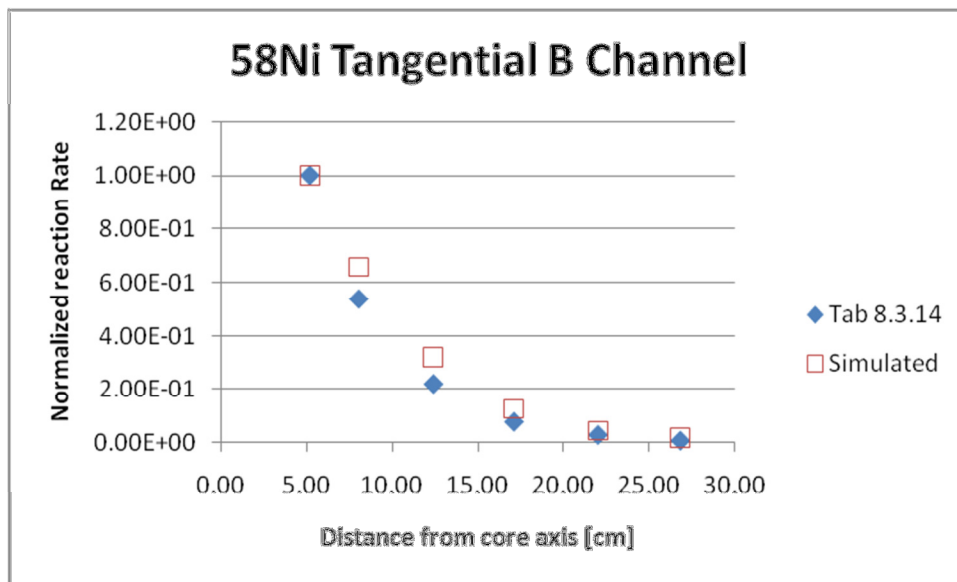


Figure 84 Comparison of experimental vs. simulated responses for  $^{58}\text{Ni}(n,p)^{58}\text{Co}$  reaction rate in Tangential channel.

Table 44 Comparison of measured (Table 8.3.35) and simulated  $^{59}\text{Co}(n,\gamma)^{60}\text{Co}$  reaction rate in selected positions on the tangential (B) channel axis.

*Distance [cm]	Measured Rate		Estimated Rate	
	Absolute Reaction Rate per Unit Source* [Bq/atom/fission]	Normalized	Reaction Rate [atom/cm <sup>3</sup> per s.p.]	Normalized
5.07	1.02E-28	9.71E-01	1.29E-05	8.98E-01
7.70	1.04E-28	9.90E-01	1.18E-05	8.22E-01
11.98	1.05E-28	1.00E+00	1.43E-05	1.00E+00
16.72	9.81E-29	9.34E-01	1.18E-05	8.26E-01
21.53	8.70E-29	8.29E-01	9.11E-06	6.36E-01
26.35	7.53E-29	7.17E-01	8.94E-06	6.24E-01

\* For radial and diametrical channel distance on channel axis taking origin in the intersection of core axis with channel axis . For tangential channel the origin is the intersection of the translation of the core axis (- 10.6 cm on y axis of MCNP reference system) with the channel axis.

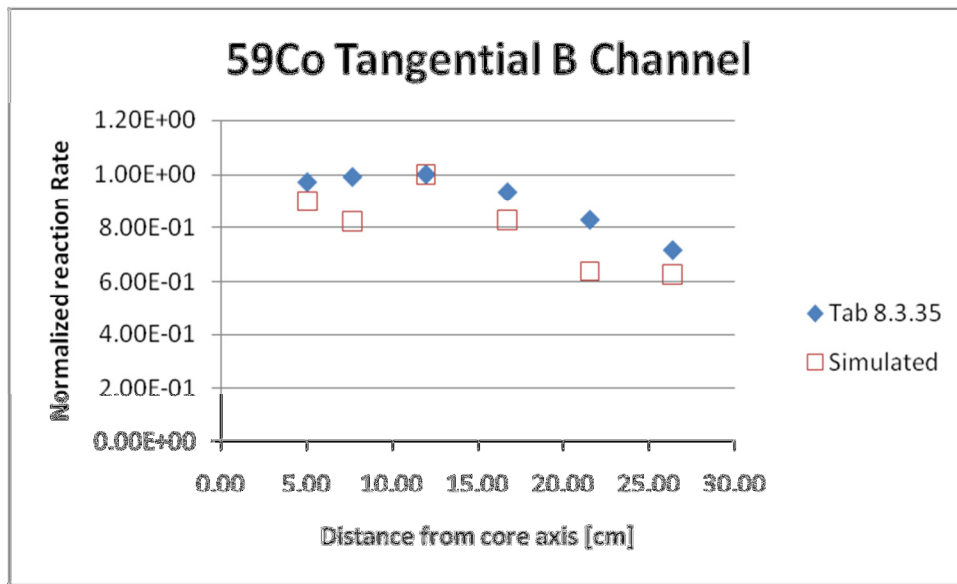


Figure 85 Comparison of experimental vs. simulated responses for  $^{59}\text{Co}(n,\gamma)^{60}\text{Co}$  reaction rate in Tangential channel.

Table 45 Comparison of measured (Table 8.3.34) and simulated  $^{197}\text{Au}(n,\gamma)^{198}\text{Au}$  reaction rate in selected positions on the tangential (B) channel axis.

*Distance [cm]	Measured Rate		Estimated Rate	
	Absolute Reaction Rate per Main Monitor Count [Bq/atom/cps]	Normalized	Reaction Rate [atom/cm <sup>3</sup> per s.p.]	Normalized
5.18	2.89E-13	9.57E-01	8.23E-05	1.00E+00
8.03	2.94E-13	9.74E-01	6.39E-05	7.77E-01
12.38	3.02E-13	1.00E+00	6.67E-05	8.11E-01
17.08	2.86E-13	9.47E-01	5.28E-05	6.42E-01
21.98	2.64E-13	8.74E-01	4.55E-05	5.54E-01
26.89	2.50E-13	8.28E-01	5.55E-05	6.74E-01

\* For radial and diametrical channel distance on channel axis taking origin in the intersection of core axis with channel axis . For tangential channel the origin is the intersection of the translation of the core axis (- 10.6 cm on y axis of MCNP reference system) with the channel axis.

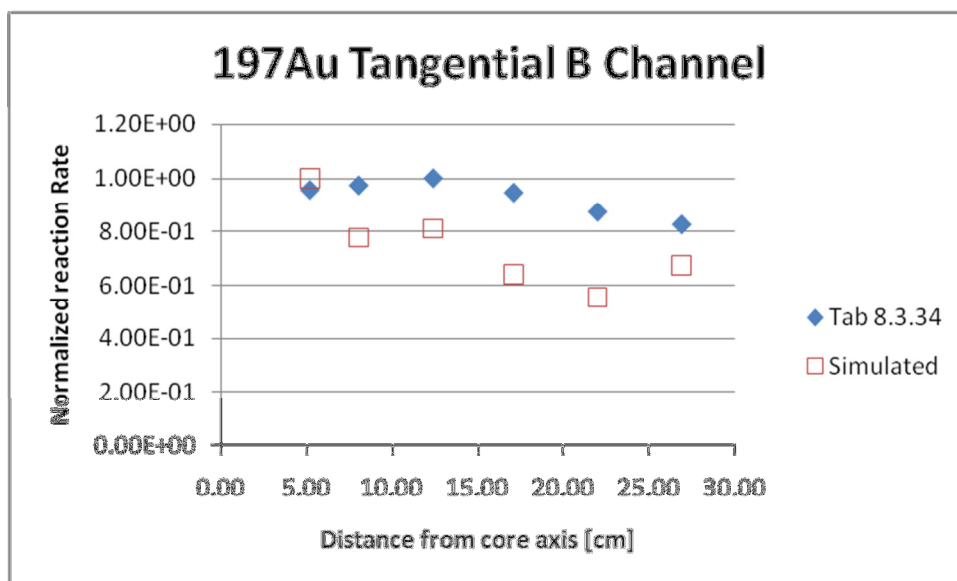


Figure 86 Comparison of experimental vs. simulated responses for  $^{197}\text{Au}(n,\gamma)^{198}\text{Au}$  reaction rate in tangential channel.

*Radial 1 channel*

Simulated  $^{58}\text{Ni}(n,p)^{58}\text{Co}$  reaction rate is in good agreement with experimental findings. The simulated reaction rates tend to overestimate the experimental findings.

**Table 46 Comparison of measured (Table 8.3.13) and simulated  $^{58}\text{Ni}(n,p)^{58}\text{Co}$  reaction rate in selected positions on the radial 1 channel axis.**

*Distance [cm]	Measured Rate		Estimated Rate	
	Reaction Rate Equivalent fission flux per main monitor count [n/cm <sup>2</sup> /s/cps]	Normalized	Reaction Rate [atom/cm <sup>3</sup> per s.p.]	Normalized
11.80	4.72E+10	1.00E+00	2.80E-06	1.00E+00
13.30	2.54E+10	5.38E-01	1.93E-06	6.91E-01
16.30	1.05E+10	2.22E-01	9.73E-07	3.48E-01
20.10	3.81E+09	8.07E-02	4.36E-07	1.56E-01
24.40	1.49E+09	3.16E-02	1.97E-07	7.05E-02
28.80	4.93E+08	1.04E-02	9.55E-08	3.41E-02

\* For radial and diametrical channel distance on channel axis taking origin in the intersection of core axis with channel axis . For tangential channel the origin is the intersection of the translation of the core axis (- 10.6 cm on y axis of MCNP reference system) with the channel axis.

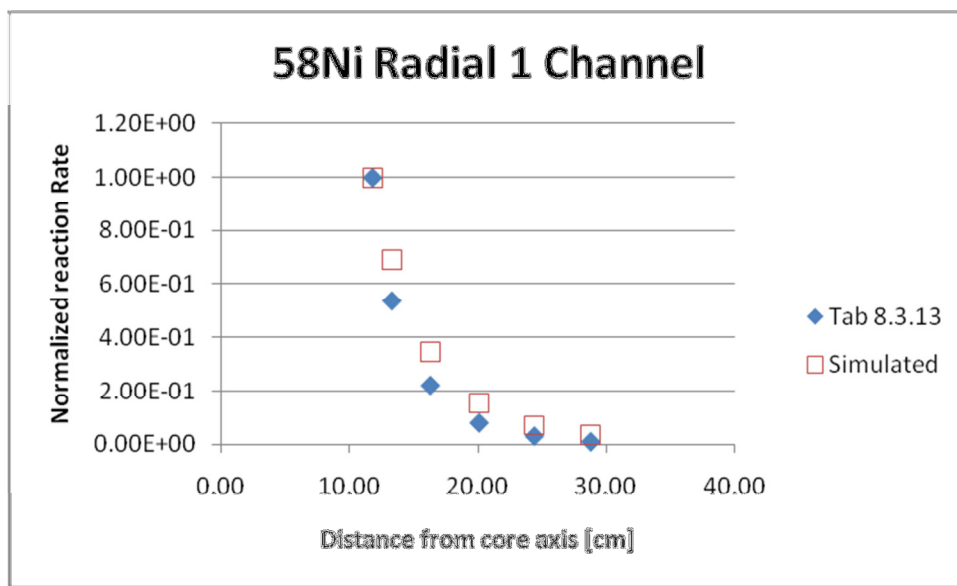


**Figure 87 Comparison of experimental vs. simulated responses for  $^{58}\text{Ni}(n,p)^{58}\text{Co}$  reaction rate in radial channel.**

## Conclusions

- TAPIRO MCNPX model succeed in the evaluation of control rods worth. Both ENDF and JEFF cross section data set estimated practically the same values of the rods worth that are in good agreement with experimental evaluation.
- Both ENDF and JEFF cross sections data set made the reactor model super critical when control rods are positioned in an experimentally critical configuration. When ENDF data set is used, the bias toward criticality is +500 PCM. In the case of JEFF data set, the bias is limited to 100 PCM. This last outcome is very close to experimental criticality and consequently, the remaining part of the simulation activity has been carried out with JEFF cross sections. The analysis of the different cross section data set behavior as not, presently, taken into account.
- As expected, the energy spectra of the neutron flux, estimate along traverses in tangential, radial 1 and diametrical channels, show a progressive departure from the fission spectrum as the slow down action of the copper reflector increases with the distance from the core center. Both flux intensity and spectra are in good agreement with experimental findings.
- Simulated fission rate traverses of  $^{235}\text{U}$ ,  $^{238}\text{U}$ ,  $^{239}\text{Pu}$  and  $^{237}\text{Np}$  have been estimated with two type of tallies (F5/Detectors and MESH) yielding in coincident results. The congruence of the tally results with the previously estimated spectral properties of the correspondent neutron flux has been positively tested ensuring the TAPIRO model internal coherence.
- Neutron induced reaction rates on  $^{45}\text{Sc}$ ,  $^{197}\text{Au}$ ,  $^{58}\text{Ni}$  and  $^{59}\text{Co}$  foils have been estimated along the same traverses in diametrical, radial1 and tangential channels with both F5/Detectors and MESH tallies. Due to the fast/epithermic nature of the TAPIRO neutron flux, the reaction rate traverses of  $^{59}\text{Co}$  and  $^{197}\text{Au}$  were affected by large uncertainties. However, reaction rate estimations of the two type of tallies yielding again, in the limit of the statistical confidence, equivalent results.
- The overall agreement of simulated and measured data is good except for  $^{197}\text{Au}$  results. One possible explanation for the unsuccessful estimation of this reaction could be the peculiar nature of the TAPIRO neutron spectrum that shows were poor intensity in the zone of maximum value of the Au cross section causing high uncertainties in the tally inference mechanism. However, the model set-up is sufficiently accurate to allow the detailed design of experiences in the irradiation facility of the TAPIRO reactor.

## Reference

- [1] A. Gandini, "Uncertainty Analysis and Experimental Data Transposition Methods Based on Perturbation Theory" in Handbook of Uncertainty Analysis, Y. Ronen Ed., CRC Press, Boca Raton, Florida, 1988.
- [2] A. Fabry Editor "Neutronic characterization of the TAPIRO fast-neutrons source reactor –Final Report-" Volumes 1-4.
- [3] "Rapporto di sicurezza per il R.S.V. TAPIRO vol. 1°: Descrizione", CNEN – Class. 0-3 – Arch. 57 - 26/09/1969.
- [4] X-5 Monte Carlo Team "MCNP: A General Monte Carlo Transport Code" LA-CP-03-245 April 24,2003 (Revised 10/3/05).
- [5] "Reattore TAPIRO: collaudo tecnico-amministrativo del nocciolo", documento CNEN, 1/11/1969.
- [6] "Prove Nucleari eseguite con il Reattore TAPIRO", CNEN - Laboratorio Fisica e Calcolo Reattori -1971.
- [7] A. Nouri, P. Nagel, N. Soppera, A. Ahite, B. Taton, J. Patrouix, F. Lecompanion, C. Cunin, O. Rioland, L. D'Eurveilher "JANIS: A New Software for Nuclear Data Services" , ND2001 Nuclear data conference.
- [8] J.W. Eaton, D. Bateman S. Hauberg "GNU Octave Manual Version 3" Network Theory Ltd. ISBN 0-9546120-6-X.